DnaB and DciA: Mechanisms of Helicase Loading and Translocation on ssDNA

*°[1,2]Nicholas Gao, *[4]Daniele Mazzoletti, [1]Adele Peng, [5]Paul Dominic B. Olinares, §[4]Castrese Morrone, ^[4]Andrea Garavaglia, [1]Nourelhoda Gouda, [1]Sergey Tsoy, [1]Albert Mendoza, [1]Ahammad Chowdhury, [1,4]Antonio Cerullo, [1]Hrutvik Bhavsar, [4]Franca Rossi, [4]Menico Rizzi, [5]Brian T, Chait, #[4]Riccardo Miggiano, and #[1,2,3,4]David Jeruzalmi

[1]Department of Chemistry and Biochemistry, City College of New York, New York, NY 10031, USA.

Ph.D. Programs in Biochemistry[2], Biology[3], and Chemistry[4], The Graduate Center of the City University of New York, New York, NY 10016, USA.

[4]Department of Pharmaceutical Sciences, University of Piemonte Orientale, Novara, 28100, Italy

[5]Laboratory for Mass Spectrometry and Gaseous Ion Chemistry, The Rockefeller University, New York, New York 10065, USA

#For correspondence: dj@ccny.cuny.edu or riccardo.miggiano@uniupo.it

*These authors contributed equally.

°Present address: Mirimus Inc, 760 Parkside Ave, Brooklyn, NY 11226, USA

§Present address: Telethon Institute of Genetics and Medicine (TIGEM) Via Campi Flegrei, 34 80078 Pozzuoli (NA) Italy.

^Present address: Department of Pharmaceutical Science (DISFARM), University of Milan, Milan, 20133 Italy

Graphical Abstract

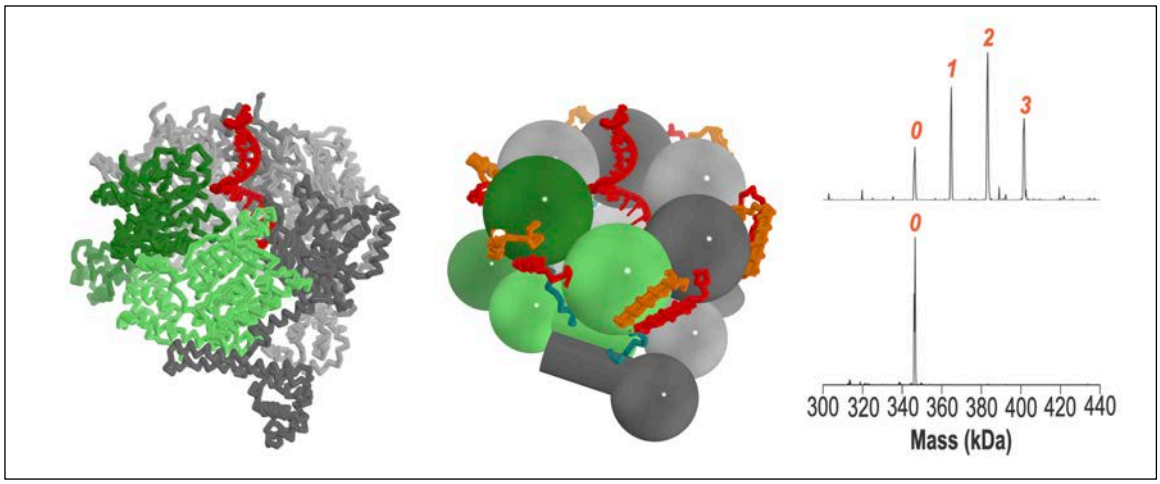

The *Vibrio cholerae* (*Vc*) DnaB replicative helicase structure bound to single-stranded (ss) DNA is depicted in the ribbon (top left) and sphere-cylinder representation (top right). In the bottom center is a native mass spectrum showing Vc DnaB helicase loading onto single-stranded DNA (ssDNA).

Abstract

Replicative helicases are assembled on chromosomes by helicase loaders before initiation of DNA replication. Here, we investigate mechanisms used by the bacterial *Vibrio cholerae* (*Vc*) DnaB replicative helicase and the DciA helicase loader. Structural analysis of the ATPγS form of the *Vc*DnaB-ssDNA complex reveals a configuration distinct from that seen with GDP•AlF_4. With ATPγS, the amino-terminal (NTD) tier, previously found as an open spiral in the GDP•AlF_4 complex, adopts a closed planar arrangement. Further, the DnaB subunit at the top of the carboxy-terminal spiral (CTD) tier is displaced by ~25 Å between the two forms. We suggest that remodeling the NTD layer between closed planar and open spiral configurations and migration of two distinct CTDs to the top of the DnaB spiral, repeated three times, mediates hand-over-hand translocation. Biochemical analysis suggests that *Vc*DciA leverages its Lasso domain to contact DnaB near its Docking-Linker-Helix interface. Up to three copies of *Vc*DciA bind to *Vc*DnaB and suppress its ATPase activity during loading onto physiological DNA substrates. Our data suggest that DciA loads DnaB onto DNA using the ring-opening mechanism.

Introduction

Replisomes in all domains of life rely on replicative helicases to melt chromosomal DNA into single-stranded templates for DNA replication (Figure 1)(1–6). In *E. coli*, the hexameric DnaB replicative helicase is a closed protein ring that encircles and translocates on one strand of DNA, excluding the second, as it prepares templates for DNA synthesis (Figure 1). Members of the DnaB family (7–20) (henceforth: DnaB) and (reviewed in (21–27)) feature a two-tiered architecture, termed the amino-terminal domain (NTD) and the carboxy-terminal domain (CTD); each tier circumscribes a central channel through which ssDNA will traverse. A short linker helix (LH) connects each NTD and CTD; the LH packs against a neighboring CTD's docking helix (DH) in the complete hexamer. The translocating form of DnaB adopts a right-handed closed-spiral configuration and is suggested to operate using a hand-over-hand mechanism. Translocation occurs akin to a human using two hands to climb a rope, except that DnaB has six hands (10). ATP hydrolysis on a DnaB subunit at the bottom of the spiral (in the pose in Figure 2) initiates translocation. This subunit peels away from its DnaB partners and from ssDNA (10, 24, 28, 29), migrates to the top of the spiral, binds ATP, docks onto a DnaB subunit via its β-hairpin arginine finger, and binds ssDNA position 3' from the original location. Translocation continues via additional subunit migrations from the bottom to the top of the DnaB spiral (10). Crucial support for this model emerged from a series of structures of the DnaB-family helicase Gp4 from phage T7 (24, 29).

Assembly of DnaB on single-stranded DNA (ssDNA) requires distinct mechanisms and loading factors (Supplementary Figure 1). The loading factors include

80 *Escherichia coli* (*Ec coli)* DnaC (30), bacteriophage λP (31), bacteriophage SPP1
81 G39P (32, 33), *Bacillus subtilis* (*Bst*) DnaI (34), T4 gene 59 (35), and phage P2 B
82 (36). Surprisingly, the genomes of most bacteria lack these well-studied loaders.
83 Instead, most bacteria employ the structurally and perhaps mechanistically distinct
84 DciA or DopE family members (37–41). Although the amino acid sequences of
85 bacterial helicase loaders diverge significantly, they appear to mediate conserved
86 mechanisms during helicase loading (11, 12, 14, 16, 19, 36, 42–48). Loaders
87 display a conserved overall architecture: a globular domain adjacent to an
88 intrinsically disordered segment that often features an alpha helix at a terminus,
89 termed the lasso/grappling hook. Related arrangements can also be inferred for
90 *Bst* SPP1 phage G39P (49), *Bst* DnaI (16, 50–52), and *Ec* phage T4 gp59 (53)
91 helicase loaders. The DciA helicase loaders are organized around a type II K
92 homology domain (KH) with Lasso elements at either the amino or carboxy
93 terminus of a particular ortholog or both (12, 14, 40, 41, 54).

94 Cells apply three broad strategies to load hexameric helicases onto nucleic acid
95 substrates: ring-opening, ring-forming, and ring-closing (22, 55, 56)
96 (Supplementary Figure 1 and Supplementary Information). Although much is
97 known about many bacterial loaders (11, 12, 14, 16, 19, 36, 42–46), little is known
98 about DciA helicase loaders and the mechanisms they implement during helicase
99 loading. DciA orthologs from *Vibrio cholerae* (*Vc*), *Mycobacterium tuberculosis*
100 (*Mt*), and *Caulobacter crescentus* (*Cc*) are all essential proteins (37, 42, 57, 58),
101 and they have been shown to bind to cognate DnaB helicases (12, 14, 42, 57, 58).
102 Component KH and Lasso domains contact DnaB (12, 14, 58). The binding site

103 on DnaB for DciA is proposed to encompass the DH-LH interface (12, 14, 58).
104 DciA orthologs bind to DNA (11, 58, 59), a feature shared with other bacterial
105 loaders (31, 35, 47, 60). Suppression of DnaB's ATPase activity is a hallmark of
106 the bacterial helicase loaders(43, 46, 60); however, *Cc*DciA has been reported to
107 promote ATP hydrolysis (42). DciA activates cognate DnaB's DNA unwinding
108 activity by mediating assembly on ssDNA, though the underlying mechanisms
109 have yet to be established (40, 41).

110 To gain insights into the mechanisms operating during the loading of DnaB by the
111 DciA loader and subsequent translocation, we studied the orthologs from *Vibrio*
112 *cholerae*. The single particle cryogenic electron microscopy (cryo-EM) structure
113 of the *Vc*DnaB-ssDNA-ATPγS (ATPγS: Adenosine 5'-O-(3-thio)triphosphate)
114 complex, the end state of helicase loading, implies that cycles of opening/closing
115 of the NTD layer and CTD remodeling are significant features in the mechanism of
116 translocation on ssDNA. We suggest that remodeling of the NTD layer and distinct
117 migrations of two subunits to the top of the DnaB spiral, repeated three times,
118 mediates hand-over-hand translocation. Native mass spectrometry (nMS)
119 indicates that *Vc*DnaB is a hexamer, and that the stoichiometry of the *Vc*DnaB-
120 DciA-ssDNA complex is 6:3:1. *Vc*DciA features a KH domain at its amino terminus
121 and a disordered segment (lasso) at its carboxy terminus (12, 40, 41, 54, 58).
122 Binding experiments show that the lasso segment specifies most of the binding
123 energy in its interaction with DnaB. Furthermore, *Vc*DciA binds to DnaB at the
124 interface between the docking helix (DH) and linker helix (LH) on adjacent
125 subunits. *Vc*DciA suppresses the intrinsic ATPase activity of DnaB. We show that

126 *Vc*DciA loads DnaB onto ssDNA and activates unwinding. Overall, our data
127 suggest that *Vc*DciA is a ring-opening helicase loader.

128 # Materials and methods
129 ## Protein Biochemistry
130 Standard techniques (61) were used to develop the nine proteins used in
131 this study. Our studies encompassed efforts with full-length and designed
132 truncations of DnaB and DciA from *Vibrio cholerae* (Supplementary Figure 2). The
133 DnaB constructs included the full-length sequence (1-468), the DnaB amino-
134 terminal domain (NTD; 1-170), the DnaB amino-terminal domain fused to the
135 Linker Helix (NTD-LH; 1-208), and the Linker helix fused to the DnaB carboxy-
136 terminal domain (CTD; 208-468). The DciA constructs included the complete
137 sequence (1-157), the KH domain (1-98), and the Lasso domains (98-157). The
138 supplementary methods section (Supplementary Methods and Tables 1 and 2)
139 provides complete details on plasmid construction, bacterial expression, and
140 protein purification.

141 Interactions between DnaB and DciA and their respective truncations were
142 interrogated by co-lysing bacteria that separately expressed each protein, where
143 only one of the proteins was histidine-tagged. The lysate was passed over NiNTA
144 agarose (QIAGEN), washed of contaminants, and histidine-tagged proteins were
145 eluted. Interactions were scored based on the propensity of the untagged protein
146 in the experiment to be retained on Ni-NTA agarose (QIAGEN) compared to trials
147 where the histidine-tagged protein was omitted. The supplementary methods
148 section describes the 'pull-down' experiments more completely.

149 ## Surface Plasmon Resonance

150 Dissociation constants (K_D) were estimated using surface plasmon
151 resonance (SPR) from measurements of the on and off rates between DnaB and
152 DciA. SPR data were acquired using a Biacore X100 instrument (GE
153 Healthcare/Cytiva), and a CM5 sensor chip functionalized with an anti-histidine
154 antibody according to the manufacturer's instructions. All measurements were
155 conducted at 25 °C. Since the SPR response is proportional to molecular weight,
156 we chose to immobilize the smaller C-terminal-His-tagged-DciA (MW = 18.4 kDa)
157 while positioning the much larger DnaB (MW = 312.3 kDa) in the mobile phase.
158 DciA was immobilized on the surface of a single channel of the CM5 sensor chip
159 via the interaction between the histidine tag and the anti-histidine antibody. The
160 appropriate ligand density (RL) on the chip was calculated according to the
161 equation: $RL = \left(\frac{ligand\ MW}{analyte\ MW}\right) \times R_{max} \times \left(\frac{1}{S_m}\right)$ where R_{max} is the maximum binding
162 signal, and S_m corresponds to the binding stoichiometry. With the immobilization
163 procedure complete, non-specifically bound proteins were removed by washing
164 with buffer HBS-EP+ (Cytiva) until the resonance signal reached a constant
165 baseline. The reference flow cell provided a control surface for refractive index
166 change and non-specific binding. DnaB solution was injected five times at
167 increasing concentrations over the DciA-functionalized sensor surface in a single-
168 cycle kinetics experiment. A long dissociation phase and a single regeneration
169 step followed the last sample injection, without regeneration between each
170 sample-injection.

171 The interaction between DnaB and DciA was assumed to display 1:1
172 kinetics; as such, the measured SPR data should display pseudo-first-order
173 kinetics that is described by the following rate equation:

174 (1) $$\frac{d[LA]}{d[t]} = k_a \cdot [L] \cdot [A] - k_d[LA]$$

175 where k_a is the association rate constant, which refers to the rate of complex
176 formation (units: $M^{-1}s^{-1}$); the dissociation rate constant k_d describes the stability of
177 the complex, i.e., the fraction of complexes that dissociate in the time frame (units:
178 M). [A] represents the analyte concentration; [LA] is the complex concentration
179 measured directly as R in Resonance Units (RU); [L] is the ligand concentration
180 on the surface.

181 To enable fitting of the SPR data, equation (1) was modified as follows:

182 (2) $$\frac{d[R]}{d[t]} = k_a \cdot [C] \cdot [Rmax - R] - k_d[R]$$

183 where Rmax is the maximum binding capacity, and Rmax-R is the free
184 concentration of the analyte. Rmax and R were extracted from the experimental
185 SPR curves. The fitted data proved estimates for k_d and k_a from which $K_D = k_d/k_a$
186 was calculated. Experimental binding kinetic data were fit to the '1:1 binding'
187 model implemented in the Biacore X100 Control Software (Cytiva).

188 **Native Mass Spectrometry**

189 *Vc*DnaB and *Vc*DciA samples for native mass spectrometry (nMS) were
190 exchanged into 500 mM ammonium acetate, pH 7.5, and 0.01% Tween-20 (nMS
191 buffer) using a Zeba micro spin desalting column with a molecular cutoff of 40 kDa
192 (ThermoFisher Scientific). Complexes containing DnaB and DciA in the above
193 buffer were mixed in defined molar ratios before nMS measurements. To take
194 data in the presence of nucleotide, ATP and magnesium acetate were added to
195 final concentrations of 10 μM and 0.5 mM, respectively.

196 The list of DNA molecules used in the nMS study appears in Supplementary
197 Table 2. Lyophilized synthesized ssDNAs (IDT) oligonucleotides were brought to

198 200 μM in HPLC-grade water and diluted to a working concentration of 3 - 6 μM in
199 the above nMS buffer.

200 An aliquot (3 – 5 μL) of an experimental sample was loaded into a gold-
201 coated quartz capillary tip prepared in-house. The sample was then
202 electrosprayed into an Exactive Plus EMR instrument (ThermoFisher Scientific)
203 using a modified static nanospray source (62, 63). Spectra were continuously
204 recorded from a single sample-loaded capillary. For analysis of DnaB and DnaB-
205 containing assemblies, the general MS parameters used include spray voltage, 1.2
206 – 1.3 kV; capillary temperature, 125 – 150 °C; S-lens RF level, 200; resolving
207 power, 8,750 or 17,500 at *m/z* of 200; AGC target, 1 x 10^6; number of micro scans,
208 5; maximum injection time, 200 ms; in-source dissociation (ISD), 0 – 10 V; injection
209 flatapole, 8 V; interflatapole, 4 V; bent flatapole, 4 V; high energy collision
210 dissociation (HCD), 200 V; ultrahigh vacuum pressure, 5 – 7 × 10^{-10} mbar; total
211 number of scans, 100. For analysis of full-length *Vc*DciA, the MS parameters are
212 similar as above except for capillary temperature, 100 °C in-source dissociation
213 (ISD), 100 V; injection flatapole, 8 V; interflatapole, 7 V; bent flatapole, 6 V; higher-
214 energy collisional dissociation (HCD), 0 V; ultrahigh vacuum pressure, 1.4 × 10^{-10}
215 mbar. Mass calibration in positive EMR mode was performed using a cesium
216 iodide solution. Raw nMS spectra were visualized using Thermo Xcalibur Qual
217 Browser (version 4.2.47). Data processing and spectra deconvolution was
218 performed using UniDec version 4.2.0 (64, 65) with the following general
219 parameters: background subtraction (if applied), subtract curve, 10; smooth
220 charge distribution, enabled; peak shape function, Gaussian; degree of Softmax

221 distribution (beta parameter): 2 – 20. PDBO measured all mass spectrometric data
222 in the laboratory of BTC.

223 **FRET-based DNA Strand Displacement Assay**

224 DNA unwinding by *Vc*DnaB and its stimulation by *Vc*DciA were measured
225 using a fluorescence resonance energy transfer (FRET) helicase strand
226 displacement assay adapted from reference (20). The DNA substrates for the
227 assay, FRET-DNA-fork-top-strand, FRET-DNA-fork-bottom-strand, and FRET-
228 DNA-fork-capture-oligo, are identical to those described in reference (20). The top
229 strand is labeled with Cy3 at its 5' end; the bottom strand is labeled with the BHQ_2
230 quencher at its 3' end. The capture oligo is unlabeled (Supplementary Table 2).

231 Strand displacement was measured by mixing annealed and fluorescence-
232 quenched substrates at a concentration of 100 nM with 200 nM DnaB and DciA
233 concentrations ranging from 0 nM to 6400 nM. An excess of the capture oligo (400
234 nM) was included to prevent the reannealing of the fork after strand displacement.
235 FRET data were taken at 37 °C in the following buffer: 20 mM K-HEPES pH = 7.5,
236 5 mM Mg acetate, 50 mM K-glutamate, 5% glycerol, and 4 mM dithiothreitol (DTT).
237 Reaction components were mixed into wells (volume: 100 μL/well) of a Corning
238 black plate (p/n: 3880) with 96 half-area clear flat bottom wells. The working
239 concentration of NaCl in the assay is 50 mM. The reaction was initiated by adding
240 1 mM ATP to each well; the plate was subsequently inserted in a SpectraMax M5
241 plate reader (Molecular Devices). FRET signals were recorded for 30 min at 37
242 °C. To avoid the crosstalk between Cy3's closely spaced excitation and emission
243 signals, an excitation wavelength of 520 nm was used; at this wavelength,
244 excitation is reduced to 50% of its maximal value

245 (https://www.thermofisher.com/us/en/home/life-science/cell-
246 analysis/fluorophores/cy3-dye.html); however, this wavelength does not overlap
247 with the fluorescence emission peak, measured at 570 nm. Relative Fluorescence
248 Unit (RFU) data taken in this way were exported for analysis in Microsoft Excel and
249 GraphPad Prism.

250 **FRET-based Replicative Helicase Loading Assay**

251 To measure helicase loading by DciA, we adapted the unwinding assay
252 described above; instead of a fork substrate with 5' and 3' unpaired segments, we
253 employed substrates that featured single-stranded 'bubbles' (Supplementary
254 Table 2) whose sequences are taken from (#894 and #895, reference: (42)).
255 Bubble substrates favor DnaB assembly on ssDNA instead of threading the free
256 end of ssDNA into the DnaB central chamber. In our first bubble substrate, the top
257 strand was singly labeled at the 5' end with Cy3, and the bottom strand with the
258 Iowa Black RQ quencher (IDT). To account for the possibility that DnaB helicase
259 could, in principle, be loaded for translocation in either direction, we employed a
260 second substrate wherein fluorophore – quencher pairs were installed at both ends
261 of the 'bubble' (Supplementary Information); such a substrate could inform on the
262 loading and translocation on both strands and in both directions. As with the strand
263 displacement assay, unlabeled capture strands forestalled the reannealing of the
264 quencher-containing bubble strand.

265 FRET signals from helicase loading were recorded and analyzed as described for
266 the strand displacement assay.

267 **Single Particle Cryogenic Electron Microscopy**

268 Samples for cryo-EM were prepared and imaged, and the images were processed
269 using standard techniques and software (66–69). Supplementary Methods,
270 Supplementary Figures 3 and 4, and Supplementary Table 3 provide detailed
271 descriptions.

272 **Model Building and Structure Refinement**

273 The DeepEMhancer-sharpened map H (Supplementary Figure 3) was
274 selected to build a molecular model of the *Vc*DnaB-ssDNA complex. Map H was
275 submitted to ModelAngelo (70) to construct the initial protein and DNA model. The
276 quality of the resulting model was high, even as it contained numerous chain
277 breaks. Next, we superimposed the AlphaFold predicted structure of *Vc*DnaB,
278 which has been split into three component domains (N-terminal Domain (NTD,
279 residues 1:170), Linker Helix (LH, residues 171:211), and C-terminal Domain
280 (CTD, residues 212:468)), onto the ModelAngelo output to create a model of
281 hexameric *Vc*DnaB with excellent stereochemistry. The program COOT (71) was
282 used to connect domains belonging to each monomer and to remove the following
283 DnaB residues (chain A, B: 1-21 and 463:468, C-E-F: 1:21 and 464:468, D: 1:22
284 and 464:468) because of missing map density. Although *Vc*DciA was present in
285 a four-fold excess in our cryo-EM sample, we found no EM density that the *Vc*DnaB
286 model did not explain. As such, we conclude that *Vc*DciA is not present in our
287 reconstruction.

288 The EM density in map H revealed an 11-mer ssDNA within the internal chamber
289 of DnaB. This was sufficiently resolved to distinguish the DNA backbone from the
290 nucleobases; however, it was not so resolved to permit assigning the nucleotide
291 sequence to the map. In many places, purines could be distinguished from

292 pyrimidines; however, we could not unambiguously position the 60-mer ssDNA in
293 our cryo-EM sample. An 11-mer ssDNA molecule (TCCAGATACAC) was
294 constructed in COOT (71, 72) and placed in density using its 'real space refine'
295 function. In the lower resolution map E0 (6.24 Å, Supplementary Figure 3), we
296 observed density extending away from DnaB along the axis where the 11-mer had
297 been built. The density quality in this map did not permit the DNA backbone to be
298 distinguished from the nucleobases. However, model building suggested that an
299 additional 11 nucleobases could explain this density. Since this density provided
300 no unique nucleobase information, we built this segment as polyadenine. The
301 extra 11 DNA bases visible in Map E0 were refined in COOT against this map.
302 The complete 22-mer ssDNA was refined against the high-resolution map H.

303 The *Vc*DnaB-ssDNA-ATPγS model was refined with Phenix (73–80). We
304 used the 'real_space_refine' protocol, encompassing global minimization,
305 morphing, NQH flips, and atomic displacement parameters (ADP). The refinement
306 leveraged three rigid bodies (DnaB residues 1:171, 171:211, 212:468, 501 for each
307 chain; ssDNA 1:11), Ramachandran, and secondary structure restraints.
308 Refinement was carried out against the DeepEMhancer sharpened 3.37 Å density
309 map H. A second round of real-space refinement encompassing global
310 minimization, atomic displacement parameters, NQH flips, with Ramachandran
311 and secondary structure restraints completed the model (Supplementary Table 3).
312 The final model includes Chain A (DnaB residues 22:461), Chain B (DnaB residues
313 22:462), Chain D (DnaB residues 23:463), Chains C-E-F (DnaB residues 22:463),

314 six ATPγS•Mg^{2+} complexes, one per chain (chains A-B-C-D-E-F residue 501), and
315 ssDNA (chain G, residues 1-22).

316 **Model Analysis and Visualization**

317 Structural analysis and visualization of the *Vc*DnaB-ssDNA complex were
318 performed in the CCP4 software package (81), Coot (71, 72), the Uppsala software
319 suite (82–85), UCSF-CHIMERA (86), Phenix (73–80), PyMOL (87), Nucplot (88),
320 and as described previously (44). Distances and angles within and between
321 protein structures were calculated using the PyMol Python scripts titled
322 "pairwise_dist" (https://pymolwiki.org/index.php/Pairwise_distances) and
323 "angle_between_domains"
324 (https://pymolwiki.org/index.php/Angle_between_domains). Molecular graphics
325 and figures were generated using UCSF-CHIMERA (86) and PYMOL (87). The
326 software used in this study was sourced from the SBGrid Consortium (89, 90).

327 **Results**

328 **Cryo-EM Structure of *Vc*DnaB Bound to ssDNA and ATPγS**

329 To understand the loading of the DnaB helicase by DciA, we applied single-particle
330 cryogenic electron microscopy (cryo-EM) to the *Vc*DnaB helicase bound to ATPγS,
331 *Vc*DciA, and ssDNA derived from the *Vc*OriC-I replication origin. In assembling
332 the complex, we relied on results from our nMS study (below). Cryo-EM analysis
333 (Supplementary Methods, Supplementary Figures 3, 4, and Supplementary Table
334 3) produced a 3.37 Å structure of hexameric *Vc*DnaB bound to ATPγS and
335 complexed to a 22-nucleotide ssDNA molecule (Figure 2 and Supplementary
336 Figures 5, 6, 7, and 8). The resolution of the EM density corresponding to one of
337 the chains (chain A) was lower than that of the other chains. Notwithstanding the
338 fourfold excess in the cryo-EM sample, our maps displayed no density

339 corresponding to the DciA loader. Our *Vc*DnaB-ssDNA complex likely represents
340 the end-state structure after DciA-mediated loading or self-threading.
341 Compared to the *Bst*DnaB-ssDNA complex, determined with GDP•AlF_4 (PDB:
342 4ESV (10)), the ATPγS form of the *Vc*DnaB-ssDNA complex presents a distinct
343 configuration (Figure 3). Both share the trimer of dimers and pseudo-sixfold
344 architecture of the NTD and CTD tiers. With diameters of ~55 Å and ~25 Å, the
345 NTD and CTD layers in the *Vc* ATPγS form are dilated and constricted (8),
346 respectively (Figures 2, 3, and Supplementary Figures 8 A-B-C-D). However, the
347 six-chain NTD tier from the *Vc* ATPγS structure adopts a closed triangular planar
348 and symmetric arrangement, resembling the NTD tier from other structures (PDB:
349 2R5U (91), Root Mean Square Deviation (RMSD) = 2.6 Å over 558 Cα atoms;
350 PDB: 7T20 (92), RMSD = 1.5 Å over 825 Cα atoms). This configuration differs
351 from the open spiral in the GDP•AlF_4 form of the Bst-DnaB-ssDNA complex (10).
352 As with other DnaB structures, the *Vc* NTD assembles around weak (head-to-
353 head) and strong interfaces (tail-to-tail), defined based on the buried surface area
354 (7); the NTD tier in the *Bst* structure is breached on the weak head-to-head
355 interface. In both nucleotide forms, the constricted CTD tier is arranged as a
356 closed spiral; however, the spirals are distinct (Supplementary Figure 9). The six
357 DnaB subunits in the *Vc* and Bst structures are labeled A-F-E-D-C-B around the
358 spiral; the breach in the CTD spiral lies between chains A and B, which are at the
359 bottom and top of the spiral (as in the pose in Figures 2 and 3), respectively. Five
360 of the six subunits of each structure (PDB: 4ESV: residues 181:441 and chain C,
361 D, E, F, and A on *Vc*DnaB: residues 204:441 and chain B, C, D, E, and F) chains

362 could be superimposed with an RMSD of 1.7 Å (1016 Cα atoms). The most
363 significant difference in CTD configurations is the distinct position occupied by
364 *Vc*DnaB chain A, which maps to chain B in the GDP•AlF4 4ESV structure; we
365 address this change in greater detail below. We also note that in the *Vc* ATPγS
366 form, chain A is located further away from its neighbors (distances to chain B:
367 ~39.6 Å, to chain F: ~34.6 Å) than the average distance separating the remaining
368 four subunits to their neighbors (Chains C, D, E, and F: ~33.4 Å). By contrast, in
369 the GDP•AlF4 4ESV structure, Chain A is distant from one immediate neighbor
370 (distance between chains B and A: 42.6 Å), while other chains are 32.5 Å from
371 their neighbors. Lastly, in the *Vc* ATPγS complex, the six Linker Helices (LH)
372 occupy three positions relative to the NTD and CTD. The LH elements of chains
373 B, C, D, and E occupy one position (LH1), with chains F (LH3) and A (LH2)
374 diverging from this position by rotations/displacements of ~16.5°/~7.1Å and
375 ~29.6°/12.3 Å, respectively. In the GDP•AlF_4 4ESV complex, the LH elements
376 occupy two positions, one by chains B, C, D, E, and F (LH1) and a second position
377 (LH4) by chain A (Supplementary Figure 10).

378 ssDNA in the complex traces a spiral path that passes through the internal
379 chamber of *Vc*DnaB (Figure 2). 11 of the 22 ssDNA nucleotides are bound to
380 subunits of the *Vc*DnaB hexamer; the remaining 11 are outside the DnaB perimeter
381 (Supplementary Figures 7 and 11). In contrast to the GDP•AlF_4 4ESV structure,
382 where each subunit contacts ssDNA, only five DnaB subunits in the current *Vc*
383 structure make contacts (less than 4.0 Å); chain A does not contact ssDNA. An
384 inventory of protein-DNA contacts reveals the involvement of seven *Vc*DnaB

residues, though not every contact is made by each subunit (Supplementary Table 4).

Six ATPγS/Mg^{2+} complexes are found at composite catalytic centers formed between adjacent *Vc*DnaB subunits, wherein the Walker A/P-loop and Walker B motifs are provided by one subunit and the β-hairpin arginine finger by a second (Figure 2C and Supplementary Figures 6 and 8E). In four nucleotide sites (chain F-E, E-D, D-C, and C-B), the β-hairpin/arginine finger makes a close approach to nucleotide on a neighboring subunit, with distances between the P-loop lysine (K234) and the arginine (R439) finger residues of ~11.3 Å. The corresponding distance at the A-F subunit interface is slightly longer (~11.9 Å), and the arginine finger has shifted by ~3 Å relative to other subunits. The β-hairpin/arginine finger at the nucleotide site that lines the breach (B-A) exhibits a considerably longer (~24.5 Å) distance. In the *Bst* GDP•AlF_4 complex, 5/6 sites (Chains A-F, F-E, E-D, D-C, and C-B) feature an average P-loop lysine (K216) to arginine (R420) finger distance of ~11.4; the chain B-A site, which lines the breach, has a considerably longer distance at ~32.8 Å.

Taken together, the significant changes between the GDP•AlF_4 and ATPγS forms of DnaB, including distinct NTD configurations, the offset of a single DnaB CTD, and diversity in LH element conformations in sequential subunits around the ring, imply that our structure has captured a distinct intermediate in the translocation reaction.

Remodeling of the NTD and CTD Tiers Accompanying Translocation

To place the distinct ATPγS form of DnaB in the translocation reaction, we compared it to the *Bst* GDP•AlF_4 (10) entity (Figure 3) and a series of DNA

409 complexes (PDB: 6N7I, 6N7S, 6N7T, and 6N7V) of the DnaB-family helicase Gp4
410 from phage T7 (24, 29) (Comparisons to other *Vc*DnaB structures appear in the
411 Supplementary Information). Aligning the *Vc* ATPγS and *Bst* GDP•AlF_4 structures
412 by superimposing 5/6 CTDs (RMSD: 1.7 Å, a similar alignment could be obtained
413 by aligning on the ssDNA (RMSD: 0.64 Å) reveals that *Vc* chain A, excluded from
414 the alignment, is displaced by 25 Å and rotated by ~22° relative to the
415 corresponding subunit in 4ESV (Chain B). Similar displacements/rotations are
416 seen in the HelF subunits in the 6N7T and 6N7V DnaB-family Gp4 helicase
417 structures, shifting positions by ~24 Å and ~13° (24, 29). Further, the DnaB
418 alignment juxtaposes all the components of the NTD layer save for the chains at
419 the top (4ESV: chain A) and bottom (4ESV: chain F) of the *Bst* spiral. These two
420 chains are offset owing to the distinct planar vs. spiral configurations adopted by
421 the NTD tier of the *Vc* ATPγS and *Bst* GDP•AlF_4 complexes. Unexpectedly, the
422 breaches in the two structures do not align (Figure 3). Instead, they are offset by
423 one subunit.

424 Given the distinct states captured by each structure, we reasoned that the *Vc*
425 ATPγS structure might precede the transition state *Bst* complex in the DNA
426 translocation reaction coordinate. Ordering the structures in this way specifies a
427 direction for the observed structural changes. Accordingly, the NTD of chain F and
428 chain E in the *Vc* ATPγS complex will transition from the closed triangular planar
429 configuration to the open spiral of the GDP•AlF_4 complex (mapped to 4ESV chains:
430 A and F); concomitantly, the CTD of *Vc* chain A will move upward (as in the pose
431 in Figure 3) to assume the configuration seen in chain B of 4ESV (Supplementary

432 Movie 1). With the migration of the *Vc* chain A CTD to the position specified in the
433 4ESV structure, the breach in the CTD spiral moves counterclockwise by one
434 subunit. The LH element moves from the LH3 to the LH4 position in 4ESV chain
435 A. Several lines of evidence in the *Vc* ATPγS complex support the proposal that
436 the chain A CTD migrates (Figure 3). First, the arginine finger/β-hairpin element
437 on chain F has peeled away by ~3 Å, relative to its position in chains B, C, D, and
438 E, from the P-loop on chain A (Figure 2C). Second, chain A is farther away from
439 its neighbors than any other DnaB subunit. Third, chain A makes no contact with
440 ssDNA. Lastly, of all the CTDs, the EM density for chain A is the weakest.
441 Together, these findings point to the disengagement of the chain A CTD from its
442 CTD neighbors and ssDNA as it poises to transition. Of course, the chain A CTD
443 remains linked to the DnaB hexamer through its NTD.

444 Due to the NTD layer's asymmetry, the next subunit's motion, chain F, must follow
445 a different trajectory. We propose that on ATP hydrolysis, chain F, now located at
446 the bottom of the spiral, will also peel away from DNA and migrate upwards to a
447 new binding site on ssDNA. In contrast to the motion of chain A, which results in
448 the opening of the NTD layer, the motion of chain F CTD must be accompanied by
449 the closure of the NTD ring from the open spiral to the closed planar configuration;
450 this motion will also result in the adjustment of the position of the LH element, from
451 the LH3 position to the LH1. Together, these two changes re-establish the NTD
452 configuration in the *Vc* ATPγS structure. Applying the above to chains E and D
453 first and then to chains C and B allows each DnaB subunit to complete a catalytic
454 cycle of ATP hydrolysis amid translocation on ssDNA. These findings highlight the

455 importance of opening and closing the NTD layer, which had previously been
456 suggested to specify the direction of unwinding (93) in the translocation reaction.

457 **Oligomeric State and Stoichiometry of *Vc*DnaB, DciA, ssDNA complexes**

458 Next, we used high-resolution native mass spectrometry (nMS) to determine the
459 oligomeric states and the stoichiometry of complexes in the DnaB-DciA system
460 assembled from purified proteins (Supplementary Figure 2). We first investigated
461 the oligomeric states of DnaB complexes from *Vc*. To provide context, the
462 hexameric *E. coli* (*Ec*) DnaB (22) and monomeric *B. subtilis* (*Bst*) DnaB-family
463 species (34) were included. nMS analysis showed that the *Vc* DnaB helicase is
464 hexameric (Figure 4A and Supplementary Table 5). We observed a sizeable
465 population of lower oligomeric states for *Ec* and *Vc*DnaB ($DnaB_5$, $DnaB_4$, $DnaB_3$,
466 and $DnaB_2$) in samples without Mg•ATP. The addition of a small amount of ATP
467 (10 μM ATP for a 10 μM DnaB monomer sample) before nMS analysis yielded a
468 predominant peak for the hexameric DnaB with minimal subcomplexes (Figure 4A
469 and Supplementary Table 5), indicating that ATP stabilizes the *Vc*DnaB hexamer
470 as previously suggested for the *E. coli* ortholog (94, 95). All subsequent
471 experiments with DnaB-containing samples were supplemented with 10 μM ATP
472 and 0.5 mM magnesium acetate before nMS analysis. Close-up inspection of the
473 nMS spectrum for the *Vc*DnaB sample incubated with Mg•ATP showed a peak
474 distribution corresponding to several Mg•ADP-bound states, indicating ATP
475 binding and hydrolysis (Figure 4B and Supplementary Table 5).

476 Next, we examined complexes between *Vc*DnaB, *Vc*DciA, and ssDNA derived
477 from the OriC-I chromosomal origin. Our nMS analysis showed that *Vc*DciA is
478 monomeric (Supplementary Figure 12). Incubation of 10 μM (as monomer)

479 *Vc*DnaB with 7 μM full-length *Vc*DciA, in the absence of ssDNA, revealed that the
480 DnaB hexamer bound 1 – 2 copies of DciA, with small amounts of a third copy
481 (Figure 5A). We attempted to analyze samples with higher relative amounts of
482 DciA (> 10:7 DnaB: DciA) but encountered significant disassembly of *Vc*DnaB
483 complexes with *Vc*DciA upon initiation of electrospray during nMS analysis
484 (Supplementary Figure 13). Stoichiometries of 6:3 or 6:6 for the *Vc*DnaB-*Vc*DciA
485 complex have been estimated from small-angle X-ray scattering and the X-ray
486 crystal structure (12, 14).

487 DnaB accepts ssDNA into its central chamber, the basis for the fork DNA
488 unwinding assay(12, 42, 96). Accordingly, we found that *Vc*DnaB alone could bind
489 OriC-I-derived ssDNA (Figure 5B). An nMS analysis of a mixture comprising
490 *Vc*DnaB, *Vc*DciA, and the ssDNA showed that up to three copies of *Vc*DciA could
491 be associated with ssDNA-bound DnaB. Interestingly, there is a marked increase
492 in the relative peak intensity for the 6:3 DnaB: DciA assembly when ssDNA is
493 bound compared to the ssDNA-free sample, suggesting that ssDNA association
494 promotes the formation or stabilization of this higher-order ensemble.

495 We also investigated the binding of specific *Vc*DciA domains to *Vc*DnaB. nMS
496 analysis of *Vc*DnaB titrated with increasing concentrations of the lasso domain of
497 DciA showed a progressive increase in the number bound to the DnaB hexamer,
498 with 1 – 4 copies bound when both proteins are present at equimolar amounts, to
499 2 – 6 copies bound at four-fold excess of DciA-Lasso (Supplementary Figure 14A).
500 In contrast, only one copy of the DciA KH domain was found associated with $DnaB_6$
501 at ~10% relative peak intensity even at six-fold molar excess, indicating that the

502 KH domain of DciA weakly binds to DnaB (Supplementary Figure 14B). Incubation
503 of *Vc*DnaB with the two separate DciA domains at the highest concentrations
504 studied did not change the maximum number of bound copies observed (i.e., one
505 and six for the DciA KH and Lasso domains, respectively, Supplementary Figure
506 14B). Contrary to what was observed with DnaB and full-length DciA, no DnaB
507 helicase disassembly was observed during the electrospray nMS analysis when
508 either or both DciA domains were used in excess. Moreover, the distribution of
509 DnaB: DciA-Lasso assemblies did not change (1 – 4 copies of DciA-Lasso
510 remained bound to $DnaB_6$ at equimolar amounts of both proteins) in the absence
511 or presence of ssDNA (Supplementary Figure 15).

512 Our nMS experiments revealed the stoichiometry of the isolated *Vc*DnaB helicase
513 and its complex with DciA and OriC-I-derived ssDNA; both estimates are crucial to
514 deciphering the loading mechanism. The hexameric nature of *Vc*DnaB implies that
515 it is a closed protein ring and that the DciA helicase loader is likely a ring-breaker.
516 The 6:3:1 stoichiometry of the *Vc*DnaB-DciA-ssDNA complex suggests that
517 although six DciA binding sites may exist on DnaB, only three are used; this value
518 will be crucial to understanding how the DnaB-DciA complex will interact with other
519 factors during replication initiation.

520 **_Vc_DciA Binds to Cognate DnaB Helicases with High Affinity**

521 Next, we used orthogonal approaches to show that DciA binds to cognate DnaB
522 and that DciA likely binds near the DH—LH interface (Figure 6). First, we
523 conducted NiNTA 'pull-down' experiments to examine the binding between full-
524 length and truncated constructs of DciA and DnaB (Figures 6A and Supplementary
525 Figure 16). We find that full-length *Vc*DciA binds to full-length *Vc*DnaB. Moreover,

526 DnaB constructs that span the LH and CTD domains also retain binding to full-
527 length DciA (a shorter construct spanning the CTD could not be expressed). No
528 other DnaB construct (NTD or NTD-LH) showed binding to full-length DciA.
529 Parallel experiments with constituent KH (*Vc*: 1:98) and Lasso domains (*Vc*:
530 98:157) revealed binding to full-length cognate DnaB, although the *Vc*DciA KH
531 domain bound weakly. No other truncated DnaB construct (NTD or NTD-LH)
532 showed any interaction with either the KH or Lasso domains. These data point to
533 the LH interface as a strong candidate for part of the DciA binding site, with another
534 part comprised of the CTD itself.

535 Next, we applied surface plasmon resonance (SPR) to quantify the
536 interaction between *Vc*DnaB and *Vc*DciA. We immobilized full-length DciA, the
537 isolated KH, and Lasso domains to the SPR chip, measured on and off rates for
538 full-length DnaB, and extracted dissociation constants (Figures 6B, 6C, and
539 Supplementary Figure 17). As our pull-down binding experiments anticipated,
540 *Vc*DnaB bound tightly (K_D = 0.58 nM) to full-length *Vc*DciA. We found the isolated
541 *Vc* Lasso domain bound to DnaB with a K_D = 65 nM, but the KH domain exhibited
542 a weak affinity (K_D = 170 nM) (Supplementary Figure 17).

543 Our data reveal that the most significant contacts between DciA and DnaB
544 are found at the LH and CTD domains of DnaB, with the Lasso domain being the
545 locus of many of these contacts. Given that two other loaders, *E. coli* DnaC and
546 phage λP, bind at the DH-LH interface of two adjacent DnaB subunits (19, 43, 44,
547 48), the finding that the LH constitutes the DciA binding establishes this site as a
548 conserved location of significance for DnaB helicase loading.

549 **Suppression of DnaB's ATPase Activity by DciA**

550 One of the hallmarks of a bacterial helicase loader is the suppression of ATPase
551 activity of the cognate helicase (43, 46, 60). To evaluate the effect of *Vc*DciA on
552 the ATPase activity of *Vc*DnaB, we measured the influence of full-length and
553 truncated constructs of DciA against control measurements encompassing wild-
554 type and the Walker B mutant E259A (Figure 7A). Our preparations of full-length
555 and truncated DciA lacked ATPase activity. Titration of full-length *Vc*DciA revealed
556 potent suppression of *Vc*DnaB's ATPase activity (untagged DnaB: $IC_{50} \approx 26$ nM,
557 NHis-DnaB: $IC_{50} \approx 26$ nM, Figure 7B). A construct encompassing the *Vc* KH
558 domain (1:98) exhibited an $IC_{50} \approx 443$ nM (Supplementary Figure 18A); the lower
559 inhibitory constant is congruent with the weak interaction signaled by our nMS
560 study and the NiNTA-based binding studies. Even though we found that the *Vc*
561 Lasso domain (98:157) binds to full-length *Vc*DnaB, titration revealed no effect on
562 *Vc*DnaB's ATPase activity at low DciA concentrations (25 – 400 nM). However, at
563 very high concentrations (800 – 6400 nM) of *Vc*DciA, we observed reproducible
564 stimulation (up to 2.8 x at 4800 nM) of DnaB's ATPase activity (Supplementary
565 Figure 18B).

566 **DciA Loads DnaB on Physiological DNA Bubble Substrates**

567 The nMS binding data and DNA unwinding experiments (Supplementary
568 Information and Supplementary Figures 19, 20, 21, and 22) implicate DciA as a
569 helicase loader since DciA enhances both underlying activities. However, the
570 substrates employed in the above assays (ssDNA, 5' and 3' ssDNA tailed fork) do
571 not permit self-threading into DnaB's central chamber to be distinguished from
572 loading/assembly around ssDNA. Physiologically melted DNA by DnaA at a

573 replication origin has no free termini, and, as such, assembly around ssDNA, rather
574 than threading, is expected to be the predominant form of loading *in vivo*.

575 To distinguish the DciA-mediated assembly of *Vc*DnaB on ssDNA from self-
576 threading, we measured unwinding from a DNA bubble substrate, which features
577 no free ends, unlike a tailed-fork substrate. Our assay employed DNA molecules
578 #894 and #895 previously described (42), which we converted into a FRET-based
579 readout by adding a Cy3 fluorophore at one 5' end and the Iowa Black RQ
580 quencher at the corresponding 3' end (Figure 8). We also measured DnaB loading
581 onto a doubly labeled DNA bubble (Supplementary Information and Figures 23,
582 24, 25C, and 25D).

583 No fluorescence signal was observed when DciA was omitted (Figure 8, red
584 curve), leading us to conclude that self-threading of ssDNA into DnaB had been
585 suppressed with the bubble substrate. Titration of full-length *Vc*DciA (0.11 to 6400
586 nM) revealed a 10-fold (~15 to ~150) increase in fluorescence at the highest
587 concentration (6400 nM). The increase in fluorescence strictly depended on ATP
588 since the *Vc*DnaB E259A mutant showed no activity (Supplementary Figure 24).
589 Substitution of the two DciA truncations – the NTD KH and the CTD Lasso – for
590 full-length *Vc*DciA revealed essentially no loading activity (less than 5%)
591 (Supplementary Figures 25A and 25B).

592 To better understand *Vc*DciA's loading activity, we repeated the above titration
593 without *Vc*DnaB. Surprisingly, titration of DciA against the DNA bubble substrate
594 revealed a substantial fluorescence signal (Figure 8B); these data imply that
595 *Vc*DciA has a previously undiscovered activity: to unwind dsDNA on its own. This

596 activity did not require ATP. The finding that isolated *Vc*DciA produced a
597 fluorescence signal ~66% of that seen in the *Vc*DnaB-DciA titration implies
598 significance, though establishing biological relevance will require further
599 experimentation. DciA's apparent unwinding activity is not observed when the
600 DNA bubble is substituted with the fork substrate (Supplementary Figure 22),
601 indicating a role for DNA structure in this activity.

602 We subtracted the two signals to separate the unwinding activities of *Vc*DnaB-DciA
603 and isolated *Vc*DciA (Figure 8C). The calculated signal from *Vc*DnaB, when acted
604 upon by *Vc*DciA, showed a 25-fold (~5 to ~125 RFU, Figure 8C) increase in
605 fluorescence at the highest concentration (6400 nM) (Figure 8D). These data
606 strongly argue that *Vc*DciA is a helicase loader for *Vc*DnaB.

607 The congruence of the DNA unwinding and helicase loading curves during titration
608 with full-length *Vc*DciA suggests that, to a large degree, helicase loading rather
609 than threading occurs with full-length DciA in both assays (Figure 8D and
610 Supplementary Figure 19B). On the other hand, dissimilarity in the curves
611 corresponding to the *Vc*DciA truncations implies that loading is not retained in
612 either construct or that the observed DNA unwinding activity in the truncated
613 constructs may arise solely from self-threading. Our data establish a helicase-
614 loading biochemical activity for the *Vc*DciA protein. Moreover, the finding that
615 loading onto the bubble substrate does not occur without DciA supports a closed
616 protein ring configuration for DnaB, which agrees with our nMS results (Figure 4A).

617 ## Discussion

618 Our analyses of the bacterial DciA loader and the DnaB helicase from *Vibrio*
619 *cholerae* shed new light on the underlying helicase-loading and activation pathway
620 (Figure 9). In bacteria, two copies of the DnaB replicative helicase are assembled
621 onto single-stranded DNA introduced into the replication origin by the DnaA
622 initiator protein. It is now clear that most bacteria lack an ortholog for the well-
623 studied DnaC helicase loader; instead, the DciA helicase loader appears likely to
624 be the predominant loading factor (37, 40, 41). *Vc* binds to cognate hexameric
625 DnaB with a low nM K_D. The unstructured Lasso segment mediates significant
626 binding energy to the interaction with DnaB, and an essential part of the DciA
627 binding site lies at the nexus of DnaB's DH and LH elements. Prior studies
628 suggested stoichiometries of 6:3 or 6:6 for the *Vc*DnaB-*Vc*DciA complex and a
629 binding site at the DH-LH nexus (12, 14). We find up to three copies of *Vc*DciA
630 and one copy of replication-origin-derived ssDNA bound to *Vc*DnaB. The
631 stoichiometry of the DnaB-DciA system distinguishes it from the *E. coli* DnaB-
632 DnaC and DnaB•λP complexes, which feature 6:6 and 6:5 stoichiometries,
633 respectively (19, 43, 44, 48). The unwinding activity of DnaB is significantly
634 stimulated by DciA on fork and replication origin-mimicking DNA bubble
635 substrates. The finding that isolated *Vc*DnaB is a hexamer under physiological
636 concentrations of ATP (Figure 4A) and exhibits essentially no self-loading on the
637 replication-origin mimicking DNA bubble substrate (Figure 8) leads us to conclude
638 that DciA is a ring-opening-type helicase loader.

639 Our structural analysis did not reveal the architecture of the *Vc*DnaB-*Vc*DciA-
640 ssDNA complex. Nevertheless, the structure of the ATPγS form of the DnaB-

641 ssDNA complex provides new insights into the mechanism of translocation. The
642 topologically closed NTD and distinctly configured CTD layers distinguish the
643 ATPγS state from a structure previously determined bound to the transition state
644 ATP analog GDP•AlF_4 (10) and provide a first view of nucleotide-dependent
645 conformational change during ssDNA translocation. Our model for ATP-
646 dependent translocation by DnaB extends the hand-over-hand mechanism (10) by
647 integrating cycles of opening/closing of the NTD layer, reconfiguration of the LH
648 element, and disengagement of individual CTDs from ssDNA and neighboring
649 subunits, followed by migration from the bottom to the top of the DnaB spiral to
650 new ssDNA binding sites. Migration to the top of the spiral is facilitated by the
651 engagement of its β-hairpin arginine finger with a freshly bound ATP by the DnaB
652 subunit that precedes arrival at the top of the spiral. ATP binding also stabilizes
653 contacts to ssDNA. We suggest that translocation encompasses three identical
654 sub-steps. Each sub-step involves migration of the chain A CTD (or chain E or
655 chain C) with the simultaneous opening of the NTD layer into an open spiral, as
656 seen in the GDP•AlF4 4ESV structure. Notably, the open spiral state of the NTD
657 tier would likely influence contacts with the DnaG primase (9, 97), whose complete
658 binding site on DnaB requires a closed NTD tier. In the second step, migration of
659 the next CTD (chain F, chain D, or chain B) in sequence, newly at the bottom of
660 the spiral, is accompanied by the closure of the NTD layer to the triangular planar
661 arrangement seen in the *Vc* ATPγS structure. Our model specifies that two DnaB
662 subunits move in sequence and that this program of motion is repeated thrice
663 around the hexamer.

664 The precise mechanisms associated with ATP dynamics in ring-shaped oligomeric
665 ATPase are of intense interest (10, 22, 28, 29, 98–102). Substantial evidence has
666 established sequential ATP hydrolysis during rotary catalysis by the ATP synthase
667 (103, 104). Within the AAA+ family of ATPases, the picture is far less clear, with
668 studies pointing to sequential, stochastic mechanisms, both simultaneously
669 (reviewed in reference (105)) or a concerted mechanism (106). Our proposal that
670 two adjacent DnaB subunits undergo nucleotide dynamics and motion in sequence
671 is compatible with sequential or stochastic mechanisms, as it disfavors a concerted
672 scheme. Additional studies will be required for a more precise answer.

673 To link the significant findings of our work in DciA-mediated loading and
674 subsequent translation by DnaB, we looked to another ring-opener, DnaC, to
675 provide models for other steps in the helicase loading pathway (Figure 9). The
676 configuration of DnaB in the *E. coli* DnaB-DnaC•ssDNA (PDB: 6QEM) complex
677 (19) closely resembles that of the 4ESV GDP•AlF_4 state (10), with a closed spiral
678 CTD and open spiral NTD and contacts to ssDNA by each subunit. DnaB in the
679 6QEM and 4ESV structures is nearly identical. Thus, on the departure of the
680 loader, DnaB enters the two-subunit motion (Figure 9E-F) scheme proposed
681 above. Notably, the departure of the DciA loader produces a DnaB configuration
682 after it has taken the first of the two sequential steps described above (Figure 9D).
683 We suggest that after the eviction of the loader, the subunit at the bottom of the
684 spiral will take the second of these steps to migrate to the top of the spiral (Figure
685 9E-F). Repetition of the sequenced motions of two DnaB subunits around the ring
686 accompanies further translocation along ssDNA.

687 A crystal structure of the 6:6 *Vc*DnaB-*Vc*DciA complex implies two distinct DciA
688 binding modes and a nearly closed planar DnaB ((14) and Supplementary
689 Information and Supplementary Figures 26 and 27). Additional studies will be
690 required to sequence the binding modes in this structure and others that might be
691 present in the helicase loading reaction.

692 An important unanswered question centers on the mechanism of expulsion of DciA
693 from the DnaB-ssDNA complex. The DnaC (19, 60, 107) and λP (108, 109)
694 systems feature biochemical programs to mediate loader dissociation. Our data
695 reveal a tight interaction between helicase and loader (Figure 6) that suppresses
696 DnaB's ATPase activity (Figure 7). Yet, DciA exhibits a dose-dependent
697 stimulation of DnaB's unwinding activity (Figure 8 and Supplementary Figure 19),
698 absent any other factor. These findings suggest that DciA may spontaneously
699 dissociate to relieve inhibition of DnaB's ATPase activity and enable unwinding
700 activities. It is also possible that interactions with other replisome components (25,
701 107, 110) could contribute to the eviction of DciA. Future studies will have to clarify
702 this question.

703

704 **Data Availability**

705 Coordinates for the EM-derived model of the *Vc*DnaB-ssDNA-ATPγS
706 complex are available from the RCSB Protein Data Bank under accession codes
707 9DLS. Cryo-EM maps are available from the EMBD under the accession code
708 EMD-46984.

709 **Funding**

710 This work was supported by the National Science Foundation (DJ: MCB
711 1818255), the Fondazione Cariplo (RM: grant #2020–3589), the Italian Ministry of
712 University and Research (RM: PRIN 2022, grant #2022LCN738), and the
713 Department of Education (NGao: PA200A150068). The nMS work is supported
714 by funding from the National Institutes of Health P41 GM109824 and P41
715 GM103314 to BTC. Some of this work was performed at the Simons Electron
716 Microscopy Center and National Resource for Automated Molecular Microscopy
717 located at the New York Structural Biology Center, supported by grants from the
718 Simons Foundation (SF349247), NYSTAR, and the NIH National Institute of
719 General Medical Sciences (GM103310) with additional support from Agouron
720 Institute (F00316), NIH (OD019994), and NIH (RR029300).

721 **Author Contributions**

722 NGao, DM, RM, and DJ conceptualized the study. NGao designed and
723 prepared all the proteins. NGao and DM performed the ATPase assays. NGao
724 performed the pull-down assays. NGouda, ST, AM, AChowdhury, ACerullo, and
725 HB assisted with various laboratory experiments. DM performed the fluorescence-
726 based DNA unwinding and helicase loading assays. DM and CM performed the
727 surface plasmon resonance analyses. All nMS analyses were performed by PDBO
728 in the BTC lab. AP and NGao acquired the cryo-EM data and performed the initial

data analysis. DM analyzed the cryo-EM data. DM built and analyzed the cryo-EM structure. NGao, DM, RM, and DJ drafted the manuscript, working with FR and MR.

Acknowledgments

We thank the Jeruzalmi and Miggiano lab members, the City College biophysics group, the CUNY Advanced Science Research Center, and the New York Structural Biology Center for their scientific and technical advice. We also thank Professor Anuradha Janakiraman for excellent scientific discussions and technical assistance.

Conflicts of Interest

The authors have no financial or non-financial conflicts of interest.

741 ## Figures/Figure legends

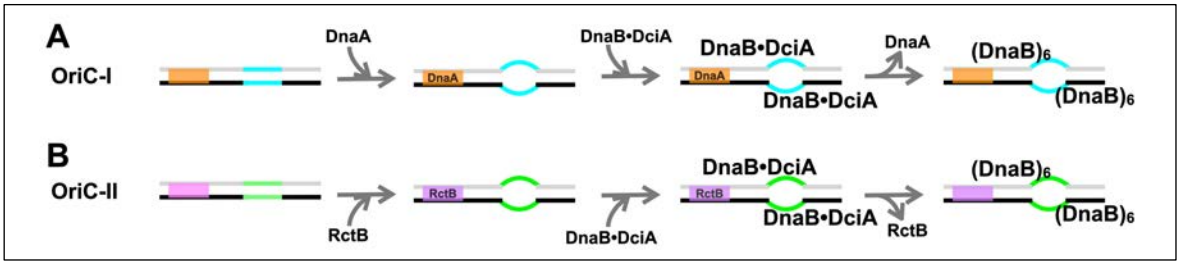

742 **Figure 1. Initiation of DNA Replication in *Vibrio cholerae*.** The primary (A) and
743 secondary chromosomes (B) in *Vibrio cholerae* initiate replication via related but
744 distinct mechanisms. Multiple copies of the replication initiator protein (OriC-I:
745 *Vc*DnaA; OriC-II: *Vc*RctB) recognize sites on dsDNA (OriC-I: orange, OriC-II:
746 purple) and oligomerize into a protein-DNA ensemble. Assembly of the initiator-
747 origin DNA complex promotes the melting of an A-T-rich segment at the origin,
748 termed the DNA unwinding element (DUE, OriC-I: cyan, OriC-II: green). The
749 melted DUE segment provides the sites for the *Vc*DciA loader to load the *Vc*DnaB
750 replicative helicase.

751

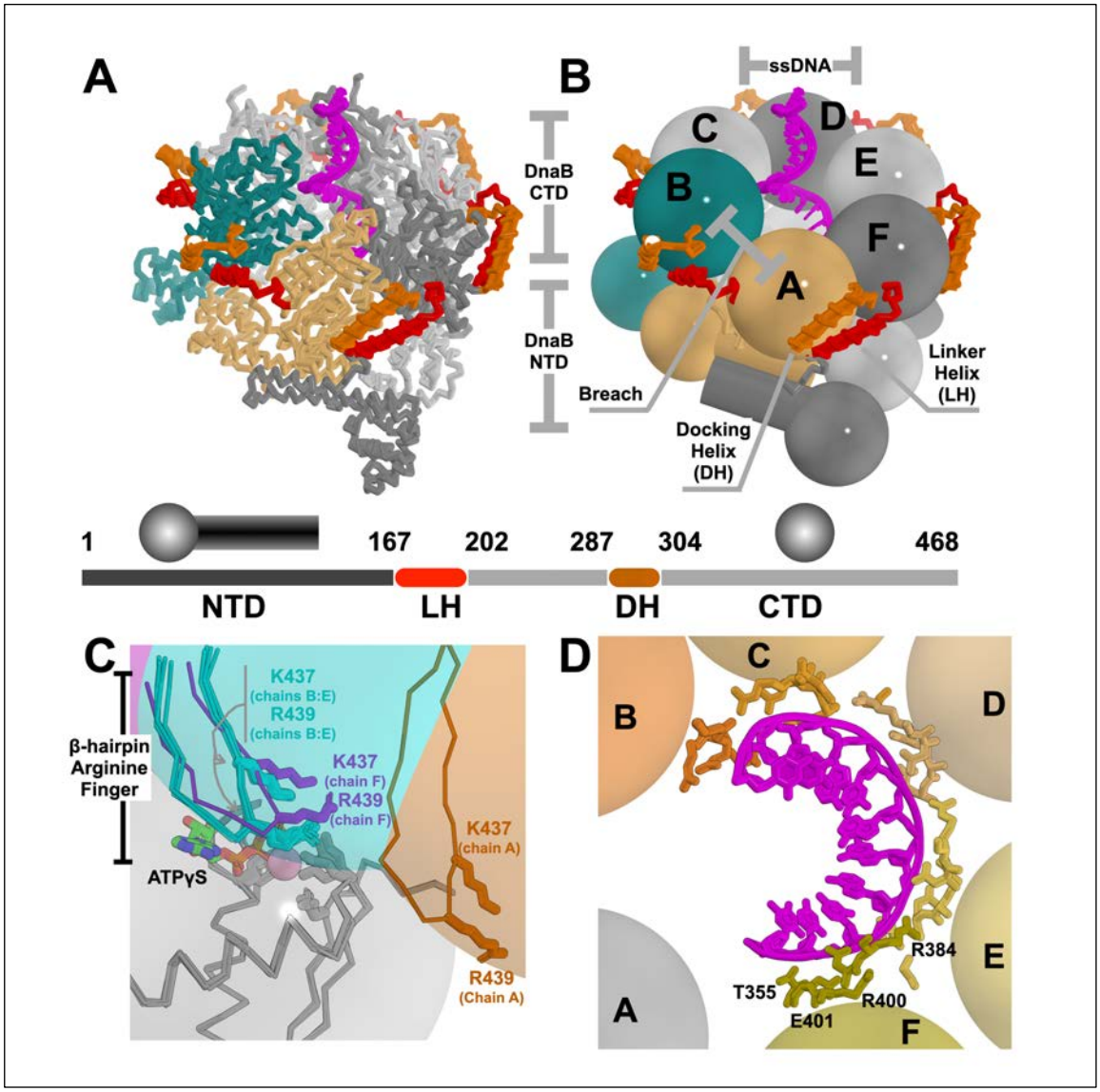

752 **Figure 2. The *Vc*DnaB-ssDNA-ATPγS Complex and Its Interactions with**
753 **Nucleotide and ssDNA.** The *Vc*DnaB-ssDNA-ATPγS is drawn in a ribbon
754 representation (A) or a schematic using a design language wherein the NTDs are
755 depicted as a mushroom shape and the CTDs as spheres (B). In panels A and B,
756 ssDNA, colored in magenta, is depicted in a cartoon and stick representation. The
757 breach in the CTD layer is between chain A (light orange) and chain B (deep teal);
758 other DnaB subunits are colored in alternating shades of gray. The Docking Helix
759 (DH) and the Linker Helix (LH) are depicted as cylinders and ribbons colored

760 orange and red, respectively. The primary sequence of *Vc*DnaB is depicted as a
761 bar, with the salient domain boundaries indicated. C) Close-up of the ATP catalytic
762 center at the interface between each pair of DnaB CTDs. ATP is depicted in the
763 stick representation. The six DnaB CTD pairs, depicted here as spheres, are
764 superimposed on the subunit (colored in grey) that harbors the Walker A and B
765 motifs (not indicated). For clarity, only a portion of the superimposed CTD is shown
766 as a ribbon; the grey sphere shows the full extent of the superimposed CTD.
767 Spheres corresponding to the CTDs excluded from the superposition are colored
768 in purple (chain F), cyan (chains B:E), and orange (chain A). The β-hairpin arginine
769 fingers from all six non-superimposed CTDs are shown in the ribbon format.
770 Although excluded from the superposition, the β-hairpin four corresponding to four
771 chains (chains B, C, D, and E, cyan) superimpose closely. In contrast, chains F
772 (purple) and A (orange) are found ~3 Å and ~19 Å, respectively. D) Schematic
773 representation of the *Vc*DnaB-ssDNA interface. The DnaB CTDs are represented
774 as spheres, labeled by the chain, and colored in shades of yellow/orange, except
775 for chain A, which is colored gray. The ssDNA is drawn in a cartoon and stick
776 representation and colored purple. Additional details on the *Vc*DnaB-ssDNA
777 complex can be found in Supplementary Figures 7, 11, and Supplementary Table
778 4.

779

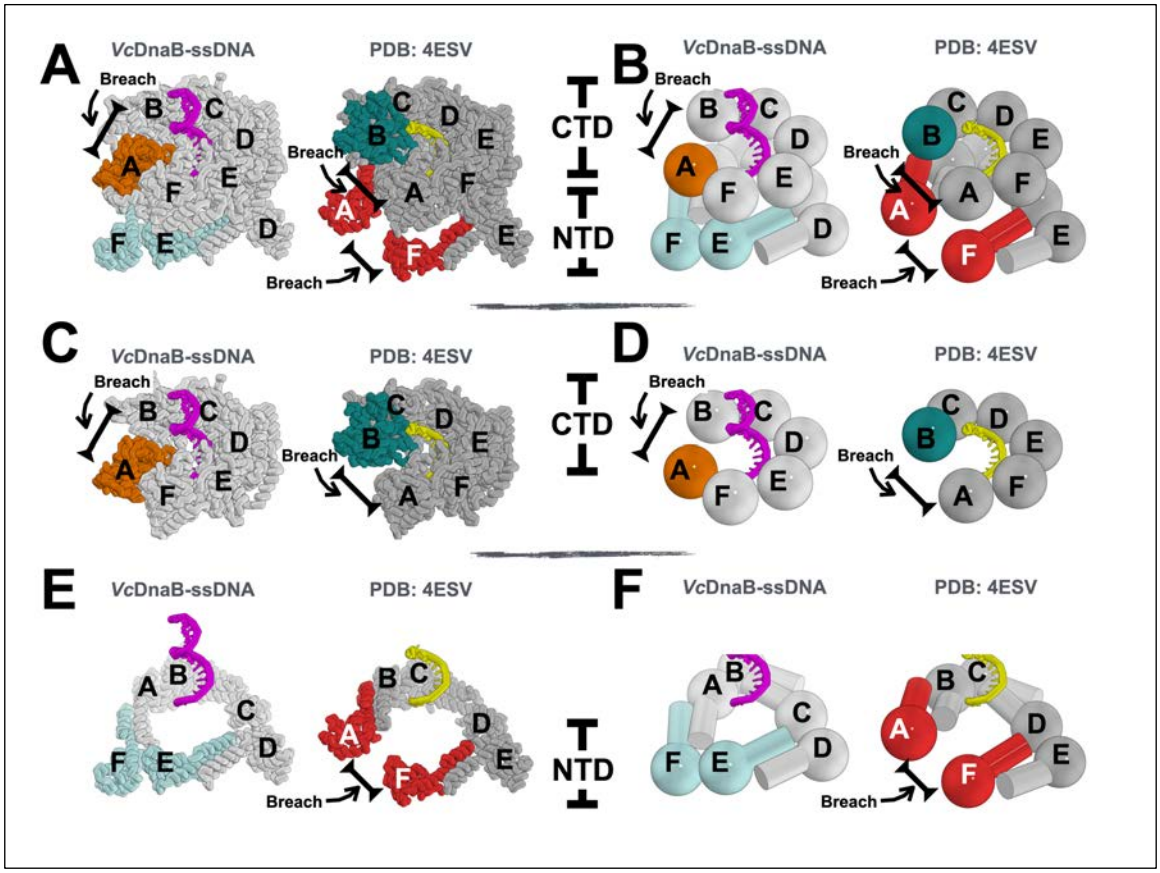

Figure 3. Nucleotide-Dependent Conformational Differences in the *Vc*DnaB-ssDNA-ATPγS and *Bst*GDP•AlF$_4$ complexes. The two complexes are superimposed in all panels, as described in the main text. For clarity, the two entities have been translated with respect to each other, allowing each to be visible. A) Ribbon representation of both complexes. *Vc*DnaB NTD components chain F and E in the closed planar and triangular configuration are colored in pale cyan. *Bst*DnaB NTD components chain A and F in the open spiral configuration are colored in red. *Vc*DnaB chain A is colored orange. 4ESV chain B is colored deep teal. The ssDNA in the *Vc* and *Bst* complexes is depicted in both cartoon and stick representations, colored purple and yellow, respectively. All other chains of DnaB are colored in light gray (*Vc*) and dark gray (*Bst*). The breaches in the

NTD and CTD layers are indicated. Chains corresponding to the N-terminal domain (NTD) and C-terminal domain (CTD) components are labeled. B) The depiction is identical to that in panel A, except that the NTD and CTD layers are represented using the sphere and mushroom-like shape design language. C) The exact representation as panel A, except that only the CTD layer is shown. D) Identical depiction as panel C except that the DnaB CTD layers are depicted as spheres. E) The exact representation as panel A, except that only the NTD layer is shown. F) Identical depiction as panel E except that the DnaB NTD layers are depicted using mushroom-like shapes.

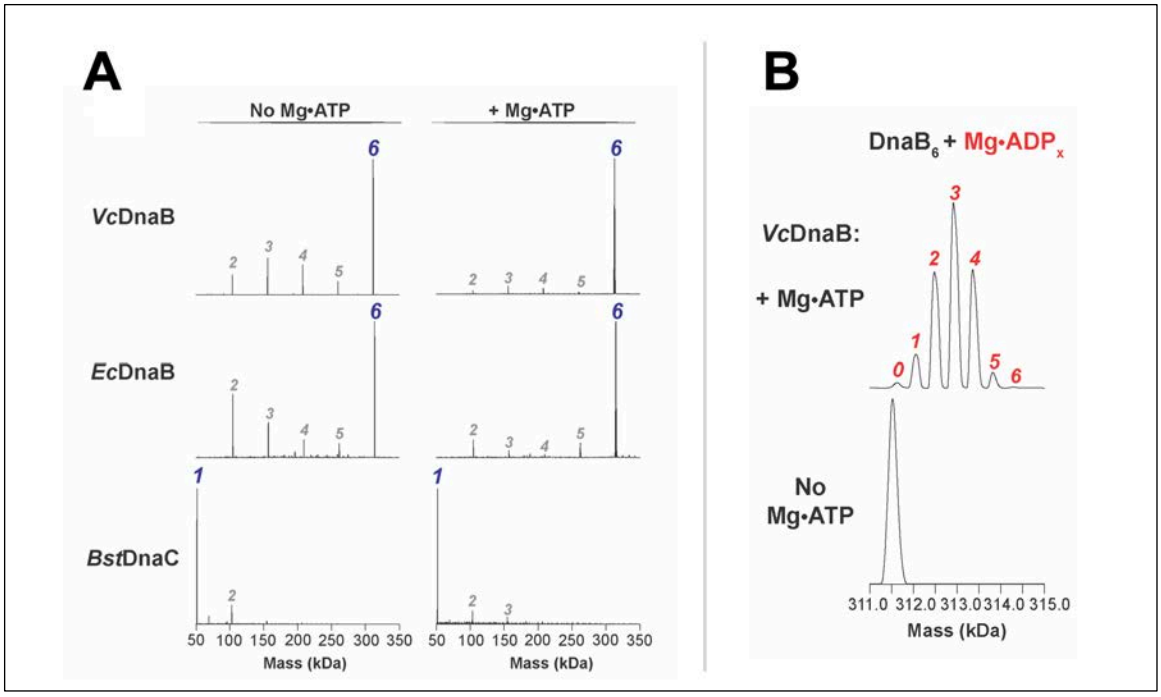

Figure 4. Although highly conserved, certain DnaB helicase orthologs feature distinct oligomeric states. (A) Deconvolved nMS spectra of replicative helicases from *V. cholerae* (*Vc*), *E. coli* (Ec), and *B. subtilis* (*Bst*) with and without Mg•ATP. Unlike the *B. subtilis* ortholog, which is monomeric (with or without ATP), *V. cholerae* and *E. coli* DnaB are hexamers. Each measurement was performed with a monomeric protein concentration of 10 μM. The *Bst*DnaC sample refers to the DnaB family helicase in *B. subtilis*. (B) Close-up of panel A peaks corresponding to the hexameric *Vc*DnaB complex. The average mass difference between adjacent peaks is 444 ± 20 Da; this value more closely matches the mass of ADP (Mass = 427 Da) than ATP (Mass = 507 Da). As such, we suggest that ATP hydrolysis has occurred, resulting in distinct Mg•ADP-occupied states. The numbers in panels A and B refer to the oligomeric state of *Vc*DnaB (A, blue) and of Mg-ADP molecules bound to *Vc*DnaB (B, red). A list of mass assignments of

814 the various nucleotide-bound peaks in panels A and B appears in Supplementary

815 Table 5.

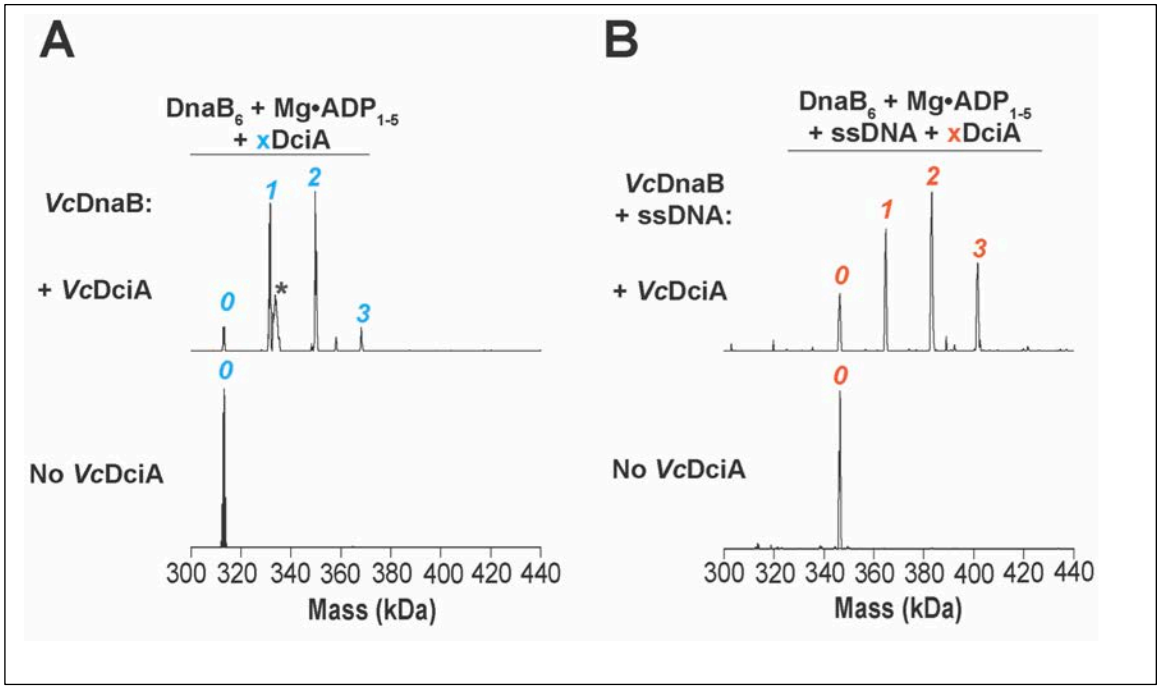

816 **Figure 5. Up to Three Copies of *Vc*DciA Bind to Isolated Hexameric *Vc*DnaB**
817 **and *Vc*DnaB Complexed to Replication Origin-Derived ssDNA.** Deconvolved
818 nMS spectra of 10 μM *Vc*DnaB (measured as the monomer) without and with 7
819 μM full-length *Vc*DciA (A) and in the absence or presence of 3 μM origin-derived
820 ssDNA (O4-*Vc*-F) (B). The number of *Vc*DciA molecules observed bound to
821 *Vc*DnaB is indicated in blue (A) or red (B). The expected masses include $DnaB_6$
822 = 311.5 kDa, DciA = 18.4 kDa, and ssDNA = 32.5 kDa. The broad peak (*) is from
823 an unknown low-level protein contaminant introduced during or after buffer
824 exchange for this sample. -All samples were exchanged into 10 μM ATP, 500 μM
825 magnesium acetate, 500 mM ammonium acetate, and 0.01% Tween-20 before
826 nMS analysis.

827

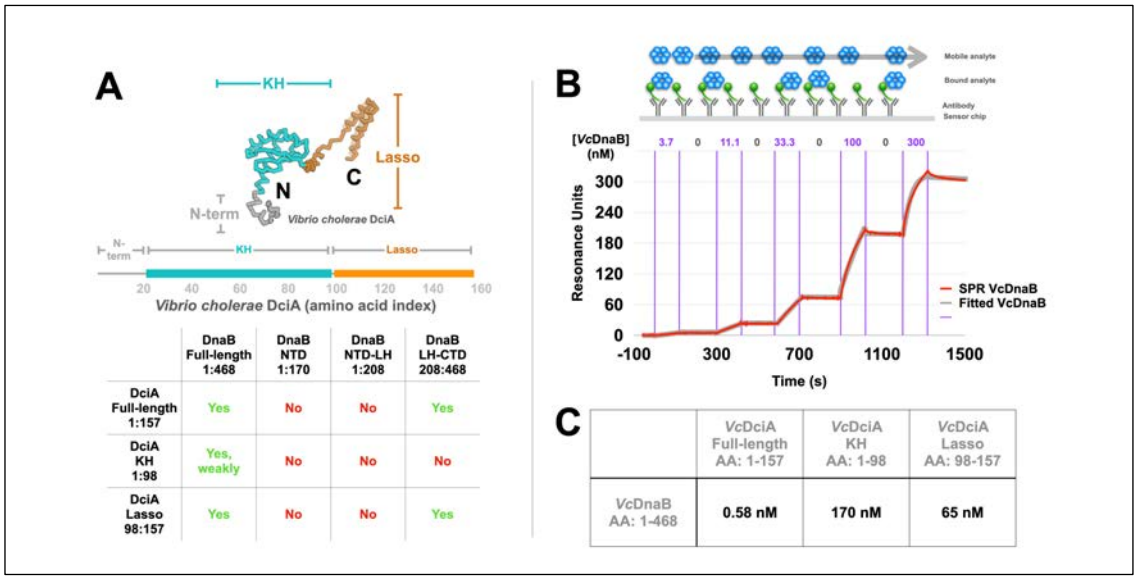

	DnaB Full-length 1:468	DnaB NTD 1:170	DnaB NTD-LH 1:208	DnaB LH-CTD 208:468
DciA Full-length 1:157	Yes	No	No	Yes
DciA KH 1:98	Yes, weakly	No	No	No
DciA Lasso 98:157	Yes	No	No	Yes

	*Vc*DciA Full-length AA: 1-157	*Vc*DciA KH AA: 1-98	*Vc*DciA Lasso AA: 98-157
*Vc*DnaB AA: 1-468	0.58 nM	170 nM	65 nM

Figure 6. The *Vc*DciA loader Binds Tightly to *Vc*DnaB helicase. A) The primary sequence of *Vc*DciA is arranged as a bar, and the locations of the KH and Lasso domains are indicated. The table summarizes the NiNTA 'pull-down' experiments, wherein the green 'yes' and red 'no' indicate that the pull-down assay was scored to report binding or no binding, respectively (Supplementary Figure 15). B) The dissociation constants (K_D) between DnaB and DciA were evaluated through single-cycle kinetic analyses *via* Surface Plasmon Resonance (SPR). On and off rates of full-length DnaB at incremental concentrations (3.7, 11.1, 33.3, 100, 300 nM) were measured by immobilizing cognate C-term His-tagged full-length *Vc*DciA (C; K_D = 0.59 nM; Chi^2 = 4.33; R_{max} = 312.3) on the SPR sensor chip. A schematic of the SPR experiment accompanies the raw (red) and fitted (grey) SPR curves. Experimental data were analyzed as described in the methods. The same approach was applied to measure K_Ds for the KH and Lasso constructs (Supplementary Figure 17). C) The K_D values emerging from the SPR analysis are summarized for the *Vc* system in tabular form.

843

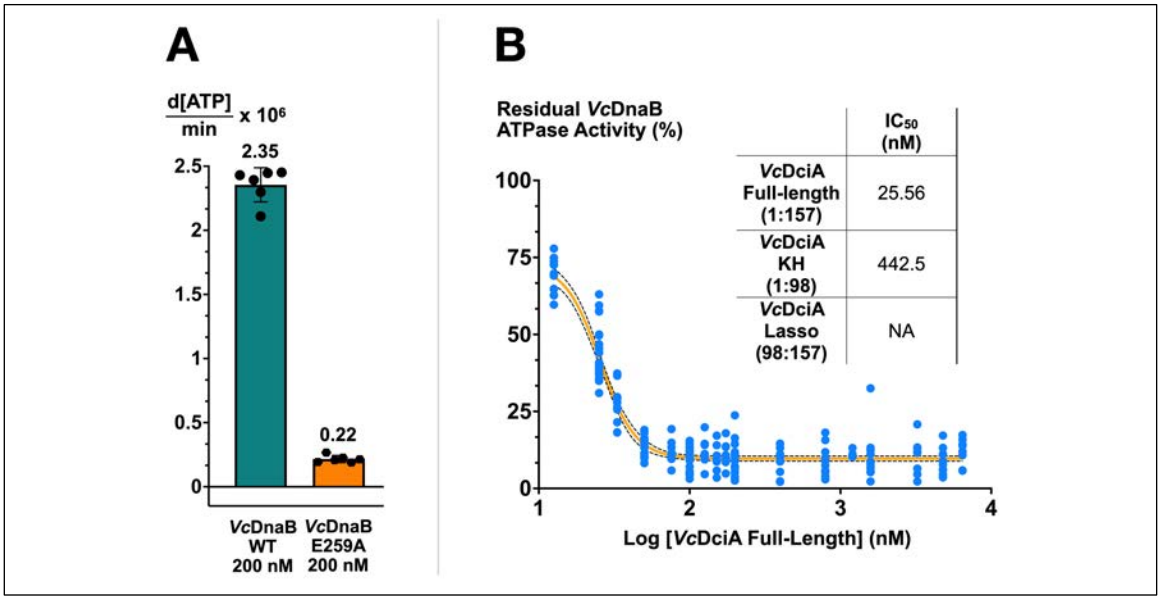

Figure 7. The full-length DciA loader suppresses VcDnaB's ATPase activity. A) ATPase rate of 200 nM wild type (teal) and E259A mutant *Vc*DnaB (orange). The points represent the measured rates; the height of the bar represents the average of the measured points; the vertical bracket visually represents one standard deviation. Each experiment in panel A was performed two times in triplicate. B)The effect of titrating *Vc*DciA (0 - 6400 nM, log scale) on the residual ATPase activity of *Vc*DnaB (200 nM) is plotted. For each experiment, the residual activity is the quotient of the ATPase rate of a particular DciA concentration and the rate for 0 nM DciA. The blue points represent seven experiments with different batches of *Vc*DnaB and *Vc*DciA measured in triplicate on various days. The light-orange line represents the non-linear fit of the residual activity points (Sigmoidal, 4PL, X is log (concentration) model in Prism. The dotted lines represent the 95% confidence interval. The fit encompassed 210 points, yielded an R^2 value of 0.91, and resulted in an IC_{50} value of 25.56 nM (95% CI = 23.74 to 26.94 nM). Parallel analysis with the KH domain on four different batches revealed a 16-fold higher

859 IC_{50} of 442.5 nM (R^2 = 0.9693; 95% CI: 380.5 to 520.0 nM). The Lasso domain
860 was not found to inhibit; however, we observed activation of DnaB's ATPase at
861 very high Lasso concentrations. The inset table summarizes the IC_{50} results.
862 Control measurements with the E259A *Vc*DnaB Walker B mutant exhibited no
863 ATPase activity (panel B, orange).

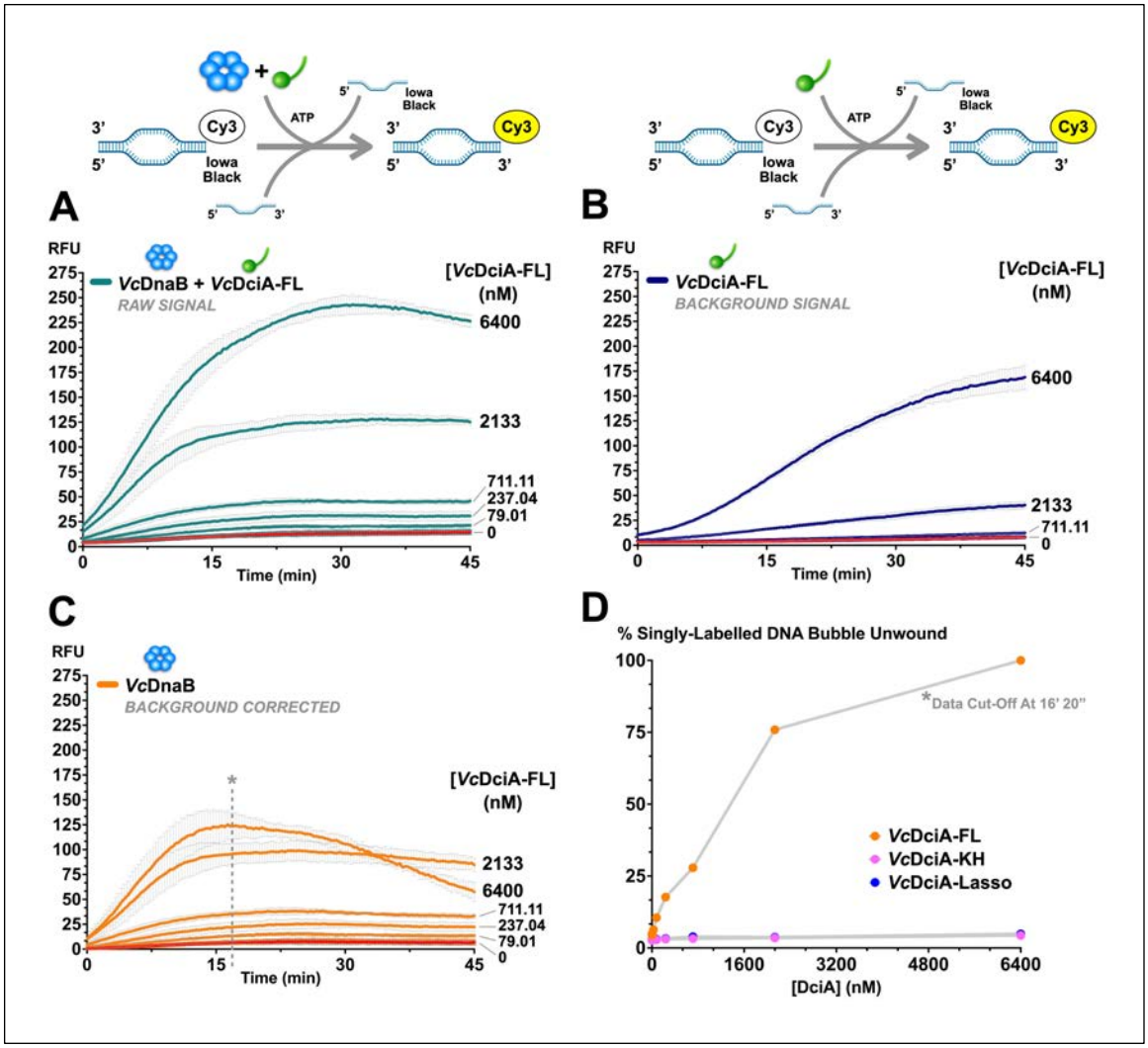

Figure 8. *Vc*DnaB is loaded onto a physiological DNA bubble substrate by the full-length *Vc*DciA loader. Helicase loading was measured using a DNA substrate that mimics unwound DNA at a replication origin, as is diagrammed in the schematic above. A) Loading of full-length *Vc*DnaB by full-length *Vc*DciA. Loading is read out by measuring fluorescence (in relative fluorescence units, RFU) over 45 minutes at 570 nm from a DNA substrate after it had been unwound by DciA-loaded DnaB; loading relieves the quenching to provide a signal. Data were taken by titrating *Vc*DciA-FL (0.11-6400 nM) against *Vc*DnaB (200 nM). Each labeled curve represents the average of 6 independent measurements taken from

873 different batches of proteins on different days. The lack of loading activity in the
874 curve that omits *Vc*DciA (red curve) implies that DnaB's self-threading activity has
875 been suppressed with the replication-origin mimicking DNA bubble substrate. The
876 standard deviation of each point is plotted in light gray. B) Same as Panel A except
877 that *Vc*DnaB is omitted. Envisioned as a control, this measurement teaches that
878 *Vc*DciA appears to have the capacity to unwind bubble DNA on its own. C) Point-
879 by-point subtraction of the curves in panels A and B estimates the bubble
880 unwinding signal that arises solely from *Vc*DnaB. The downward phase of the
881 6400 nM DciA curve after 16 minutes arises from unwinding rate differences
882 between *Vc*DnaB and *Vc*DciA. These data suggest that *Vc*DciA stimulates the
883 loading of *Vc*DnaB by ~25-fold, ranging from 5 to 125 RFU. D) The unwinding
884 data in panel C is converted to a percentage unwound by dividing by the maximum
885 RFU point and plotting the resulting values against *Vc*DciA concentration. Parallel
886 measurements reveal that the isolated *Vc*DciA KH and Lasso domains
887 (Supplementary Figure 25A and 25B) exhibit little (less than 5%) to no loading
888 activity.
889

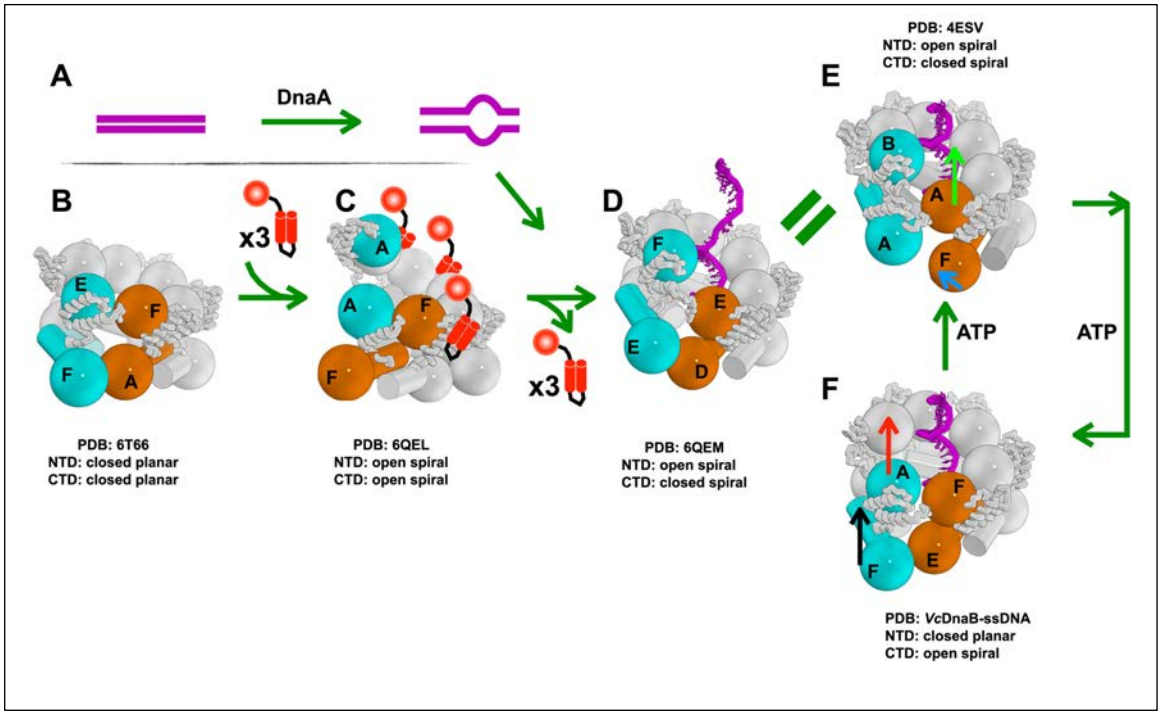

Figure 9. Model for Loading of DnaB by DciA and Translocation of DnaB on ssDNA. A) The DnaA protein binds to the replication origin and promotes melting into a DNA bubble. B) The hexameric closed planar DNA-free *Vc*DnaB (PDB: 6T66 (12)) provides a ground state model for the loading pathway. C) Our data suggest that up to 3 DciA loaders (red) bind to *Vc*DnaB; we suggest that DnaB adopts an open spiral configuration analogous to that seen with the DnaC/λP complexes (19, 43, 44, 48). D) Remodeling of this complex accompanies the entry of DnaA-generated ssDNA into the central chamber of DnaB. The current structures suggest that the D and E conformations are identical (19). We suggest that DnaB populates the two states captured in the GDP•AlF_4 (E) and ATPγS (F) conformations during translocation. The first translocation step (panel F to panel E) involves opening the NTD tier and the migration of a CTD in the ATPγS complex to its position in the GDP•AlF_4 complex. The ATPγS-chain F NTD shifts (black arrow) in position to the location of the GDP•AlF_4-chain A. Opening of the NTD

904 layer is accompanied by upward migration by 25 Å of the cyan CTD chain A in the
905 ATPγS complex (panel F, red arrow) to the position occupied by chain B in the
906 GDP•AlF_4 complex (panel E); this represents the first translocation step. In the
907 second step (panel E to panel F), the GDP•AlF_4-NTD layer (chain F) returns (blue
908 arrow) to the ATPγS-closed planar configuration (chain E). This change is
909 accompanied by a 25 Å upward migration of the orange CTD chain A in panel E to
910 a new position (chain F) in panel F (green arrow). Repetition of these two steps
911 around the DnaB enables each subunit to translocate. We suggest that the DciA-
912 loaded DnaB-ssDNA complex, which resembles the GDP•AlF_4 conformation,
913 enters this cycle and then transitions to the ATPγS state. The DnaB models in
914 panels B-F are colored in white except for certain blue and orange CTDs and NTDs
915 that line the various breaches, except for the closed planar entity.

916

Supplementary Information

Assembly of Hexameric Helicases on Nucleic Acid Substrates

Cells apply three broad strategies to load hexameric helicases onto nucleic acid substrates: ring-opening, ring-forming, and ring-closing (1–3); the terms refer to the initial state of the helicase. These schemes encompass loading onto ssDNA, ssRNA, and dsDNA. In the ring-opening scheme, closed-ring hexamers, e.g., *E. coli* DnaB, are opened by helicase loaders, such as *E. coli* DnaC (4–6) or phage λP (7–9), and assembled on ssDNA formed at the cognate replication initiator–origin DNA complex. In the ring-forming scheme, the hexameric helicase is assembled on ssDNA from monomers, either spontaneously as with the LT-antigen or E1 helicases or through the activity of a helicase loader such as DnaI, which loads the DnaB family helicase in *B. subtilis* (10, 11). The ring-closing scheme is observed with the bacterial Rho and the eukaryotic MCM2-7 hexameric replicative helicases (reviewed in (1–3)). In the Rho helicase, ring closure is mediated by the entry of the nucleic acid substrate. In the MCM2-7 ensemble, dsDNA is deposited via the chaperone origin recognition complex and associated factors. The scheme(s) the DciA loader uses to assemble DnaB onto the origin-DNA are unknown.

*Vc*DnaB Primarily Contacts the Phosphate Backbone of ssDNA

*Vc*DnaB subunits use seven residues (Asn353, Thr355, Asn383, Arg384, Arg400, Glu401, and Gly403) to contact the ssDNA backbone, though not every chain uses every residue; one contact is seen to contact a nucleobase (chain D Asn353 and N2 of G5). The segment of ssDNA within DnaB's central chamber is arranged with 11-12 nucleotides per turn of ssDNA and a pitch of ~32 Å, a value that compares well with the pitch (~33.4 Å) displayed by the DnaB CTD spiral. The approximate

942 match in pitch between protein and ssDNA spirals implies that corresponding DNA
943 binding residues on each subunit make equivalent contacts with the ssDNA
944 backbone (12) (Supplementary Figure 11 and Supplementary Table 4).

945 *Vc*DciA Stimulated Unwinding by *Vc*DnaB Measured Using a Replication 946 Fork-Mimic

947 Every bacterial helicase loader stimulates the DNA unwinding activity of its
948 cognate DnaB helicase. To investigate the influence of DciA on cognate DnaB,
949 we applied an ensemble FRET-based DNA unwinding assay wherein a DNA
950 replication fork mimicking substrate (5) is fitted with a Cy3 labeled nucleobase
951 Watson-Crick-Franklin paired with a nucleobase conjugated to the BHQ2
952 quencher; the unwinding of the fork substrate is readout by recording appearance
953 of a fluorescent light signal at 570 nm (Supplementary Figure 19). This assay
954 showed that 200 nM *Vc* DnaB exhibited measurable albeit low DNA unwinding
955 activity. However, titration of full-length *Vc* DciA (0.11 to 6400 nM) revealed a 10-
956 fold (15 to 150) increase in fluorescence at the highest concentration (6400 nM)
957 (Supplementary Figure 19A). Unwinding depended on ATP and was significantly
958 reduced in the *Vc*DnaB Walker B mutant E259A (Supplementary Figure 20).
959 Parallel analysis of the isolated DciA KH and Lasso domains implied retention of
960 about 30% of the activity of the full-length *Vc*DciA to activate the helicase.
961 (Supplementary Figures 19B and 21).

962 *Vc*DciA Stimulated Unwinding by *Vc*DnaB Measured Using a Doubly Labeled 963 DNA Bubble Substrate

964 The bubble DNA substrate (Figure 8 and Supplementary Figure 23), in principle,
965 permits the loading of DnaB onto both single strands, leading to unwinding in both
966 directions; however, the bubble substrate above with the single FRET pair only

967 reports on activity at one end of the DNA. To examine activity at both ends, we
968 repeated the helicase loading assay with a bubble substrate that featured the
969 above FRET pairs at both termini. Full-length DciA and the two truncated
970 constructs displayed the same pattern of activity as seen with the singly labeled
971 substrate (Supplementary Figures 23, 25C, and 25D). Full-length DciA produced
972 10% more fluorescence on the doubly labeled substrate instead of the expected
973 doubling of the signal. This discrepancy may be due to unexpected quenching
974 between the two ends of the molecule due to conformational switching that brings
975 them closer together. Alternatively, loading two DnaB molecules may be more
976 complex than previously thought.

977 **Comparison to other structures of *Vc*DnaB**

978 We compared our cryo-EM *Vc*DnaB structure to three previously
979 determined crystal structures: 6T66, 7QXM, and 8A3V. None feature ssDNA
980 (6T66, 7QXM), and one includes DciA at a 6:6 ratio with DnaB (8A3V). We
981 compared the structures for subunit proximity, ring breaches, nucleotide
982 occupancy, the β-hairpin/arginine finger disposition, and LH position.

983 The 6T66 structure (13) presents as a planar hexamer in the
984 crystallographic asymmetric unit with a dilated NTD layer and a constricted CTD
985 tier (Supplementary Figure 26A). The DnaB subunits in this structure are labeled
986 A-B-C-D-E-F, counterclockwise down the CTD axis. Two of the CTDs (A – F: 35.1
987 Å and D – E: 36.4 Å) are 2-3 Å further away from their neighbors than the
988 disposition of other subunit pairs (A–B: 32.8 Å; B–C; 32.7 Å; C–D: 32.7 Å; E– F:
989 33.1 Å), implying two breaches in the CTD layer; the NTD layer is not breached.
990 In the *Vc*DnaB-ssDNA complex, chain A, at the bottom of the spiral, is further away

991 (A–B: 39.6 Å; F–A: 34.6 Å) from its neighbors than other pairs (average: ~33.4 Å).
992 The significance of two breaches in non-consecutive subunits in the CTD tier in
993 the 6T66 structure remains to be understood.

994 The nucleotide-binding site of each subunit in 6T66 is populated with
995 GDP•AlF_4/Mg^{2+}. However, the β-hairpin/arginine finger elements that complete
996 these binding sites populate three positions. The distance between the P-loop
997 lysine 234 and arginine finger 439 at the sites between chains D to E (18.7 Å) and
998 F to A (16.0 Å) is considerably longer than the corresponding values for other
999 subunit pairs (A–B: 10.9 Å; B–C: 11.2 Å; C–D: 11.1 Å; E–F: 11.3 Å). Naturally,
1000 longer distances are seen in CTDs that are further apart (Supplementary Figure
1001 26C).

1002 We next examined the positions adopted by the LH element in the 6T66
1003 hexamer. Alignment of the CTD onto the chain A CTD, but omitting the DH and
1004 LH elements from the calculation (resid 204:465 and not (resid 287:304 or resid
1005 178:205)) produces an average RMSD = 0.74 Å. In this alignment, the LH
1006 elements populate two positions (LH1 and LH2 above). The LH elements from
1007 chains A and E populate positions closely related to LH2; the rest are seen in the
1008 LH1 position (Supplementary Figure 26D). The subunit pairs with divergent
1009 dispositions and arginine fingers populate the LH2 position; the rest are in LH1.

1010 The 7QXM *Vc*DnaB crystal structure features an unliganded planar
1011 hexamer in the asymmetric unit (14). The DnaB subunits in this structure are
1012 labeled A-F-E-D-C-B, counterclockwise down the CTD axis. The NTD layer is
1013 dilated and follows NTD layers from 6T66 and the *Vc*DnaB-ssDNA complex. The

1014 CTD layer is constricted, with individual CTD further away from each other than in
1015 6T66 or the *Vc*DnaB-ssDNA complex (A–B: 33.7 Å; B–C: 37.0Å; C–D: 33.7 Å, D–
1016 E: 36.3; E–F: 33.6 Å; F–A: 37.9 Å). Likewise, the P-loop lysine to arginine finger
1017 distances are variable (A–B: 21.1 Å; B-C: 16.8 Å; C–D: 20.4 Å, D–E: 15.7 Å; E–F:
1018 20.9 Å; F–A: 17.3 Å). The observed variability in the disposition of CTDs in 7QXM
1019 may reflect the underlying lack of nucleotide to organize and stabilize inter-CTD
1020 contacts via the β-hairpin arginine finger. The LH elements in 7QXM populate two
1021 positions, LH2 (Chains B, D, and F) and another position (Chains A, C, and E),
1022 which are unique to this structure.

1023 The 8A3V *Vc*DnaB-DciA crystal structure has two DnaB subunits and two
1024 DciA molecules in the crystallographic asymmetric unit (15). Applying
1025 crystallographic symmetry generates a 6:6 DnaB: DciA entity, revealing a dilated
1026 NTD layer and a constricted CTD layer. The nucleotide site of each *Vc*DnaB CTD
1027 is filled with ADP. In the *Vc*DnaB$_2$: *Vc*DciA$_2$ asymmetric unit, the inter-CTD
1028 distance is ~32 Å, and the P-loop to arginine finger distance is 12.3 Å. The LH
1029 elements in 8A3V occupy the LH1 position (Supplementary Figure 27).

1030 Although parallels could be drawn between the 6T66, 7QXM, and 8A3V
1031 structures and the present *Vc*DnaB-ssDNA structure, additional studies will be
1032 required to sequence them precisely in the reaction coordinate.

1033 **Structural Comparisons to *E. coli* DnaB-ssDNA Complexes**

1034 The RCSB PDB includes four unpublished entries corresponding to *E. coli* DnaB-
1035 ssDNA structures (PDB: 7T20, 7T21, 7T22, and 7T23 (16–19)). One structure
1036 was determined with the ATP analog AMP-PNP (7T20); the others harbor the
1037 ADP•AlF$_4$ transition state analog (7T21, 7T22, and 7T23). The ATP analog

1038 structure maps closely to the *Vc* structure, while the ADP•AlF_4 transition state
1039 DnaB structures map to the Bst complex. As such, conclusions made from
1040 comparisons between the *Vc* and Bst structures are fully compatible with the *E.*
1041 *coli* structures.

1042 **Supplementary Methods**

1043 **Expression Plasmid Construction**

1044 Genes corresponding to full-length *Vibrio cholerae* (*Vc*) DnaB and *Vc*DciA
1045 were amplified using polymerase chain reaction (PCR) and genomic DNA from
1046 *Vibrio cholerae* N16961 (ATCC # 39315D-5), and variously, cloned into the
1047 following protein expression vectors (pET24a, pCDFDuet-1, or pRSFDuet-1).
1048 These efforts encompassed untagged, amino, or carboxy-terminal hexahistidine-
1049 tagged proteins. Point mutations were introduced using the Quickchange Site
1050 Directed Mutagenesis kit (Agilent).

1051 *E. coli* DnaB was prepared as previously described of the *E. coli* DnaB•λP
1052 complex, except that λP was omitted (9).

1053 **Protein Expression**

1054 For production-scale bacterial growths, colonies corresponding to bacterial
1055 transformants were picked and resuspended in LB media supplemented with the
1056 appropriate antibiotic concentration. Bacterial cultures were grown at 37 °C to an
1057 OD600 ≈ 0.6 – 0.7 (RPM = 180). Protein expression was induced by making the
1058 culture 0.5 mM in isopropyl -D-1-thiogalactopyranoside (IPTG), followed by a
1059 temperature shift of the culture to 16 °C; protein production was allowed to
1060 continue for 14-16 hours (RPM = 180). Cells were recovered by centrifugation,
1061 resuspended in 20mM Tris-HCl pH 7.4, 500mM NaCl, 5mM $MgCl_2$, 10% sucrose,

1062 5mM β-mercaptoethanol at a ratio of 5 mL buffer per gram of wet cells, and frozen
1063 at -80°C.

1064 ***Vc*DnaB.** *Vc*DnaB-untagged (pNG066, 50 µg/mL kanamycin), *Vc*DnaB-NHis
1065 (pNG067, 50 µg/mL kanamycin), *Vc*DnaB-E259A-NHis (pNG072, 50 µg/mL
1066 kanamycin), *Vc*DnaB-NTD-untagged (pNG114, 50 µg/ml kanamycin), *Vc*DnaB-
1067 NTD_LH-untagged (pNG131, 50 µg/mL kanamycin) and *Vc*DnaB-LH_CTD-
1068 untagged (pNG134, 50 µg/mL kanamycin) were expressed using the above
1069 procedure.

1070 ***Vc*DciA.** *Vc*DciA-FL-CHis (pNG057, 50 µg/ml streptomycin) and *Vc*DciA-CTD-
1071 CHis (pNG087, 50 µg/ml streptomycin) were expressed using the procedure
1072 above, except for three changes: a) the media was LB for pNG057 and SB (20,
1073 21): for pNG087, b). after adding 0.5 mM IPTG to the culture, protein expression
1074 was allowed to continue for 3 hours at 37 °C, and c) cells were resuspended after
1075 harvesting in 20 mM Tris-HCl pH 8, 300 mM NaCl, 5% glycerol, 5 mM β-
1076 mercapoethanol.

1077 *Vc*DciA-NTD-Chis (pNG078, 50 µg/ml streptomycin) was grown using the
1078 same procedure as full-length DciA, except that cells were resuspended in 20 mM
1079 Tris-HCl pH 8, 300 mM NaCl, 5% glycerol, and 5 mM β-mercapoethanol.

1080 ***Vc*DnaB-*Vc*DciA coexpression.** *Vc*DnaB-untagged (pNG066, streptomycin: 50
1081 ug/mL) and *Vc*DciA-FL-Chis (pNG057, Kanamycin: 50 ug/mL) were co-expressed
1082 using the above procedure altered to account for the co-expression.

1083 **Protein Biochemistry**

1084 Unless otherwise indicated, standard protein biochemistry techniques were
1085 used to purify all the proteins in this study (Supplementary Figure 8). All
1086 manipulations were carried out at 4 °C.

1087 Unless otherwise indicated, 90 - 160 mL of cells expressing the protein of
1088 interest were lysed using a Sonic dismembrator (Model 500, Fisher Scientific) at
1089 the following settings: 3 min at 70% amplitude, with alternating 30s on and off
1090 cycles and 15 min at 50% amplitude. The protein of interest was recovered in the
1091 soluble fraction by centrifugation (RPM=16,000, JA-17, Beckman-Coulter).

1092 ***Vc*DnaB.** Untagged *Vc*DnaB was purified by combining ammonium sulfate (AS)
1093 precipitation and heparin, hydroxyapatite, and size exclusion chromatography.
1094 *Vc*DnaB was found in the supernatant after making the soluble fraction 20% of
1095 saturated AS (SAS), but in the pellet when treated with 45% SAS. The 45% SAS
1096 pellet was resuspended in heparin buffer A below and purified over a 50 mL
1097 Heparin Sepharose Fast Flow (Cytiva), with the following buffers: heparin buffer A:
1098 20 mM Tris-HCl, pH = 7.4, 5 mM $MgCl_2$, 5% glycerol, 5 mM β-mercaptoethanol;
1099 Heparin buffer B: A + 1 M NaCl and a linear gradient from 0% to 40% B. Heparin-
1100 purified *Vc*DnaB was purified by hydroxyapatite chromatography (65 ml, CHT, Bio-
1101 Rad) in the following buffers: A: 5mM potassium phosphate, pH = 7.5, 100 mM
1102 NaCl, 5 mM $MgCl_2$, 5% glycerol, 5 mM β-mercaptoethanol; B: A + 250 mM
1103 potassium phosphate, pH = 7.5). CHT-purified *Vc*DnaB was concentrated by 45%
1104 AS precipitation, redissolved in 6 mL of 20 mM potassium HEPES, pH=7.5, 500
1105 mM NaCl, 5 mM $MgCl_2$, 5% glycerol, 5 mM β-mercaptoethanol), and applied to a
1106 320 mL Superdex200 Prep Grade (Cytiva) column equilibrated in the above buffer.

1107 Size exclusion chromatography fractions free of nuclease activity were pooled,
1108 concentrated (Corning, 20 ml, 10 kDa molecular weight cutoff) to 55 mg/ml,
1109 aliquoted (~10-20 µl aliquots), flash frozen in liquid nitrogen, and maintained at -
1110 80 °C until use.

1111 *Vc*DnaB-NHis and *Vc*DnaB-E259A-NHis were purified using the protocol
1112 employed with untagged *Vc*DnaB but with discrete changes. The 45% SAS pellet
1113 was resuspended in Ni^{2+}-nitrilotriacetic acid (NiNTA) Buffer A (20 mM Tris-HCl, pH
1114 = 7.4, 50 mM NaCl, 5 mM $MgCl_2$, 5% glycerol, 5 mM β-mercaptoethanol) and
1115 incubated with 15 mL of NiNTA agarose beads (Qiagen) according to the
1116 manufacturer's instructions. The beads were washed with 180 mL of NiNTA Buffer
1117 B (20 mM Tris-HCl, pH=7.4, 50 mM NaCl, 5 mM $MgCl_2$, 5% glycerol, 5 mM β-
1118 mercaptoethanol, 30 mM imidazole pH 8); *Vc*DnaB-NHis and was eluted from the
1119 beads with 300 mL of NiNTA Buffer C (20 mM Tris-HCl pH=7.4, 50 mM NaCl, 5
1120 mM $MgCl_2$, 5% glycerol, 5 mM β-mercaptoethanol, 250 mM imidazole, pH = 8).
1121 NiNTA-purified *Vc*DnaB-NHis was further purified over Heparin Sepharose Fast
1122 Flow as was done with untagged DnaB, except that the elution gradient was
1123 modified; 4 column volumes of Heparin buffer A (above), followed by a linear
1124 gradient from 5% to 100% Heparin buffer B over six column volumes. *Vc*DnaB-
1125 NHis fractions were recovered and pooled in the ~80 mM to ~600 mM NaCl
1126 positions on the gradient. The heparin pool was passed through a 23 mL SP
1127 Sepharose Fast Flow (Cytiva) equilibrated in Q buffer A: 20 mM Tris-HCl, pH=7.4,
1128 100 mM NaCl, 5 mM $MgCl_2$, 5% glycerol, and 5 mM β-mercaptoethanol; *Vc*DnaB-
1129 NHis was captured by a 50mL Q Sepharose Fast Flow column (Cytiva) attached

1130 in-line. After a 4-column volume wash with 10% Q buffer B: (20 mM Tris-HCl, pH
1131 = 7.4, 1 M NaCl, 5 mM $MgCl_2$, 5% glycerol, and 5 mM β-mercaptoethanol), a linear
1132 gradient from 10% to 100% Q buffer B was used to elute *Vc*DnaB-NHis, which was
1133 recovered in the ~250 mM to ~800 mM NaCl positions on the gradient. The pooled
1134 *Vc*DnaB-NHis containing fractions were further purified over hydroxyapatite (Bio-
1135 Rad, CHT) and Superdex200 Prep grade (Cytiva) as described above. Size
1136 exclusion chromatography fractions were pooled, concentrated as described
1137 above, to 40 mg/ml, aliquoted (~15-30 µL aliquots), flash frozen in liquid nitrogen,
1138 and maintained at -80 °C until use.

1139 ***Vc*DciA.** *Vc*DciA-FL-CHis, *Vc*DciA-NTD-CHis, and *Vc*DciA-CTD-CHis were
1140 purified using nearly identical protocols. Cells were lysed as above, except that
1141 Protease Inhibitor Mini Tablet, EDTA-free (Pierce, ThermoFisher Scientific p/n
1142 32955), was added to the *Vc*DciA-CTD-CHis sample at a ratio of one tablet for
1143 every 10 mL of lysate. All three *Vc*DciA constructs were recovered in the soluble
1144 fraction. Each fraction was applied to ~10 mL of Ni-NTA agarose beads, incubated
1145 for 40 min, and washed with 80 mL of NiNTA Buffer A (20 mM Tris-HCl, pH = 8,
1146 300 mM NaCl, 5% glycerol, and 5 mM β-mercaptoethanol), supplemented with 15
1147 mM imidazole, pH = 8 (*Vc*DciA-NTD-CHis), or 30 mM imidazole, pH = 8 (*Vc*DciA-
1148 FL-CHis and *Vc*DciA-CTD-CHis). *Vc*DciA constructs were eluted from the beads
1149 with NiNTA Buffer B (20 mM Tris-HCl, pH = 7.4, 50 mM NaCl, 5 mM $MgCl_2$, 5%
1150 glycerol, 5 mM β-mercaptoethanol, and 250 mM imidazole, pH = 8). Further
1151 purification was achieved by flowing the various *Vc*DciA constructs through a 50mL
1152 Q Sepharose Fast Flow column for capture on a 23mL SP Sepharose Fast Flow

1153 column attached in-line; both columns had been equilibrated in SP buffer A: (20mM
1154 Tris-HCl, pH = 7.4, 50 mM NaCl, 5% glycerol, and 5 mM β-mercapoethanol). After
1155 separating the two columns, weakly bound proteins were washed away with 4
1156 columns volumes of 5% SP buffer B (20 mM Tris-HCl, pH = 7.4, 1 M NaCl, 5%
1157 glycerol, and 5 mM β-mercaptoethanol); this was followed by a linear gradient from
1158 5% to 100% SP buffer B over 3 column volumes. Notably, we observed that
1159 *Vc*DciA-FL-CHis eluted at the ~150 mM to ~350 mM NaCl position in the gradient,
1160 *Vc*DciA-NTD-CHis between ~120 mM and ~700 mM NaCl, and *Vc*DciA-CTD-CHis
1161 between ~180 mM and ~300 mM NaCl. Pooled fractions were concentrated
1162 (*Vc*DciA-FL-CHis by 50% AS precipitation, *Vc*DciA-NTD-CHis by 70% AS
1163 precipitation, and *Vc*DciA-CTD-CHis using a 15 mL (2 kDa molecular weight cutoff)
1164 spin concentrator (Sartorius Vivaspin). Each construct was then chromatographed
1165 over a 320 mL Superdex200 Prep Grade column, equilibrated in 20 mM
1166 potassium-HEPES, pH = 7.5, 300 mM NaCl, 5% glycerol, and 5 mM β-
1167 mercaptoethanol, and processed for -80° storage as described above.

1168 **Coexpressed *Vc*DnaB-*Vc*DciA.** A soluble fraction derived from coexpressed
1169 *Vc*DnaB-untagged - *Vc*DciA-FL-Chis, prepared as described above, was
1170 submitted to NiNTA and size exclusion chromatography (320 mL Superdex200
1171 Prep Grade). The NiNTA chromatography was performed as above with the
1172 following buffers: NiNTA buffer A (20 mM Tris-HCl, pH = 7.4, 500 mM NaCl, 5 mM
1173 $MgCl_2$, 5% glycerol, 5 mM β-mercaptoethanol, and 30 mM imidazole, pH = 8) and
1174 NiNTA buffer B (20 mM Tris-HCl, pH = 7.4, 500 mM NaCl, 5 mM $MgCl_2$, 5%
1175 glycerol, 5 mM β-mercaptoethanol, and 250 mM imidazole, pH = 8). NiNTA-

1176 purified protein was concentrated by precipitation with 75% SAS and redissolved
1177 in 6 mL of the running buffer (below) for size exclusion chromatography. The size
1178 exclusion chromatography was carried out in (20 mM potassium HEPES, pH = 7.5,
1179 500 mM NaCl, 5 mM $MgCl_2$, 5% glycerol, and 5 mM β-mercaptoethanol).

1180 **NiNTA pull-downs**

1181 Equal volumes (22.5 mL) of cells at similar densities expressing untagged
1182 *Vc*DnaB (full-length, NTD, NTD-LH, or LH-CTD, each in 20 mM Tris-HCl pH 7.4,
1183 500 mM NaCl, 5 mM $MgCl_2$, 10% sucrose, 5 mM β-mercaptoethanol) and his-
1184 tagged *Vc*DciA (full-length, Lasso, or KH, each in 20 mM Tris-HCl pH 8, 300 mM
1185 NaCl, 5% glycerol, 5 mM β-mercapoethanol), were mixed, diluted with 15 mL of
1186 buffer (20mM Tris-HCl pH 8, 300mM NaCl, 5% glycerol 5 mM β-mercapoethanol)
1187 were combined to a total volume of 60 mL. The mixture was lysed using a Sonic
1188 dismembrator (Model 500, Fisher Scientific) at the following settings: 2 min at 70%
1189 amplitude, with alternating 30s on and off cycles. Sonication settings were: 30s
1190 on, 30s off, 2 min total on time, 70% amplitude. The lysate was centrifuged at 16k
1191 RPM in a JA-17 rotor (Beckman-Coulter), and the supernatant was recovered.

1192 The clarified lysate was incubated with Ni-NTA Agarose beads for 40
1193 minutes, washed with 90 mL of NiNTA Buffer A (20 mM Tris-HCl pH 8, 300 mM
1194 NaCl, 5% glycerol, 5 mM β-mercaptoethanol, 15 mM Imidazole pH 8). Protein was
1195 eluted using 30 mL of NiNTA Buffer B (20 mM Tris-HCl pH 8, 300 mM NaCl, 5%
1196 glycerol, 5 mM β-mercaptoethanol, 250 mM Imidazole pH 8).

1197 **ATPase Rate Measurements**

1198 An NADH-coupled microplate spectrophotometric assay was used to
1199 measure rates of ATP hydrolysis (22, 23) by *Vc*DnaB and how rates are affected

1200 by the presence of our suite of full-length and truncated constructs of *Vc*DciA. In
1201 all experiments, *Vc*DnaB was kept fixed at 200 nM, while titrations of DciA
1202 encompassed concentrations between 0 nM and 6400 nM.

1203 NADH oxidation data were recorded in the presence of 2 mM ATP (Gold
1204 Biotechnology, Inc. p/n: A-081-1), 2 mM phosphoenolpyruvic acid monopotassium
1205 salt (PEP), 0.01 U/μL lactate dehydrogenase (Sigma-Aldrich, L1254), 0.002 U/μL
1206 pyruvate kinase (Sigma-Aldrich, p/n: P7768,) and 0.3 mM NADH in the following
1207 buffer: 50 mM potassium-HEPES – pH=7.5, 150 mM potassium acetate, and 8 mM
1208 magnesium acetate, 5 mM β-mercaptoethanol, and 0.25 mg/mL bovine serum
1209 albumin (Sigma-Aldrich p/n: A3912). The above components were combined,
1210 save for ATP, into wells of a Corning 96-well Clear Flat Bottom UV-Transparent
1211 Microplate (p/n: 3635), and the plate was warmed to 37 °C for 5 minutes. After the
1212 quick addition of 2 mM ATP, the plate was inserted into a SpectraMax M5 plate
1213 reader (Molecular Devices), and absorbance data were taken at 340 nm every 30
1214 s over 30 min. Raw data were exported in text format and imported into Microsoft
1215 Excel for analysis. Each absorbance curve was manually inspected to identify 10
1216 minutes during the experiment wherein the slope of the 340 nm absorbance vs
1217 time was constant. The values in the above period were divided by the (-) 6.22
1218 mM^{-1} cm^{-1} extinction coefficient of NADH and the path length in cm calculated by
1219 the plate reader to result in the rate of ATP hydrolysis in mM/s; further division by
1220 the mg of DnaB in the assay provided the specific activity in mM/s/mg.

1221 **Grid Preparation for Single Particle Cryo-EM**

1222 To prepare complexes for cryo-EM, untagged *Vc*DnaB-FL and *Vc*DciA-FL-
1223 CHis were diluted in 20 mM HEPES pH = 7.5, 200 mM NaCl, 5 mM MgCl2, 5 mM

1224 β-mercaptoethanol, and 5 mM ATPγS to reach a final concentration of 18 μM
1225 (DnaB monomer) and 12.7 μM (DciA). A ssDNA oligonucleotide bearing the origin
1226 of the replication sequence of *Vibrio cholerae* serotype O1 (Supplementary Table
1227 4, oligo: O1b-*Vc*F) was added at a concentration of 5.4 μM. 3 μL of the *Vc*DnaB-
1228 DciA-ssDNA sample was applied to a Quantifoil UltrAuFoil R1.2/1.3 Au300 grid,
1229 previously plasma cleaned with a 3:1 ratio of Ar/O_2 at 15 W for 10 seconds in a
1230 Gatan Solarus II glow discharger. Liquid absorption was allowed for 30 seconds
1231 at 4 °C and 100% humidity. The sample was then blotted for 4 seconds with a blot
1232 force of 4 and plunge-frozen into liquid ethane. The procedure was conducted on
1233 a Vitrobot Mark IV (Thermo Fisher). The grid was stored in liquid nitrogen until
1234 data collection.

1235 **Cryo-EM Data Acquisition**

1236 Cryo-EM images were acquired on a Titan Krios (ThermoFisher) operating
1237 at 300 keV and fitted with a Gatan K3 direct electron detector. 12,265 movies were
1238 collected using Leginon (24, 25) at an 81,000 magnification, corresponding to a
1239 pixel size of 0.541 Å/pixel, and at a defocus of -1.57 μm. The total exposure dose
1240 was 51.37 e–/$Å^2$, and the exposure time per movie was 2 seconds. Additionally,
1241 20° and 40° tilted images were collected to mitigate the expected preferred particle
1242 orientation that would otherwise compromise the EM reconstruction.

1243 **Cryo-EM Image Processing**

1244 The 12,265 images measured from the *Vc*DnaB-DciA-ssDNA-ATPγS
1245 complex were processed using two approaches (Supplementary Figure 3): a)
1246 template-based picking using a prior DnaB structure (PDB entry = 7T20 (17)) as
1247 the initial template, and b) blob-picking. For facile computing, the blob-picking

1248 approach initially targeted 10% of the images, which produced 2.5 million particles
1249 that were 2D classified and submitted to *ab initio* reconstruction with C1 symmetry
1250 enforced. This reconstruction generated two volumes, C0 and C1 (~123K and
1251 ~151K particles), which were judged to be of low quality and influenced our
1252 decision not to pursue the blob-picking approach further.

1253 For the PDB structure-based template-picking approach, for computational
1254 ease, we selected 100 frames at random, binned them by a factor of ½, and
1255 submitted them for motion correction and Contrast Transfer Function (CTF)
1256 estimation as implemented in cryoSPARC (26–32). Unless otherwise indicated,
1257 the following steps were performed within cryoSPARC. An EM map was
1258 calculated from PDB entry 7T20 in EMAN2 (33) and used to derive templates for
1259 application to the above 100 images; this procedure netted 92,178 particles. From
1260 this collection, 79,820 particles were extracted using a box size of 360 pixels and
1261 2D classification. Subsequently, *ab initio* reconstruction was performed with C1
1262 symmetry, which produced two classes (A0, A1). Class A0 (18.5K particles) was
1263 carried forward to homogeneous refinement, which created an 8.72 Å map (B0).
1264 Inspection of Class A1 suggested a lower quality than A0. As such, further
1265 processing of Class A1 was not pursued.

1266 The complete data set (12,265 images) was then submitted to motion
1267 correction (Fourier crop factor of ½) and CTF estimation using standard settings.
1268 These calculations enabled manual curation leveraging ice thickness (0.82-1.1)
1269 and CTF fit resolution (2.17-9.98) parameters to eliminate images with low overall
1270 resolution. The resulting 11,817 images were submitted to template-based picking

1271 using the B0 map; this calculation produced ~4.3 million particles. These particles
1272 were extracted as above and submitted to 2D classification and *ab initio*
1273 reconstruction using C1 symmetry. The resulting volumes, D0 and D1 (~437K and
1274 ~291K particles), were submitted to heterogeneous refinement and produced two
1275 volumes, E0 and E1 (~526K and ~202K particles). Inspection of these two
1276 volumes implied that the 6.24 Å E0 volume was of higher quality.

1277 Particles from the E0 Class were re-extracted using a box size of 360 pixels,
1278 with no Fourier crop, and submitted to non-uniform refinement, which yielded an
1279 EM map with a resolution of 3.36 Å (Volume F). To further improve the quality of
1280 our reconstruction, volume F particles were submitted to global CTF refinement.
1281 The final non-uniform refinement job produced map G at 3.37 Å, which was further
1282 sharpened with DeepEMhancer (34) to produce volume H; this volume embodied
1283 our best map and was used for model building (below). EM density was evident
1284 for the protein, nucleic acid, and nucleotides. Indeed, estimates of the local
1285 resolution ranged from 2.8 Å to 4.8 Å, with the highest resolution density spanning
1286 the DnaB-CTDs (Supplementary Figure 4C). The quality of the protein density
1287 was sufficient to allow unambiguous assignment of side chains to the map.
1288 However, no density could be assigned to the DciA loader.

1289 Next, we made several efforts to improve the resolution of Map H in hopes
1290 of locating the DciA loader. 3D classification of the particles that generated Map
1291 F produced ten classes (group I). Classes I1 and I9 retained the highest number
1292 of particles, 82K and 77K, respectively, and showed high similarity to Map H, but
1293 with no features that could be assigned to *Vc*DciA. Non-uniform refinement was

1294 performed on volumes I4 (46K particles) and I6 (59K particles), producing maps at
1295 the resolution of 3.76 Å (class J4) and 3.78 Å (class J6). Automatic model building
1296 with ModelAngelo (35) on the sharpened map, once again, failed to show any
1297 evidence of *Vc*DciA. Homogeneous refinement of the particles that produced the
1298 E0 volume created class L, followed by two consecutive rounds of non-uniform
1299 refinements (classes M and N) with different settings, using volume E0 as the input
1300 map. This procedure generated Map N, followed by Map O after DeepEMhancer
1301 sharpening, with both at resolutions of 3.45 Å. Neither map showed evidence of
1302 density better than Map H, let alone proof of the presence of *Vc*DciA. Lastly,
1303 inspection of the 3D variability analysis of the particles that produced volume F
1304 (group K) produced no evidence of conformational changes in the *Vc*DnaB-ssDNA
1305 complex.
1306

1307 ## Supplementary Figures

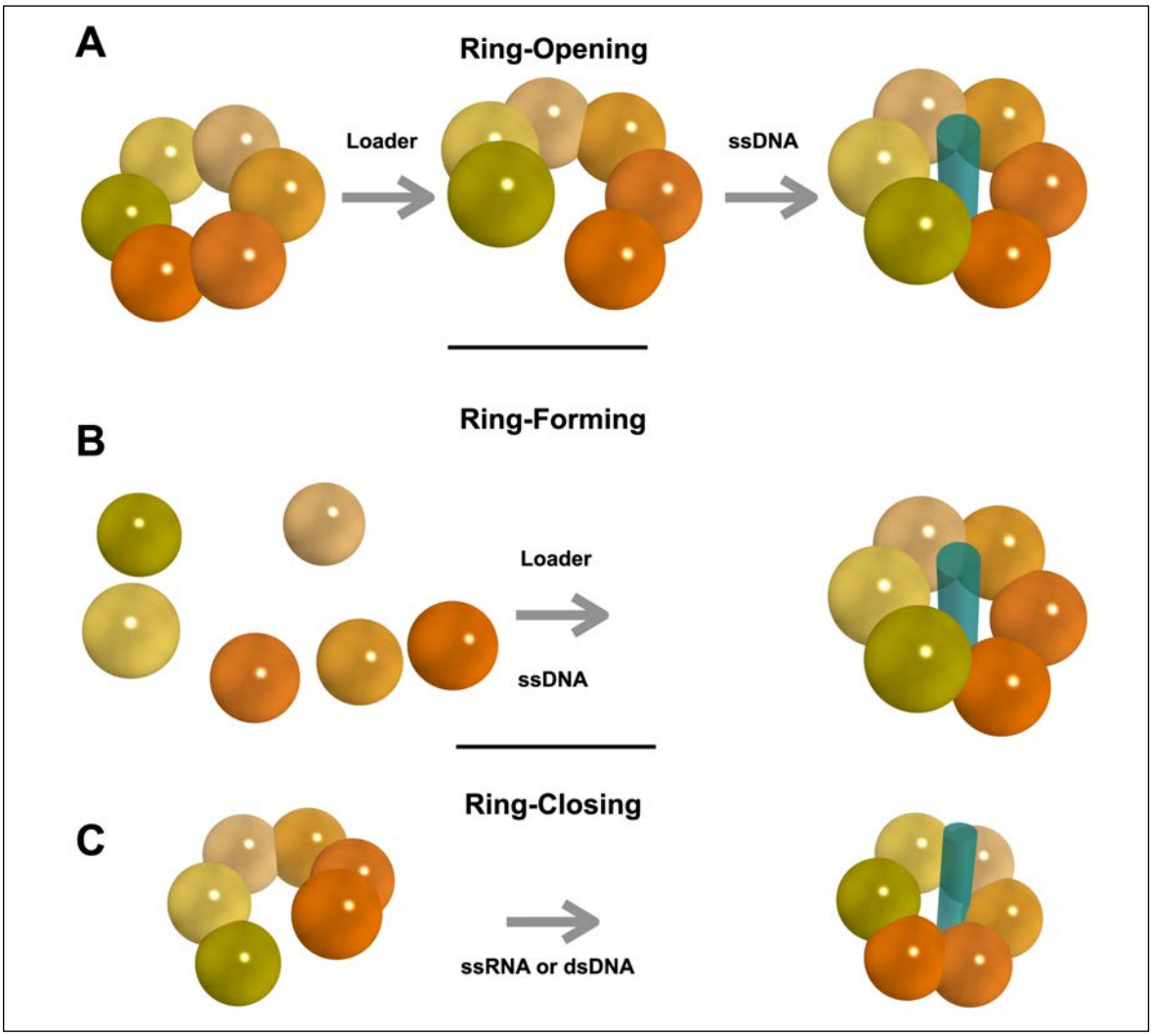

1308 **Supplementary Figure 1. Mechanisms of Helicase Loading.** Strategies used
1309 to load hexameric helicases onto nucleic acid substrates are ring-opening, ring-
1310 forming, and ring-closing (1–3); the terms refer to the initial state of the helicase.
1311 In the ring-opening scheme, closed-ring hexamers are opened by helicase loaders
1312 and subsequently assembled on ssDNA. The hexameric helicase is assembled
1313 on ssDNA from monomers using a ring-forming mechanism. Entry of the nucleic
1314 acid substrate and other factors mediate the ring-closing scheme. Hexameric
1315 helicase subunits are represented as spheres in shades of orange. For clarity,

1316 only the ATPase domains are shown. Nucleic acid substrates are depicted as
1317 deep teal cylinders.

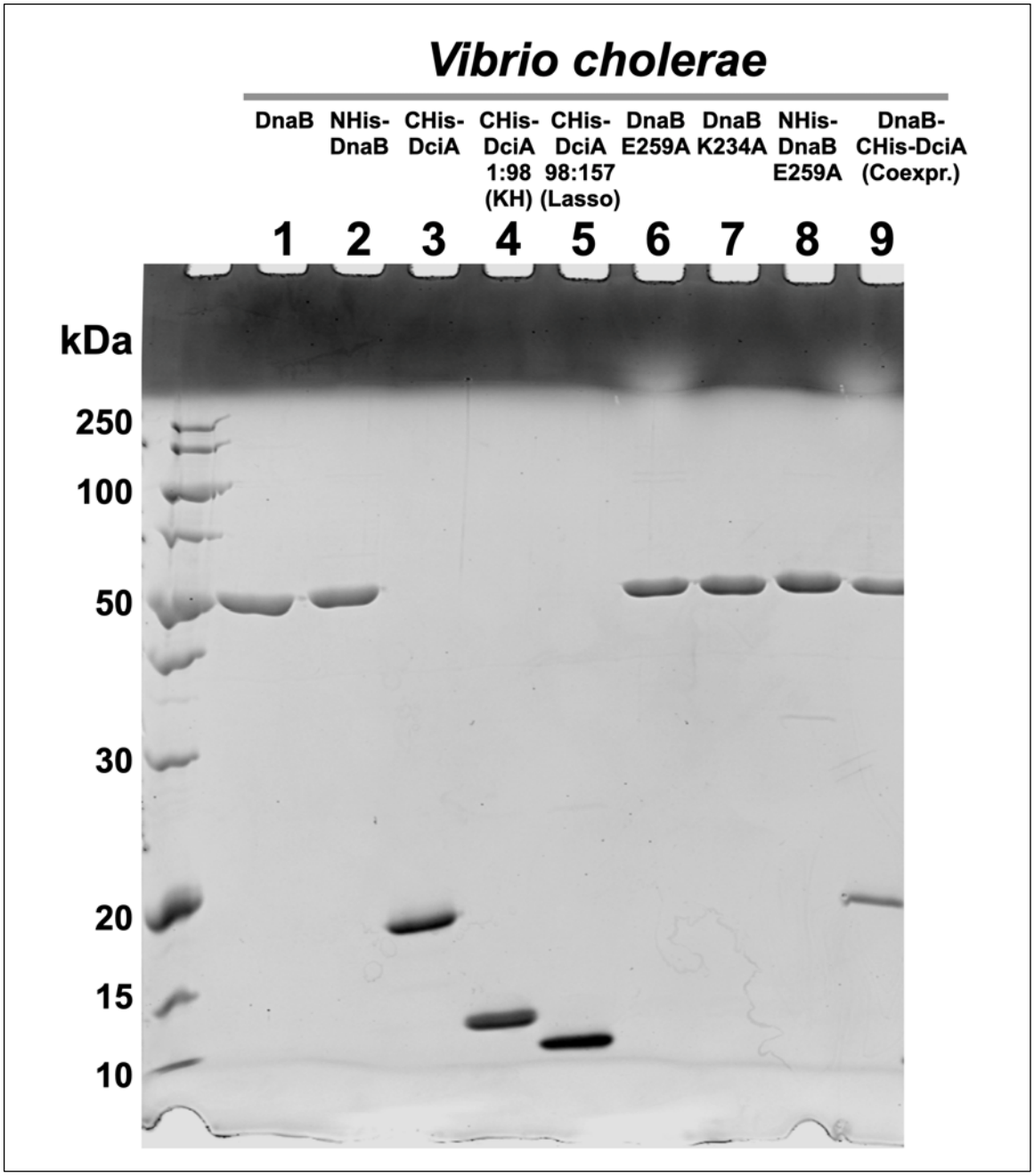

Supplementary Figure 2. Purified *Vc*DnaB and *Vc*DciA proteins. A) 15% SDS-Gel electrophoretic analysis of purified *Vc* proteins. Lane 1: *Vc*DnaB untagged; Lane 2: N-terminal His-tagged *Vc*DnaB; Lane 3: C-terminal His-tagged *Vc*DciA full-length; Lane 4: C-terminal His-tagged *Vc*DciA KH domain (residues 1:98); Lane 5: C-terminal His-tagged *Vc*DciA Lasso domain (residues 98:157); Lane 6: Untagged *Vc*DnaB-E259A; Lane 7: Untagged *Vc*DnaB-K234A; Lane 8: N-

terminal His-tagged *Vc*DnaB-E259A; Lane 9: Coexpressed *Vc*DnaB untagged + C-terminal His-tagged Full-length *Vc*DciA.

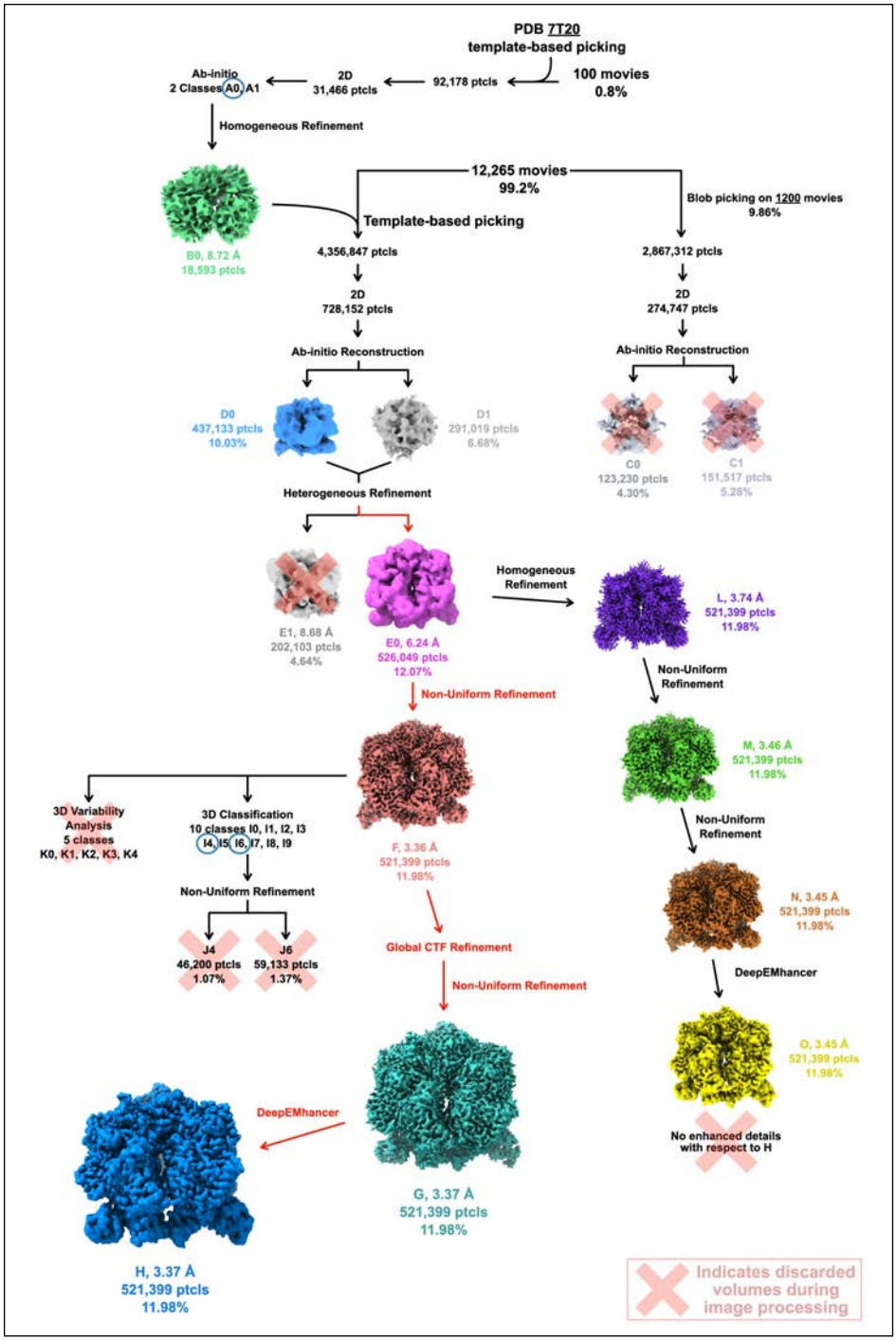

1327 **Supplementary Figure 3. Workflow in the Processing of cryo-EM Data for the**
1328 ***Vc*DnaB-ssDNA-ATPγS complex.** The steps in this workflow are described in
1329 the Methods section. The percentages reported alongside the volumes are
1330 calculated against the number of starting picked particles. The various

volumes/maps in the workflow are depicted with unique colors. Map H represents the highest quality map we obtained, against which the atomic model was built and refined. The extended length of ssDNA was built into map E0.

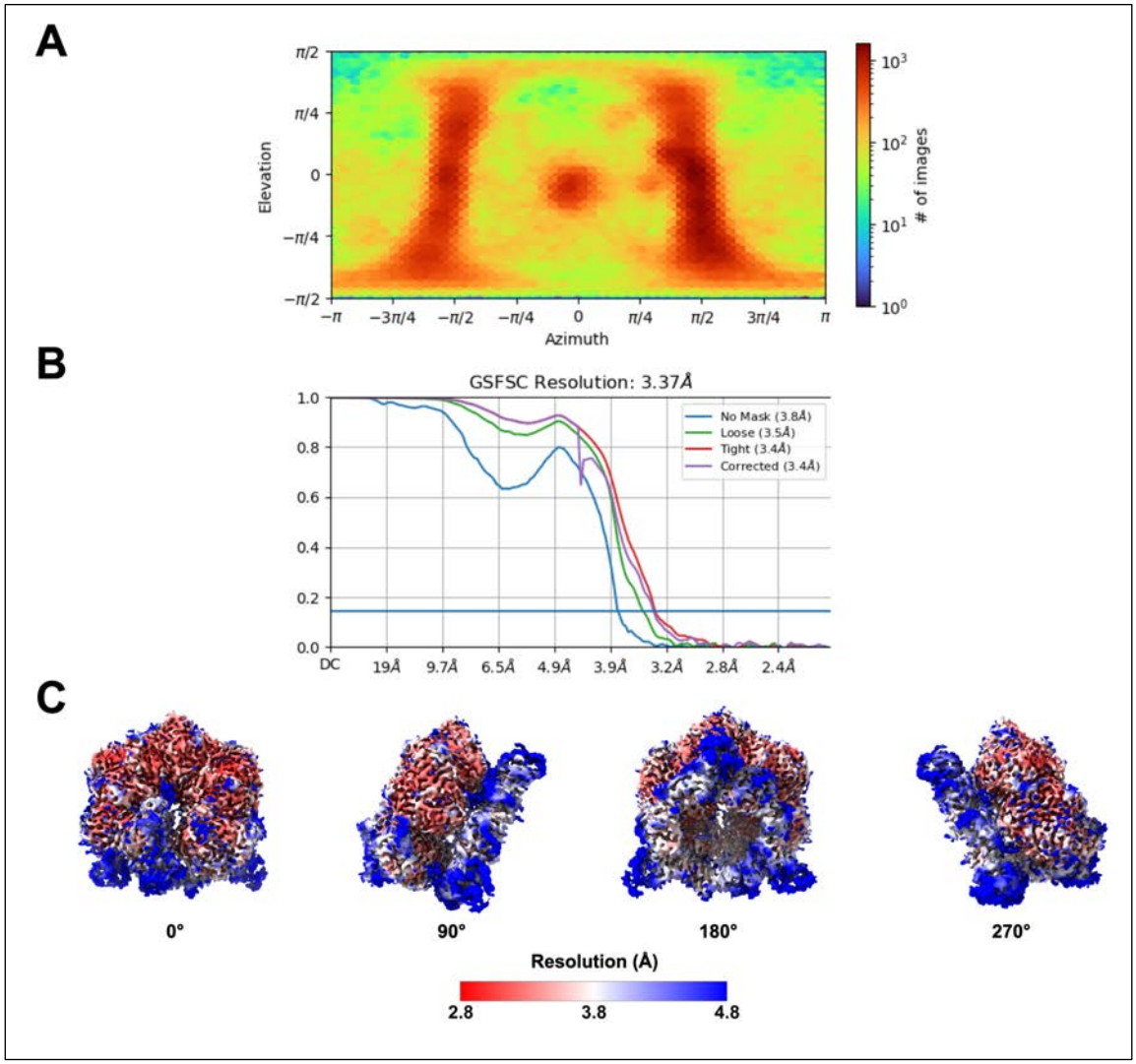

1335 **Supplementary Figure 4. Statistics, Fourier Shell Correlation, and Local**
1336 **Resolution.** A) CryoSPARC plot of particles' azimuthal and elevation angles in the
1337 3.37 Å reconstruction of *Vc*DnaB-ssDNA-ATPγS. The blue-to-red scale
1338 represents the number of particles, ranging from 10^2 to 10^3. The red clusters
1339 represent the preferred orientation of the particles in our data set; however, this
1340 distribution of particles did not impact the quality of the map reconstruction. B)
1341 Fourier Shell Correlation (FSC) plots taken from the non-uniform refinement
1342 calculation that produced the map H. Plots were generated by applying no mask,

1343 spherical mask, loose mask, tight mask, and corrected mask on the protein-DNA
1344 complex. The corrected tight mask plot shows a resolution of 3.37 Å at an FSC
1345 value of 0.143. C) The *Vc*DnaB + ssDNA EM density map is colored (red: 2.8 Å
1346 to blue: 4.8 Å) according to the local resolution. The density map is depicted in
1347 four poses that differ by 90° rotations along the Y axis.
1348

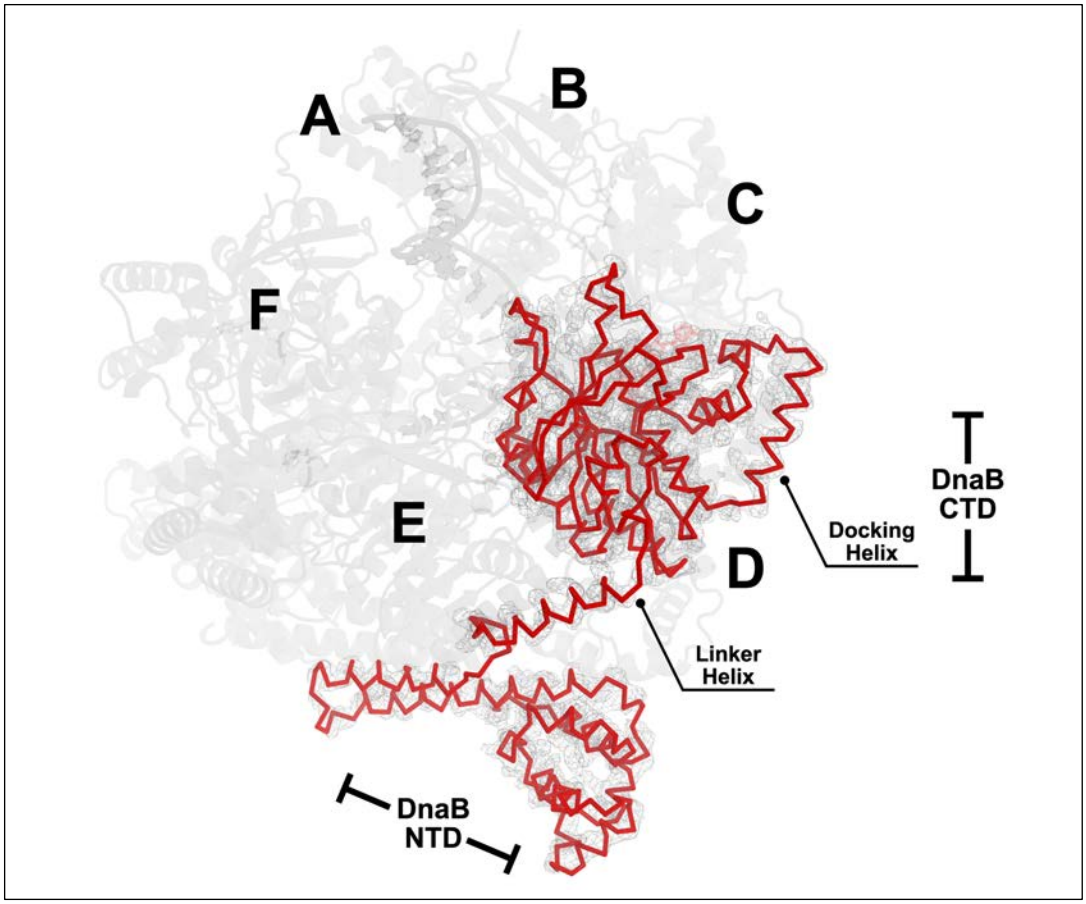

1349
1350 **Supplementary Figure 5. Cryo-EM Density Corresponding to one *Vc*DnaB**
1351 **chain.** EM density is drawn as a grey mesh around chain D of the *Vc*DnaB-
1352 ssDNA-ATPγS structure. The density is drawn in PyMol using the following
1353 parameters: isomesh level: 10 and isomesh carve: 2.3. The *Vc*DnaB chain B
1354 ribbon model is superimposed on the EM density. The rest of the hexameric
1355 *Vc*DnaB-ssDNA-ATPγS structure is drawn in the cartoon format to provide context.
1356 Labels identify DnaB sub-domains and chains.

1357

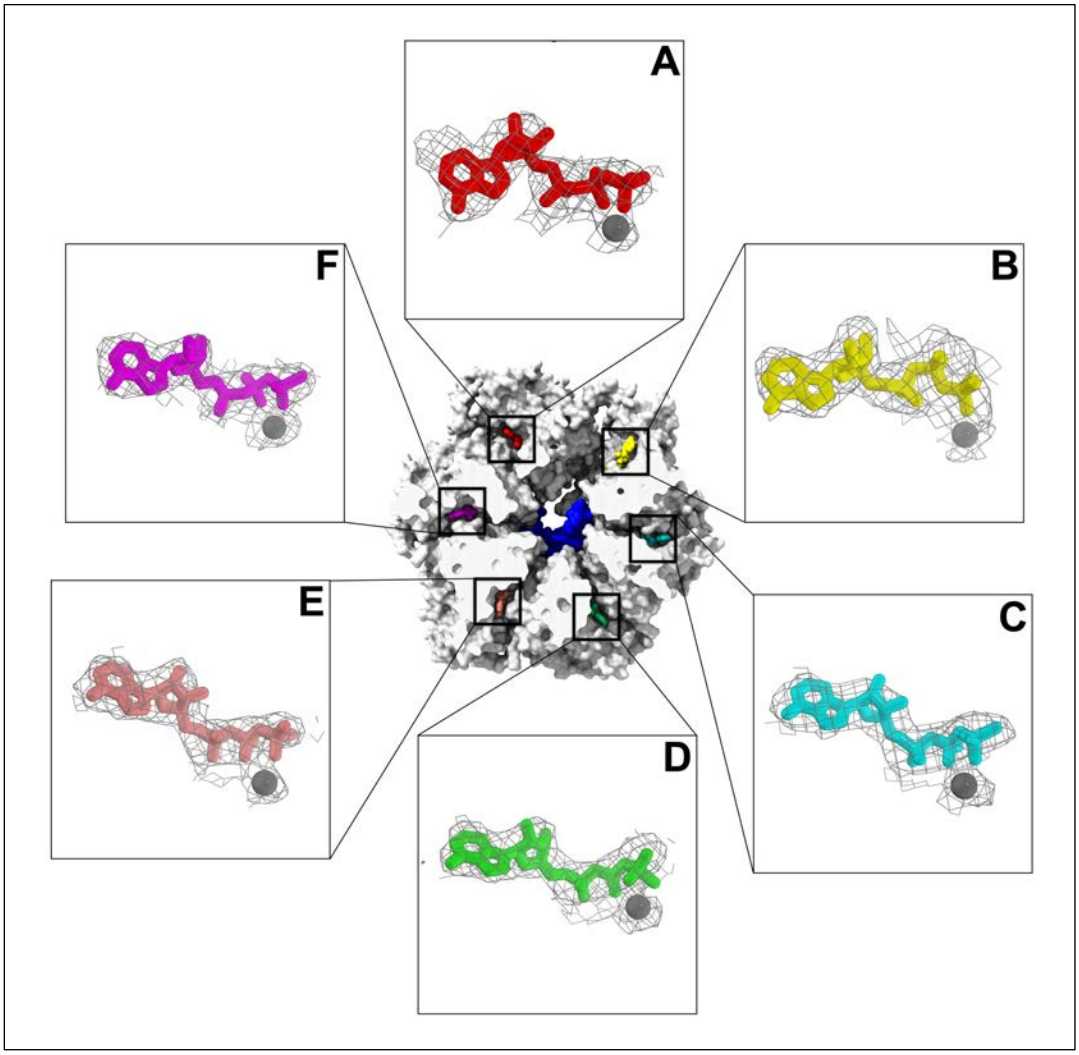

1358 **Supplementary Figure 6. The six nucleotide binding pockets in the *Vc*DnaB-**
1359 **ssDNA structure are filled with ATPγS•Mg^2.** The β and γ phosphates of each
1360 ATPγS moiety are coordinated to a Mg^{2+} atom. EM density is drawn as a mesh
1361 around each nucleotide. The density is drawn in PyMol using the following
1362 parameters: isomesh level chain B: 2; chains A-C-D-E-F: 2, and isomesh carve:
1363 chains A-B-C-D-E-F: 5. The ATPγS molecules, each colored uniquely, are drawn
1364 in the stick representation, with the Mg^{2+} ion depicted as a grey sphere. The
1365 position of the nucleotide pockets is indicated on the surface representation of

*Vc*DnaB, sliced to expose the six pockets. ssDNA within DnaB is colored dark blue.

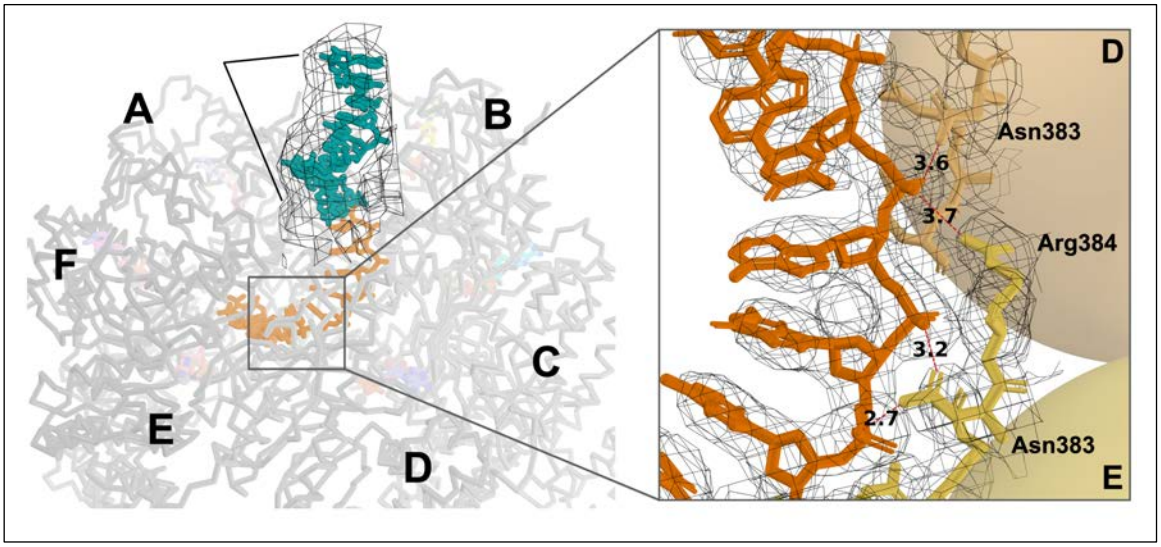

Supplementary Figure 7. 11 additional ssDNA positions outside the confines of *Vc*DnaB are seen in the cryo-EM density map. Close inspection of the 6.24 Å map E0 (Supplementary Methods and Supplementary Figure 3) enabled an ssDNA model to be constructed that was 11 positions longer than that seen in map H. The map into which this segment was built is shown as a mesh (isomesh level: 2.5). The extra positions are colored in teal; the ssDNA built into map H is colored orange. *Vc*DnaB is represented as a grey ribbon, and each monomer is labeled by chain (A-B-C-D-E-F). For reference, the six ATPγS and six Mg^{2+} atoms are displayed as sticks and spheres, respectively, with transparency applied. As noted in the methods, neither map H nor map E0 was sufficiently resolved to permit the assignment of parts of the input 60-mer sequence to the map. As such, the sequence in our final model was built as follows: TCCAGATACACAAAAAAAAAAA. Inset: close-up view of the DnaB-ssDNA interface superimposed on the cryo-EM density. The inset was rotated ~90° counterclockwise with respect to the main panel and adjusted to align the nucleobases along the vertical axis.

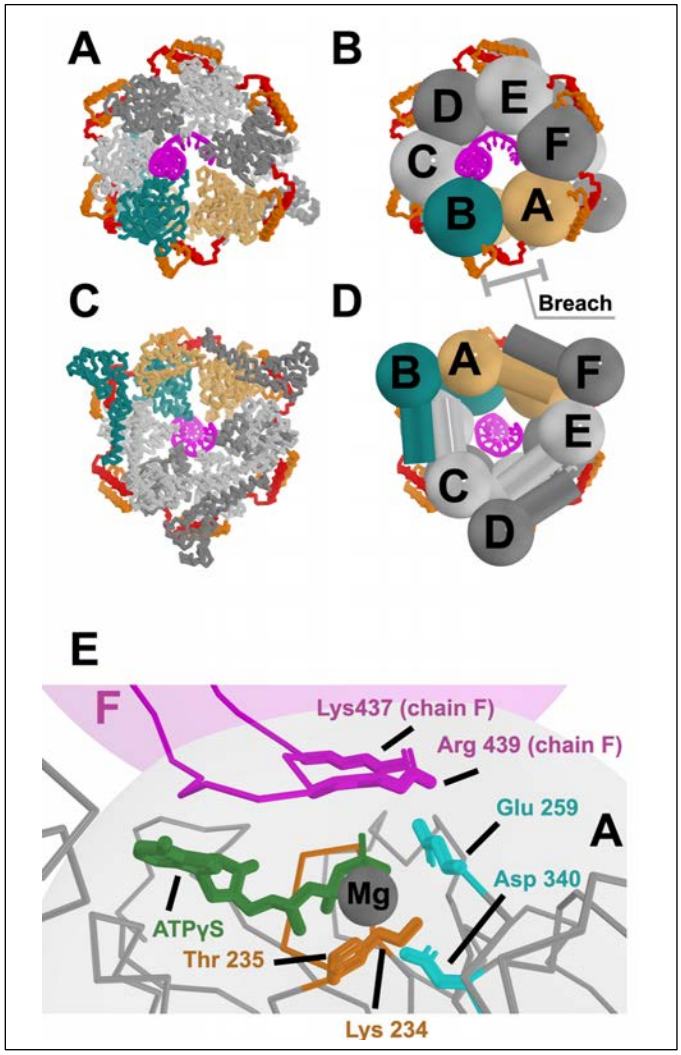

Supplementary Figure 8. The *Vc*DnaB-ssDNA-ATPγS Complex. The *Vc*DnaB-ssDNA-ATPγS is drawn in a ribbon representation (A or B) or a schematic using a design language wherein the NTDs are depicted as a mushroom shape and the CTDs as spheres (B or D). ssDNA, colored in magenta, is displayed in a cartoon and stick representation. The breach in the CTD layer is between chain A (light orange) and chain B (deep teal); other DnaB subunits are colored in alternating shades of gray. The Docking Helix (DH) and the Linker Helix (LH) are depicted as transparent cylinders colored orange and red, respectively. The pose in panels A and B is along the path of DNA. Panels C and D are in a pose that is rotated

1394 approximately 180° from that in panels A and B. E) Closeup of the composite
1395 nucleotide catalytic center in *Vc*DnaB at the interface between subunits A (gray
1396 shape) and F (magenta shape). ATPγS (green) is bound at a composite site
1397 created by the Walker/P-Loop residues Thr 234 and Lys 235 (orange), Walker B
1398 residues Asp 340 and Glu 259 (cyan) from chain A, and the β-hairpin arginine
1399 finger residues Lys 437 and Arg 439 from chain F. Chains A (grey) and F
1400 (magenta) are depicted in the ribbon format.

1401

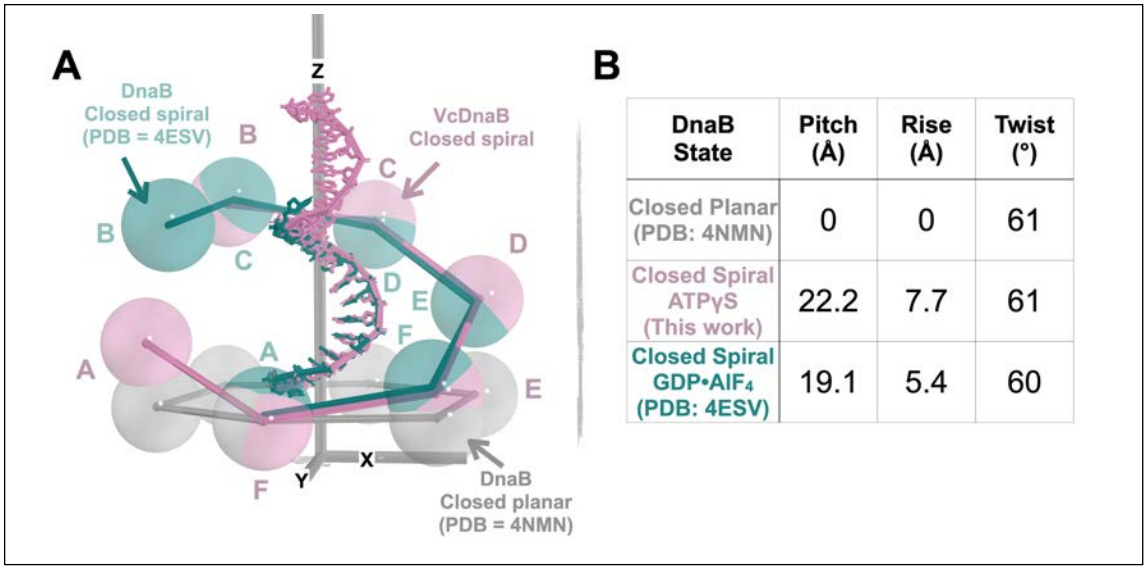

DnaB State	Pitch (Å)	Rise (Å)	Twist (°)
Closed Planar (PDB: 4NMN)	0	0	61
Closed Spiral ATPγS (This work)	22.2	7.7	61
Closed Spiral GDP•AlF$_4$ (PDB: 4ESV)	19.1	5.4	60

Supplementary Figure 9. The CTD Tier of DnaB Populates Distinct States as a Function of Nucleotide. A) The CTD tiers are presented as interconnected spheres centered on the indicated DnaB structures. The closed spiral (pink) of the ATPγS *Vc*DnaB CTD layer is displayed against the corresponding closed spiral CTD layer from *Bst* GDP•ALF$_4$ (PDB: 4ESV (12), deep teal) and the closed planar form (PDB: 4NMN (36), grey). The CTD of chain A of the GDP•AlF4 4ESV structure was superimposed onto the CTD of chain A of 4NMN (RMSD = 1.0 Å over 210 Cα atoms). The CTDs of the VcDnaB structure (excluding chain A) were aligned to the CTDs of 4ESV (excluding chain B) by superimposing the ssDNA species (depicted above in the color of the parent structure) in each structure, resulting in an alignment of CTDs with an RMSD = 1.7 Å over 1016 Cα atoms. This alignment positions *Vc*DnaB-ssDNA chain F atop chain A of 4ESV. The 4NMN structure is aligned to the XY plane, with the Z-axis passing through the central chamber. The chains for the CTD spheres corresponding to the 4ESV and *Vc*DnaB structures are labeled in the color of the underlying structure. B) Helical parameters (pitch, rise, and twist) for the specified states of the DnaB CTD.

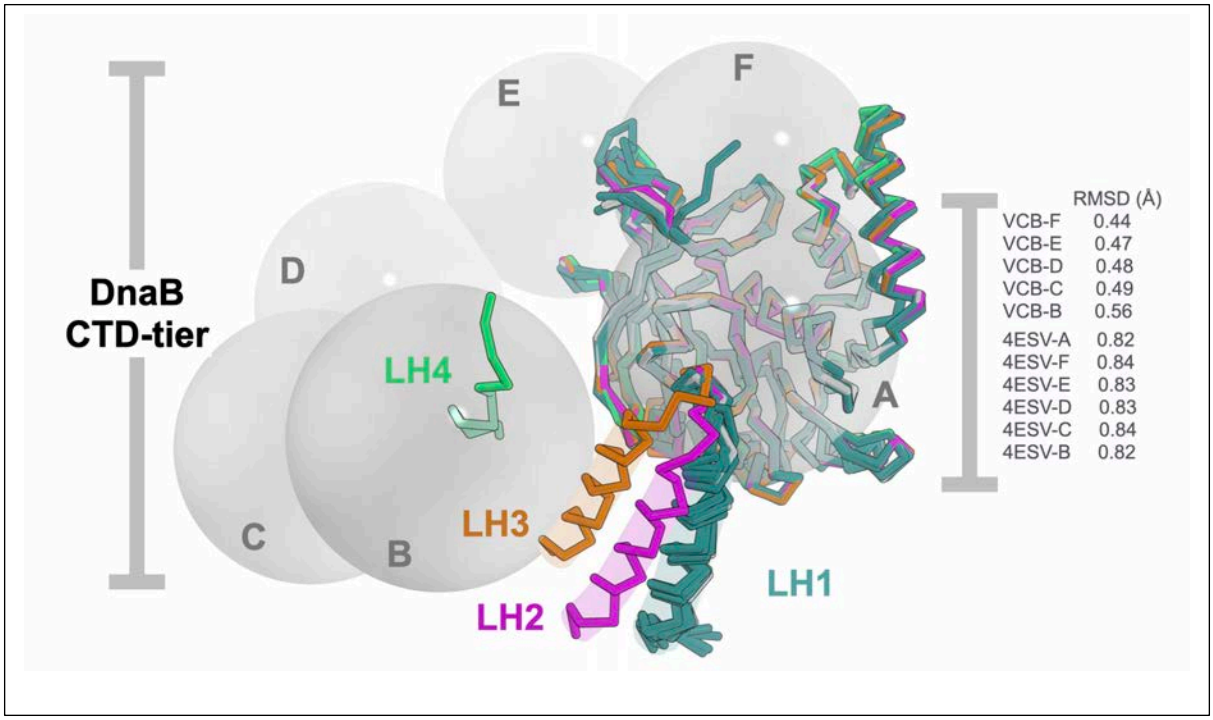

Supplementary Figure 10. The DnaB Linker Helix (LH) Element is a Moving Part During Translocation on ssDNA. Superposition analysis of the Vc ATPγS and GDP•AlF_4 structures reveals that the LH element of DnaB occupies at least four positions, termed LH1, LH2, LH3, and LH4. The CTDs (total of 11) of the *Vc* and Bst structures were superimposed on residues 204:465 of *Vc* chain A (residues corresponding to the LH 178:205 or DH 287:304 elements were omitted from the calculation). The four positions of the LH are colored in deep teal (LH1), magenta (LH2), orange (LH3), and lime-green (LH4). Except for chains A (LH3) and F (LH2), the *Vc* DnaB chains populate the LH1 position. Chain A of the Bst-4ESV structure occupies the LH4 position, while the others are observed in the LH1 position. The CTD layer of the *Vc* structure is shown as labeled spheres drawn at the centers of mass of each CTD. The superimposed CTDs are drawn in the ribbon representation, and the transparent cylinder indicates the LH.

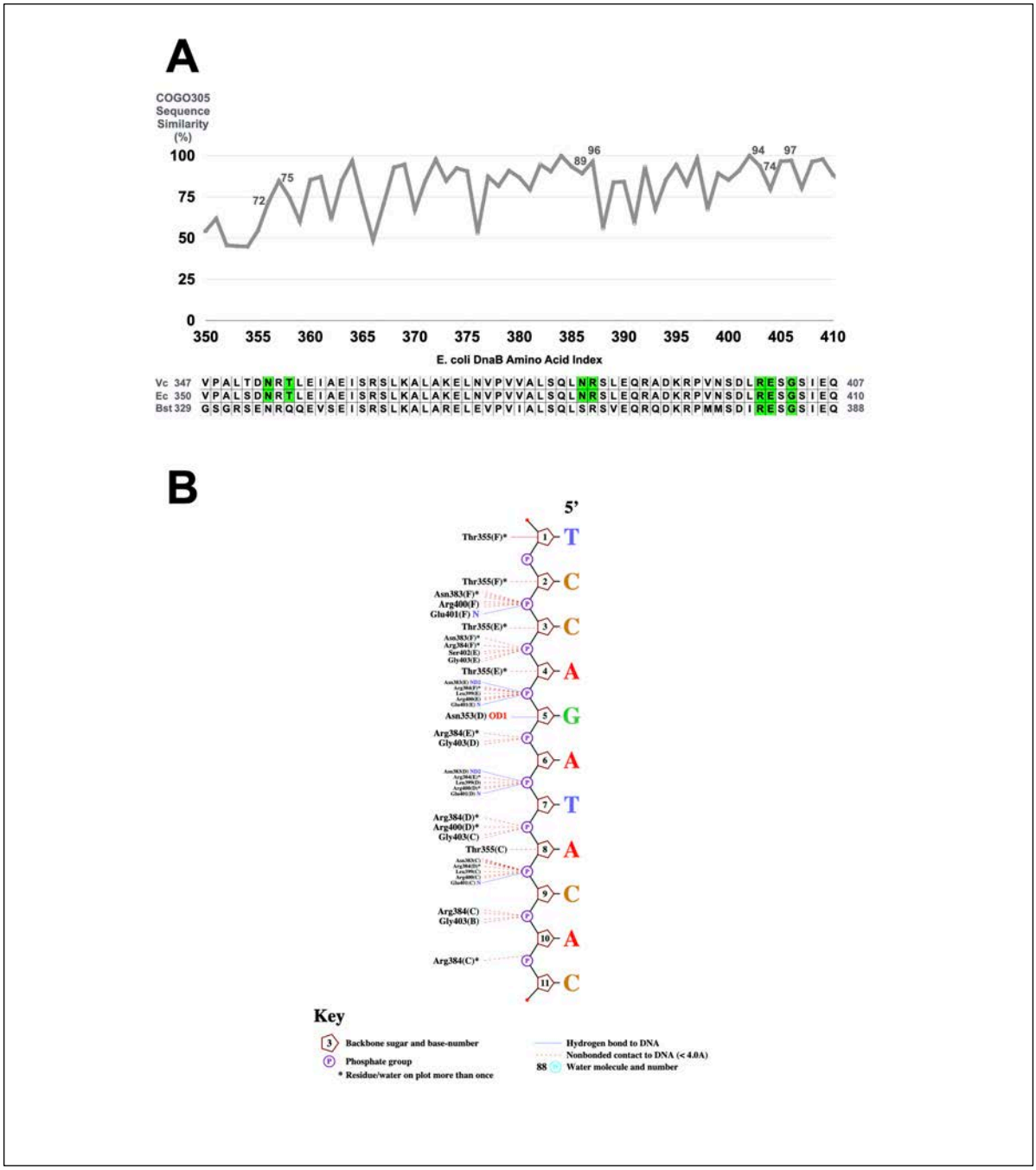

Supplementary Figure 11. Protein–ssDNA interactions in the *Vc*DnaB-ssDNA complex. A) Sequence identity is plotted against the amino acid index of a portion of the sequence alignment derived from the DnaB COG0305 conserved protein domain family (100 sequences). Seven *Vc*DnaB residues are in contact with ssDNA, though not every subunit uses each residue. These are N353, T355,

1437 N383, R384, R400, E401, and G403 (highlighted in green). The sequence
1438 alignment teaches that these residues are conserved in the COG0305 DnaB-
1439 family. The conservation value for each contact residue is listed in the plot. The
1440 residues used by *E. coli* (PDB: 7T20 (17)) and Bst (PDB: 4ESV(12)) are also
1441 highlighted. B) *Vc*DnaB-ssDNA contacts are depicted schematically as drawn by
1442 Nucplot (37).
1443

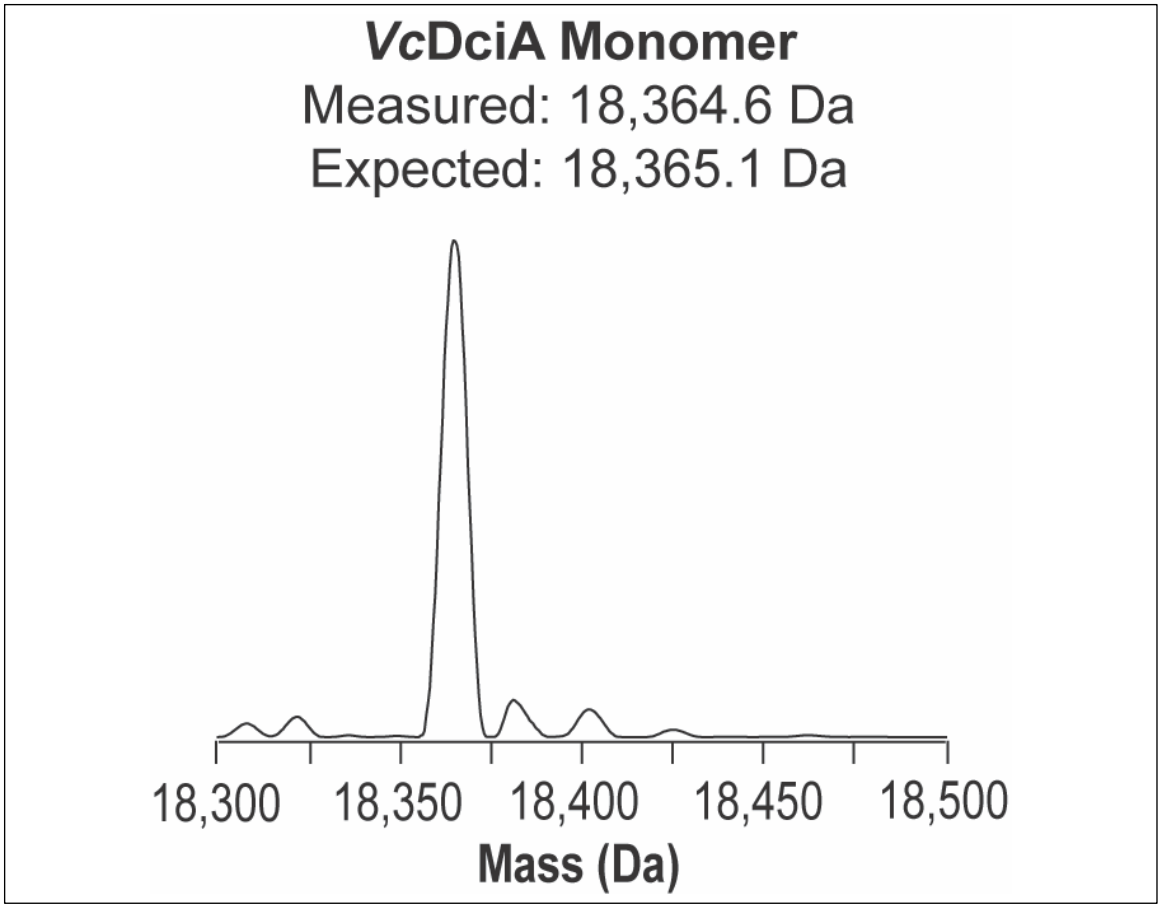

1444 **Supplementary Figure 12. Isolated *Vc*DciA is a monomer.** Deconvolved nMS
1445 spectra of *Vc*DnaB.
1446

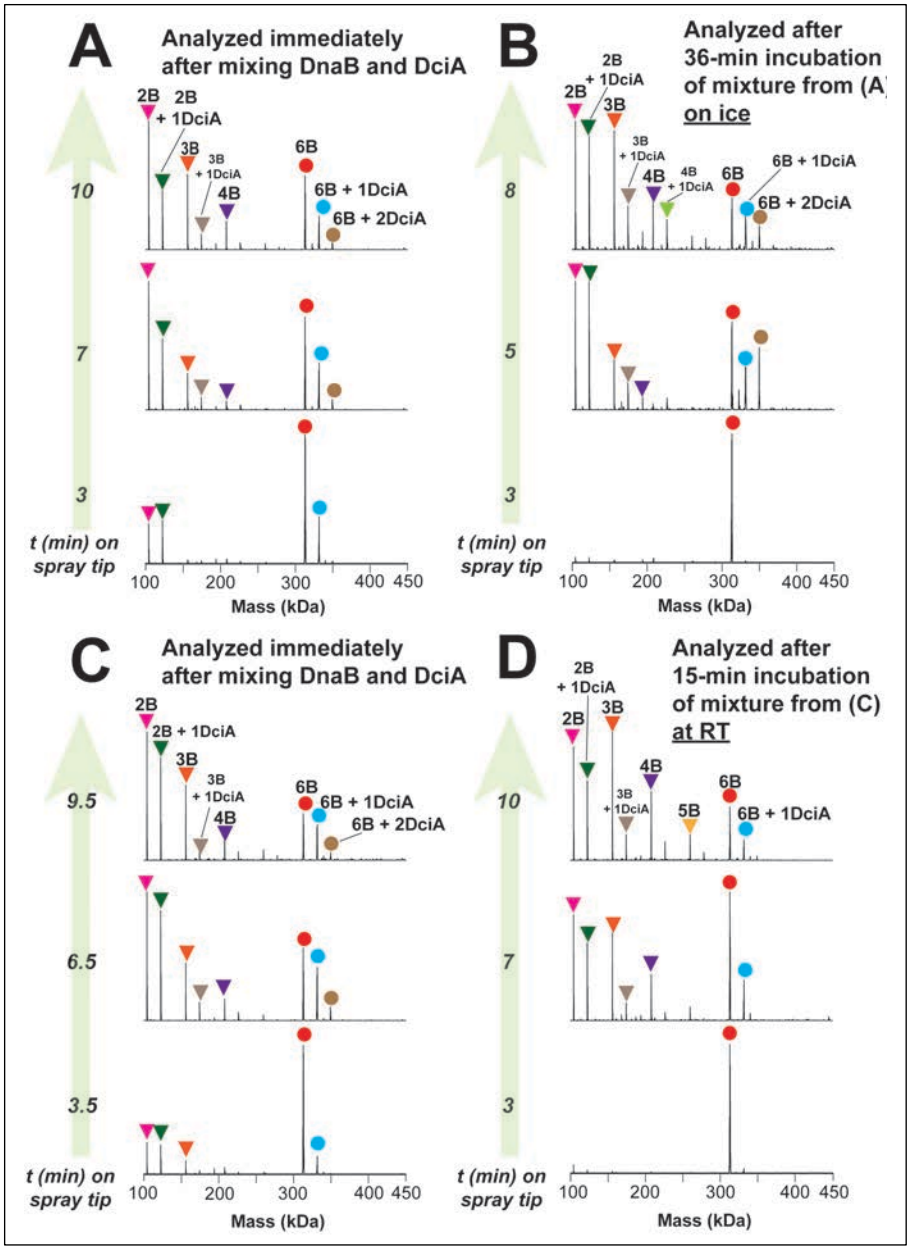

Supplementary Figure 13. Disassembly of *Vc*DnaB upon incubation with *Vc*DciA during nMS analysis. *Vc*DnaB was mixed with *Vc*DciA, and an aliquot of the mixture was loaded immediately on the electrospray tip for nMS analysis (A and C), and the rest of the mix was either incubated on ice for 36 min (B) or at room temperature for 13 min (D) before nMS characterization. The deconvolved spectra at specific time points during the nMS analysis (~100 scans averaged) and the corresponding peak assignments are shown for each sample. The overall

1454 delay time from loading the sample into the tip, setting up the electrospray, and
1455 initiating nMS data acquisition is typically 2 min. The sample mixture comprised
1456 10 μM DnaB and 7 μM DciA in 10 μM ATP, 0.5 mM magnesium acetate, 500 mM
1457 ammonium acetate, and 0.01% Tween-20. The peaks for $DnaB_6$ and $DnaB_6$ +
1458 $DciA_1$ predominate during the first 1-3 minutes of initiating the electrospray, and
1459 then peaks with increasing intensities for $DnaB_2$, $DnaB_2$ + $DciA_1$, and other DnaB
1460 subcomplexes appear, indicating the progressive disassembly of $DnaB_6$. Analysis
1461 of the rest of the sample incubated on ice or at room temperature (RT) resulted in
1462 similar time-resolved mass spectrometry (MS) profiles, suggesting that $DnaB_6$
1463 dissociation only occurs during electrospray. Overall, the results indicate that DciA
1464 binding can destabilize $DnaB_6$, and this destabilization is intensified during the
1465 electrospray process, leading to $DnaB_6$ disassembly.
1466

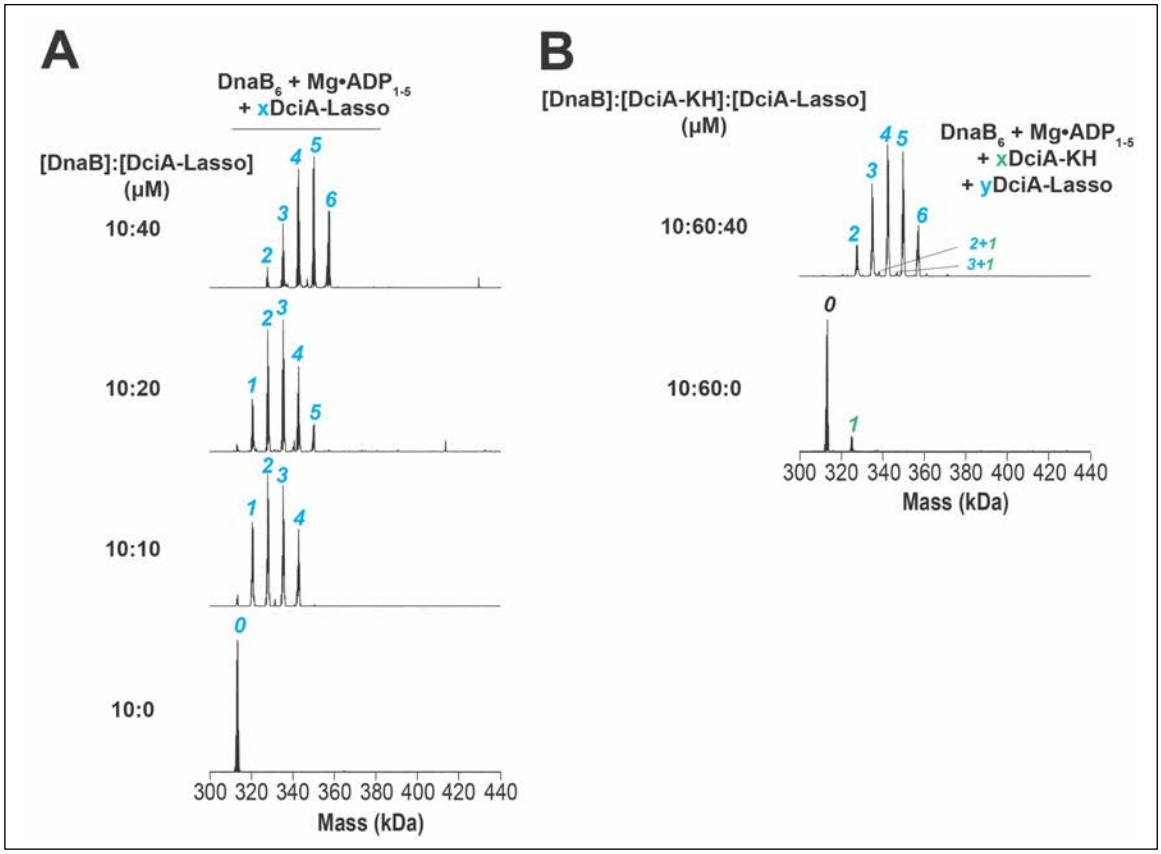

Supplementary Figure 14. Stoichiometry of binding the *Vc*DciA KH domain, the *Vc*DciA Lasso, and ssDNA to *Vc*DnaB by nMS. Deconvolved nMS spectra of (**A**) DnaB titrated with increasing concentrations of DciA-Lasso, and (**B**) DnaB incubated with an excess of DciA's KH domain in the absence or presence of DciA's Lasso domain. The expected masses of *Vc*DnaB$_6$ = 311.5 kDa, DciA-KH = 11.8 kDa, DciA Lasso = 7.5 kDa, and ssDNA = 32.5 kDa. The colored numbers and Roman letters 'X' and 'Y' indicate the number of DciA-Lasso domains bound (A) or DciA-KH and Lasso bound (B).

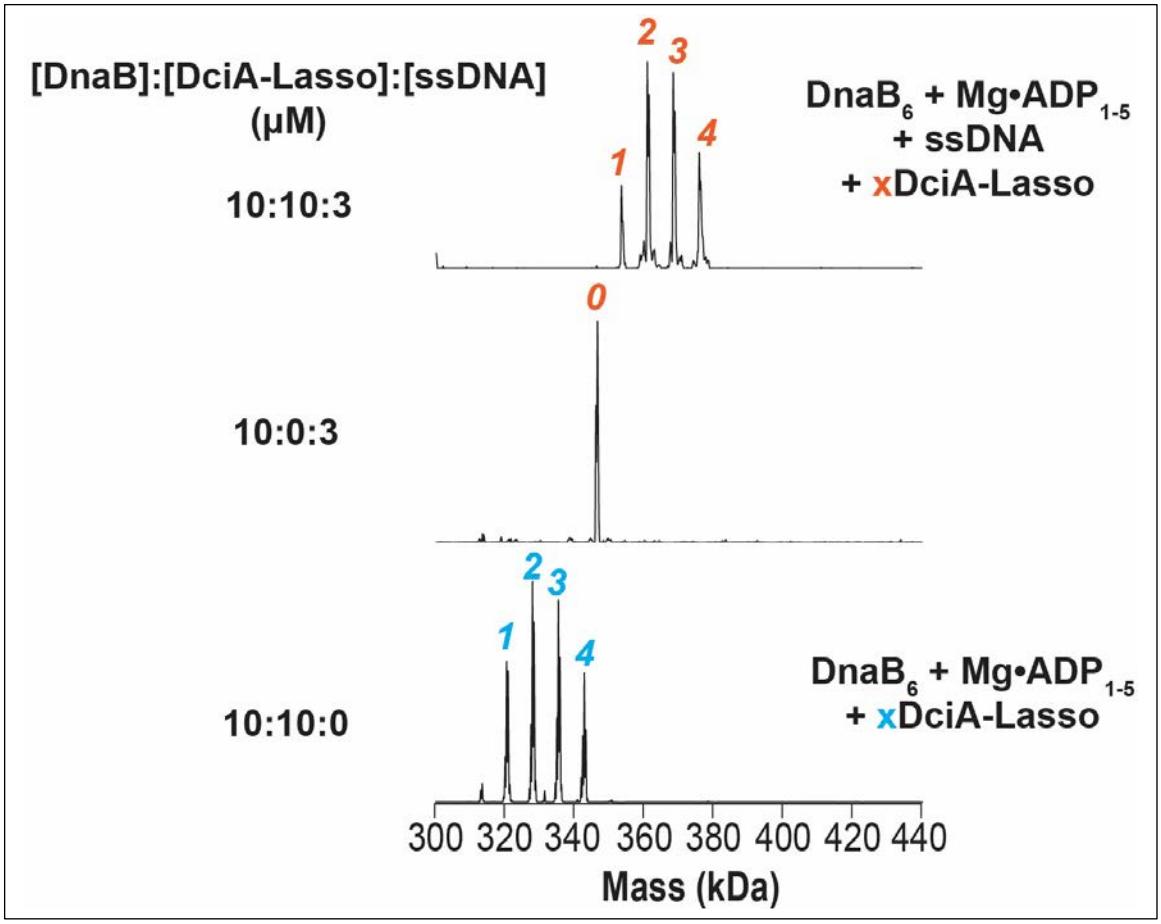

Supplementary Figure 15. The *Vc* Lasso domain forms complexes with *Vc*DnaB and ssDNA. Up to 4 *Vc* Lasso domains are found in *Vc*DnaB complexes, whether ssDNA in the absence/presence of ssDNA. Deconvolved nMS spectra of DnaB and ssDNA (O4-*Vc*F) incubated with and without an equimolar concentration of DciA-Lasso. All samples are prepared in 10 μM ATP, 500 μM magnesium acetate, 500 mM ammonium acetate, and 0.01% Tween-20 before nMS analysis. Spectra were collected at the indicated DnaB, DciA-Lasso, and ssDNA ratios. The blue and red Roman letter 'X' indicates the number of copies of *Vc*DciA revealed by nMS for a given sample. The expected masses are $DnaB_6$ = 311.5 kDa, DciA-KH = 11.8 kDa, DciA Lasso = 7.5 kDa, and ssDNA = 32.5 kDa.

1487

1488

1489

1490

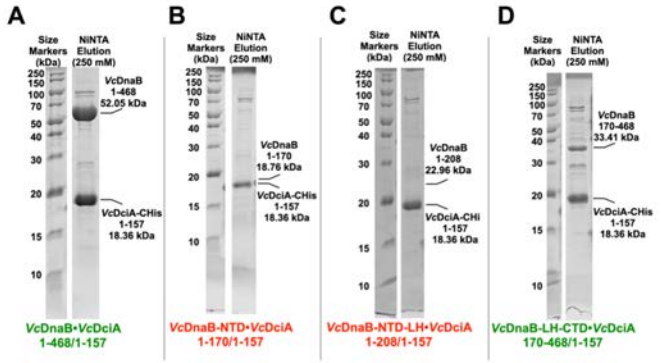

E

	VcDciA 1-157
VcDnaB 1-468	Yes
VcDnaB-NTD 1-170	No
VcDnaB-NTD-LH 1-208	No
VcDnaB-LH-CTD 171-468	Yes
VcDnaB-CTD 208-468	N/D

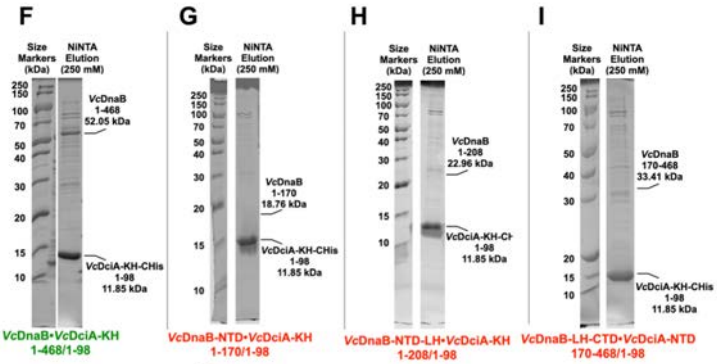

J

	VcDciA-KH 1-98
VcDnaB 1-468	Yes
VcDnaB-NTD 1-170	No
Vc-DnaB-NTD-LH 1-208	No
Vc-DnaB-LH-CTD 171-468	No
Vc-DnaB-CTD 208-468	N/D

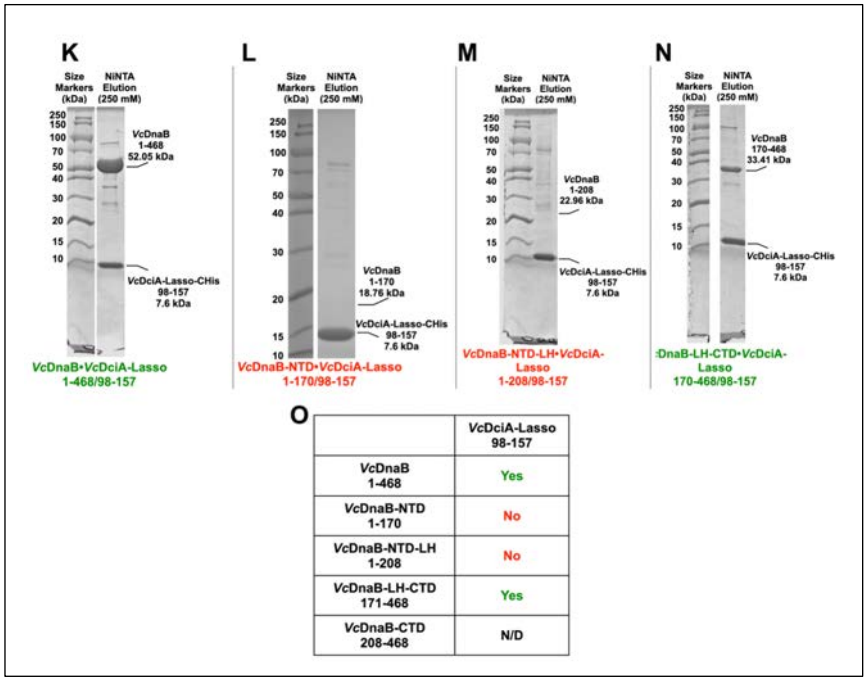

	VcDciA-Lasso 98-157
VcDnaB 1-468	Yes
VcDnaB-NTD 1-170	No
VcDnaB-NTD-LH 1-208	No
VcDnaB-LH-CTD 171-468	Yes
VcDnaB-CTD 208-468	N/D

Supplementary Figure 16. *Vc*DciA binds tightly to *Vc*DnaB, and the *Vc*DciA-Lasso domain prefers the LH-CTD domain. Composite image of 12 NiNTA 'pull down' assay between *Vc*DciA (full-length: 1:157; KH: 1:98; Lasso: 98:157) and DnaB (full-length: 1:468; NTD: 1:170; NTD-LH: 1:208; LH-CTD: 171:468; CTD: 208:468) constructs. A-D) Full-length *Vc*DciA and various *Vc*DnaB constructs. E) Summary of binding data from panels A-D; the *Vc*DnaB CTD (residues 208:468) could not be stably expressed. F-I) *Vc*DciA KH domain (1:98) and various *Vc*DnaB constructs. J) Summary of binding data from panels F-I. K-N) *Vc*DciA Lasso domain (98:157) and various *Vc*DnaB constructs. O) Summary of binding data from panels K-N. The green text indicated a NiNTA pull-down scored as interacting, while the red text indicated that no interaction was observed. These data show that full-length *Vc*DciA binds to full-length *Vc*DnaB and that the Lasso domain binds to the LH-CTD, likely at the DH-LH interface, as with other helicase loaders (4, 7–9, 13, 15).

1505

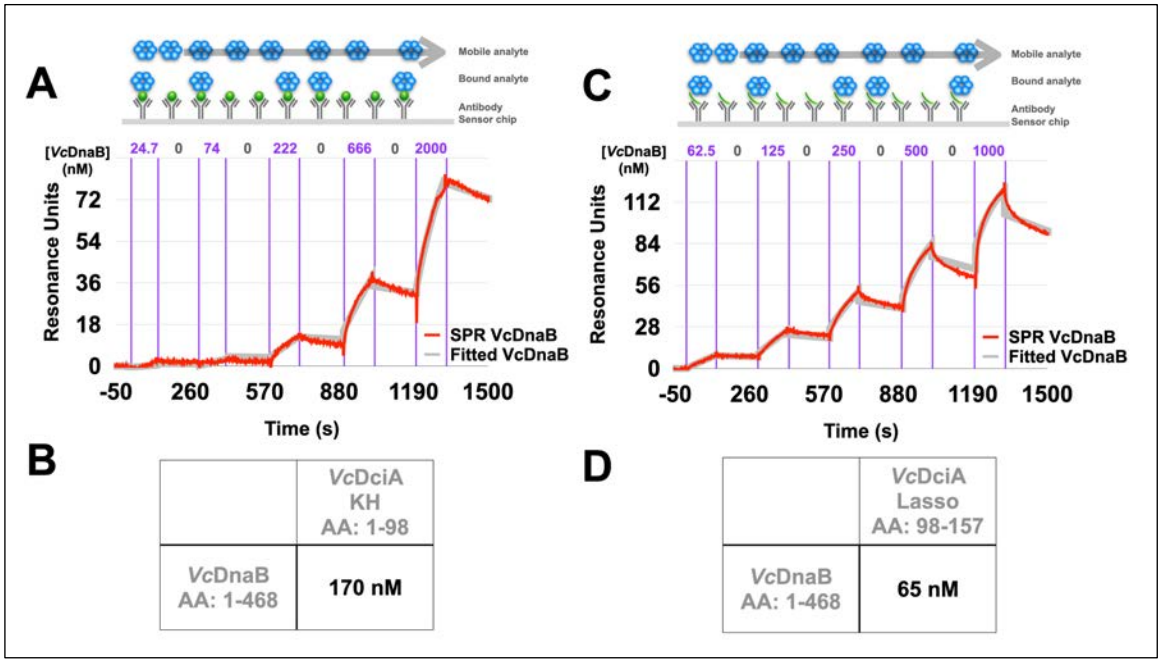

Supplementary Figure 17. The *Vc*DciA KH and Lasso Domain Retain Affinity to *Vc*DnaB, albeit with a Higher K_D. A) On and off rates with *Vc*DnaB at incremental concentrations (24.7, 74, 222, 666, 2000 nM) were measured by immobilizing cognate C-terminal His-tagged *Vc*DciA-KH to the SPR sensor chip. The single-cycle kinetic analyses through SPR revealed how DciA's KH domain exhibited a decreased affinity to *Vc*DnaB. The *Vc*DciA KH domain displays a K_D = 170 nM (Chi^2 = 1.82; R_{max} = 135.2), representing a ~300-fold reduction compared to full-length (A, B). C) Same as panel A except that slightly different incremental concentrations (62.5, 125, 250, 500, 1000 nM) were used. D) The *Vc*DciA Lasso domain features a K_D of 65 nM (Chi^2 = 5.89; R_{max} = 126.3). The 170 nM and 65 nM K_D measured for the KH and Lasso domains contrast with the 0.58 nM value measured for full-length DciA. The SPR experiments are diagrammed schematically above each trace. The experimental data were fitted as described in the methods. The raw SPR signal is shown in red, and the fitted model is depicted in grey.

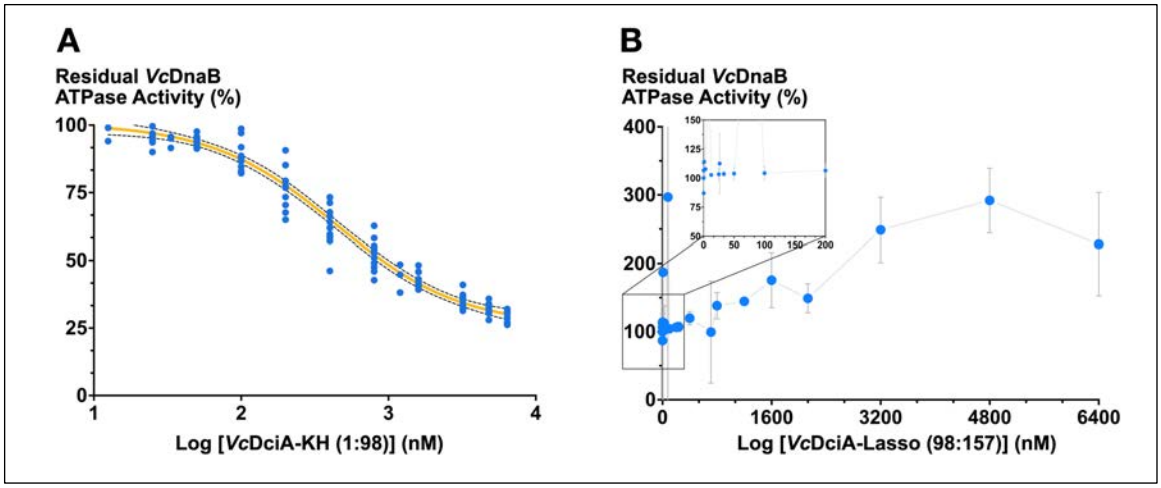

1521 **Supplementary Figure 18. The *Vc*DciA KH, but not the Lasso, domain**
1522 **partially retains the ATPase suppression activity.** A) The IC_{50} calculation
1523 described in Figure 7B was applied to the *Vc*DciA KH and Lasso domains. The
1524 *Vc*DciA KH domain represses *Vc*DnaB ATPase activity with an IC_{50} of 443 nM (R^2
1525 = 0.9693; 95% confidence interval: 380.5 to 520.0 nM), representing a 16-fold
1526 lower potency than the full-length loader. The blue dots represent individual
1527 measured ATPase rates plotted on a log scale. A non-linear fit (light-orange line),
1528 calculated using the Sigmoidal, 4PL model as implemented in PRISM, is
1529 superimposed on the experimental data. The dashed lines represent the 95%
1530 confidence interval (CI). These experiments encompassed four independent
1531 protein batches. B) The same analysis applied to the *Vc*DciA Lasso domain
1532 revealed no effect on *Vc*DnaB's ATPase activity at low concentrations (0.11 – 200
1533 nM). However, the titration of a significant excess of the Lasso domain (800 –
1534 6400 nM) revealed a 2.8x stimulation of DnaB's ATPase activity at 4800 nM
1535 *Vc*DciA. The measured ATPase rates (blue dots) in the inset are plotted on a
1536 linear scale and connected with a grey line.

1537

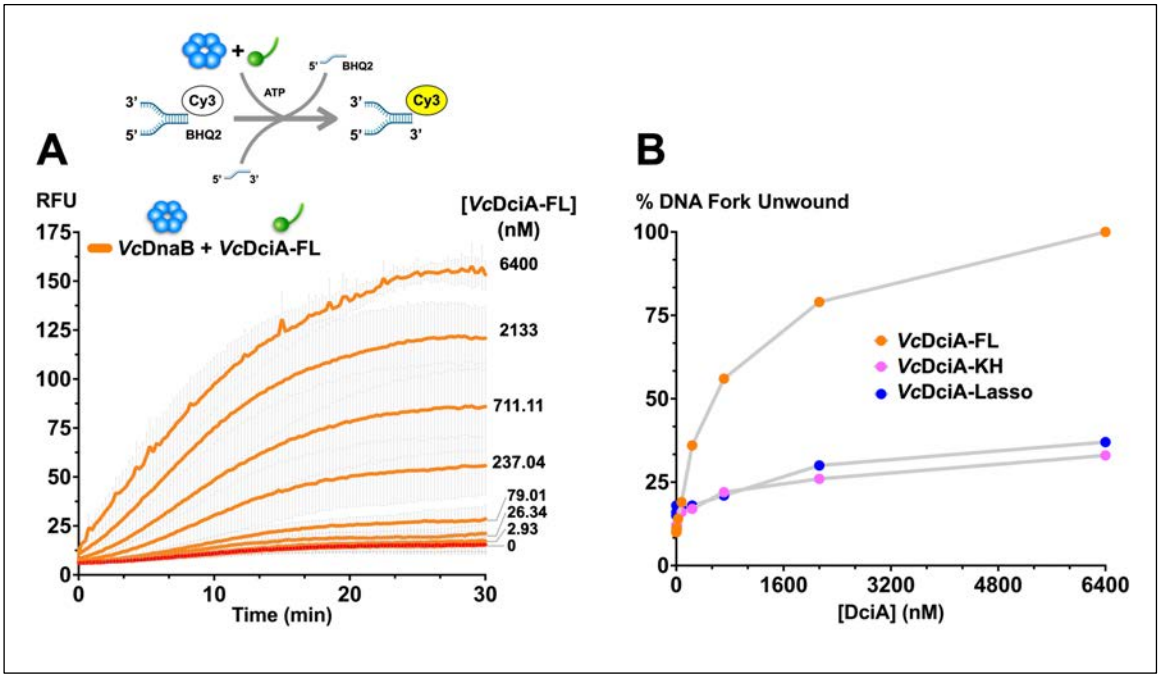

1538 **Supplementary Figure 19. *Vc*DciA stimulates the DNA unwinding activity of**
1539 ***Vc*DnaB in a concentration-dependent manner.** A) The unwinding experiments
1540 employed a FRET-based 5'- and 3'-tailed replication fork mimic, which is
1541 diagrammed schematically above. A time course of the evolution of fluorescence
1542 at 570 nm, due to relief of quenching at the Cy3/BHQ2 center during unwinding, is
1543 shown for unwinding experiments where the *Vc*DnaB concentration was held fixed
1544 at 200 nM, and the *Vc*DciA concentration varied from 0.11 to 6400 nM (orange
1545 curves). Shown in red is *Vc*DnaB's unwinding when *Vc*DciA was absent. The data
1546 indicate a 10-fold increase in unwinding. B) The data in panel A are plotted as a
1547 function of %DNA unwound, where the highest RFU value was considered 100%
1548 unwound. By this measure, the *Vc*DciA-KH (pink) and *Vc*DciA-Lasso (blue)
1549 domains exhibit 30% of the activity of full-length VcDciA. Control measurements
1550 lacking *Vc*DciA showed no unwinding, as was observed with the bubble substrate
1551 (Figure 8 and Supplementary Figure 25).

1552

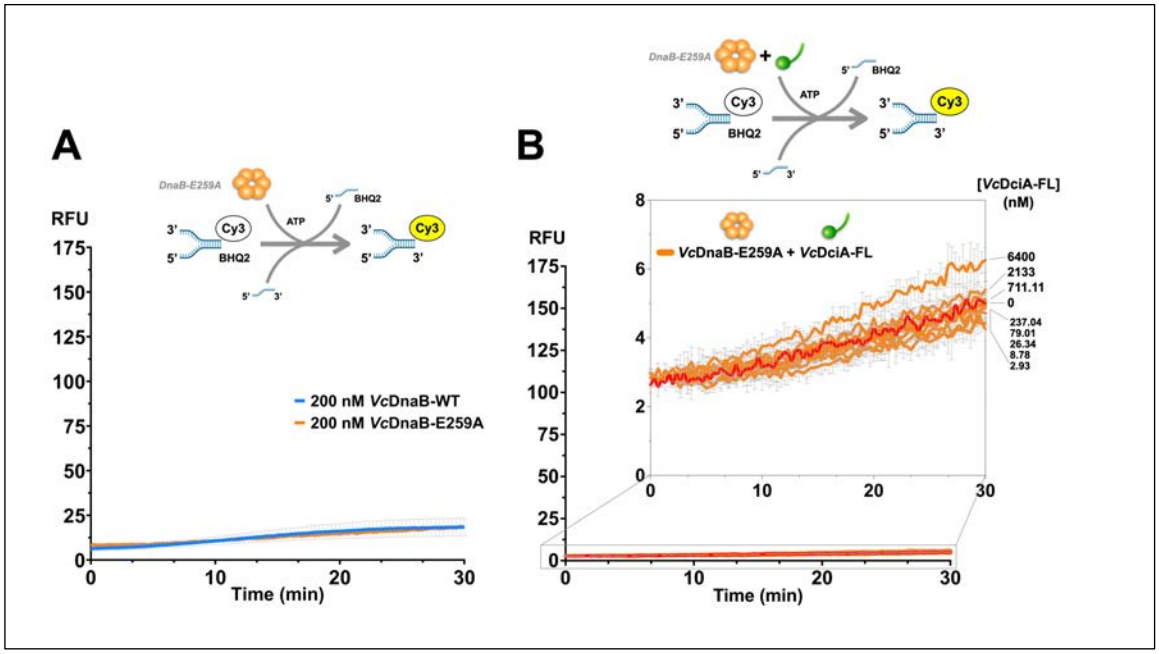

1553 **Supplementary Figure 20. The *Vc*DnaB Walker B glutamate (E259A) mutation**
1554 **Significantly Reduces DNA unwinding activity and *Vc*DciA-stimulated**
1555 **unwinding.** The FRET-based DNA unwinding experiments utilized a 5'- and 3'-
1556 tailed replication fork mimic, as diagrammed schematically above each panel. A)
1557 The time course of the 570 nm fluorescence signal due to the unwinding of the
1558 DNA substrate is plotted for wild-type (blue) and E259A mutant (orange) DnaB. In
1559 this experiment, the *Vc*DnaB concentration was held at 200 nM. The blue line
1560 represents the average of 27 replicates measured from 200 nM *Vc*DnaB-WT. Both
1561 wild-type and the E259A mutation show a slight basal fluorescence signal increase
1562 in the DNA fork unwinding assay. Although the E259A mutant behaves like wild-
1563 type in the fork unwinding assay, adding *Vc*DciA (panel B) does not stimulate it as
1564 seen for wild-type (Supplementary Figure 19). B) The time course of the 570 nm
1565 fluorescence signal arising from titration of *Vc*DciA (0.11-6400 nM) into an assay
1566 containing the Walker B *Vc*DnaB-E259A mutant. Essentially, no unwinding activity
1567 was recovered. The inset shows the same data but expands a section of the plot.

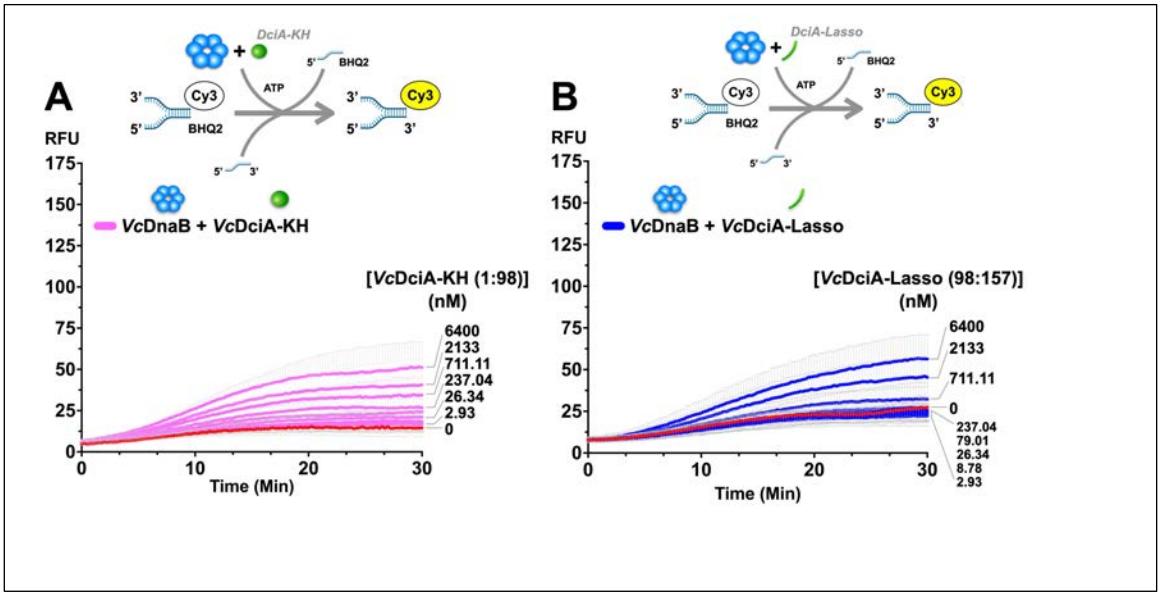

Supplementary Figure 21. The Isolated KH and Lasso Domains Retain 30% of the Potency of Full-length VcDciA in Stimulating Unwinding by VcDciA. The FRET-based DNA unwinding experiments utilized a 5'- and 3'-tailed replication fork mimic, as diagrammed schematically above each panel. Titration of *Vc*DciA-KH (pink, A) or DciA-Lasso (blue) domains into the assay stimulated DnaB's unwinding activity by only 30% compared to full-length DciA. The titration of the appropriate DciA-construct encompassed concentrations from 0.11 to 6400 nM. At most, the isolated KH and Lasso domains stimulated DNA unwinding by 3.3-fold compared to a sample lacking DciA. In contrast, full-length DciA produces a 10-fold increase (Supplementary Figure 19).

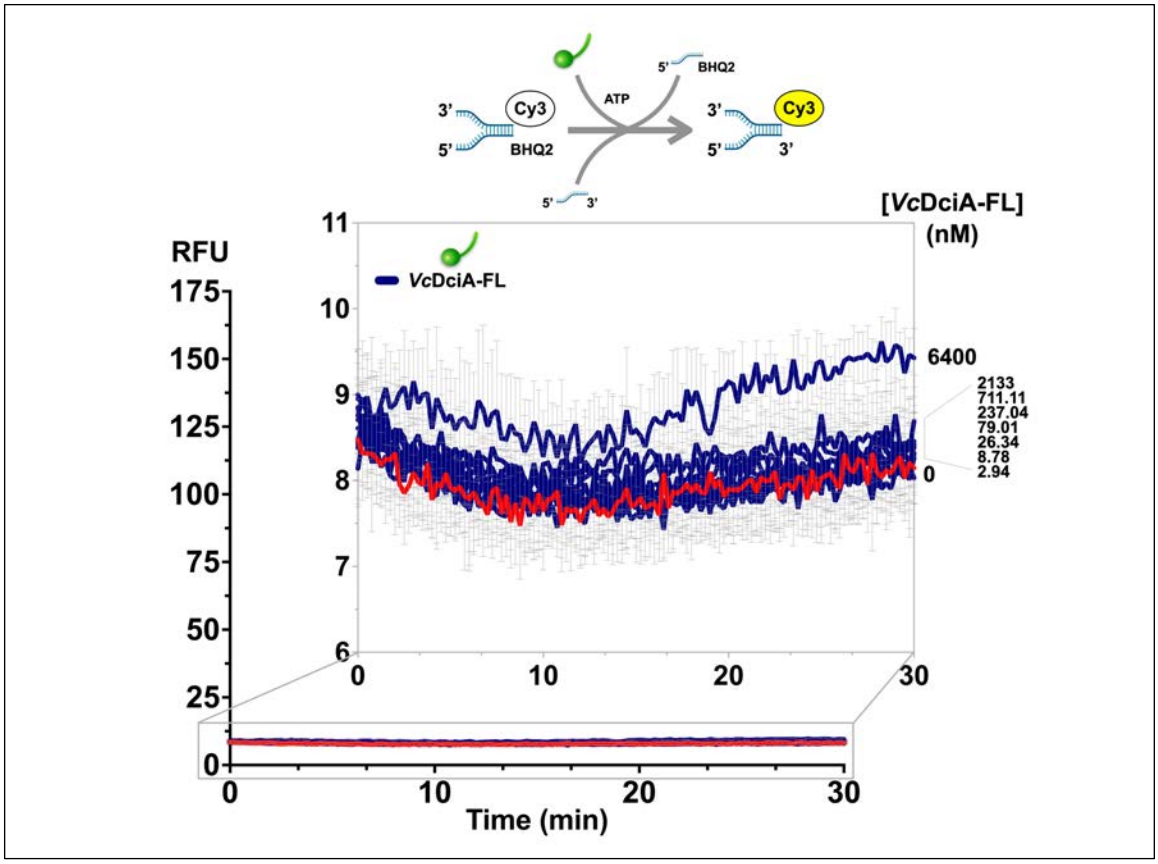

Supplementary Figure 22. Isolated *Vc*DciA fails to unwind the 5'- and 3'-tailed replication fork mimic. Titration from 0-6400 nM (blue curves) of *Vc*DciA into an assay that lacks DnaB, as diagrammed schematically above, fails to show any 570 nm fluorescent signal arising from unwinding of the DNA. The inset shows a plot section expanded around RFU values of 6-11. The red curve describes fluorescent signals from an experiment that lacked DciA. These data suggest that DciA alone fails to unwind the fork DNA substrate, a finding that contrasts with the robust unwinding observed with the DNA bubble substrate. The reason for this difference in activity is unknown.

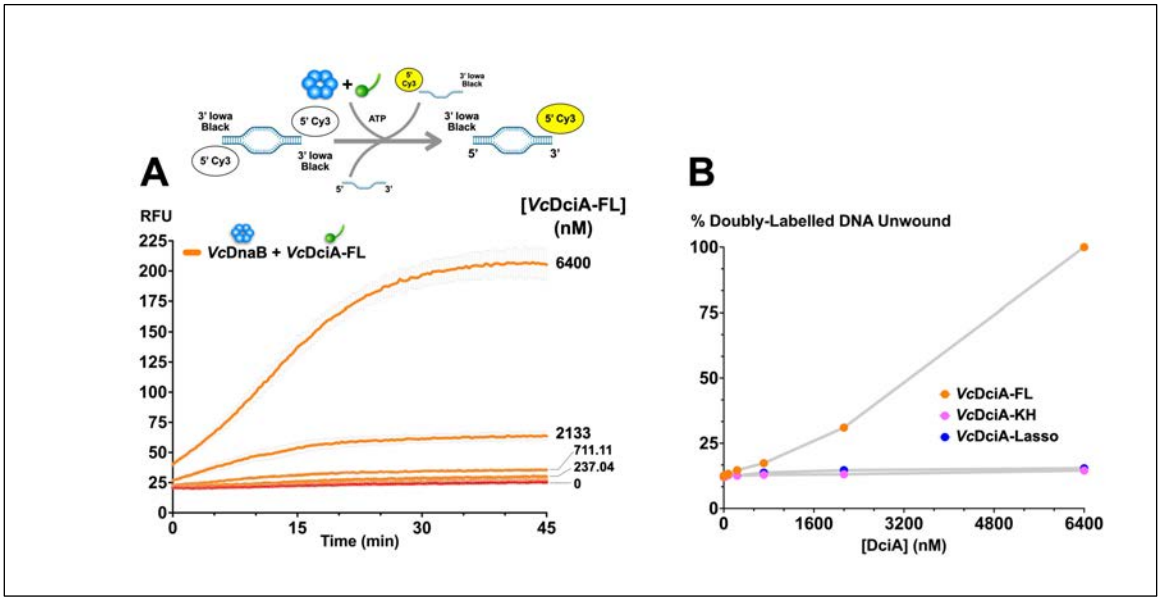

Supplementary Figure 23. Measurement of *Vc*DciA-mediated loading of *Vc*DnaB using a doubly labeled DNA bubble. The assay diagrammed above was performed precisely as the singly labeled DNA bubble substrate in Figure 7, except that FRET labels were included at both ends of the DNA bubble. A) A time course (orange curves) of fluorescence at 570 nM was recorded from an experiment wherein *Vc*DciA was titrated from 0.11 to 6400 nM while the *Vc*DnaB concentration was fixed at 200 nM. The red curve shows the signal from an experiment that lacked *Vc*DciA. Surprisingly, the amplitude of the fluorescence signals did not increase twofold compared to the singly labeled, as was expected, given the presence of two fluorescence centers. Instead, the signal increased by 10%. B) Data from panel A are plotted as a percentage of DNA unwound as a function of *Vc*DciA concentration. These data show no loading activity by the *Vc*DciA-KH (pink) or Lasso domains (blue), even with a significant excess of each domain (Supplementary Figure 25).

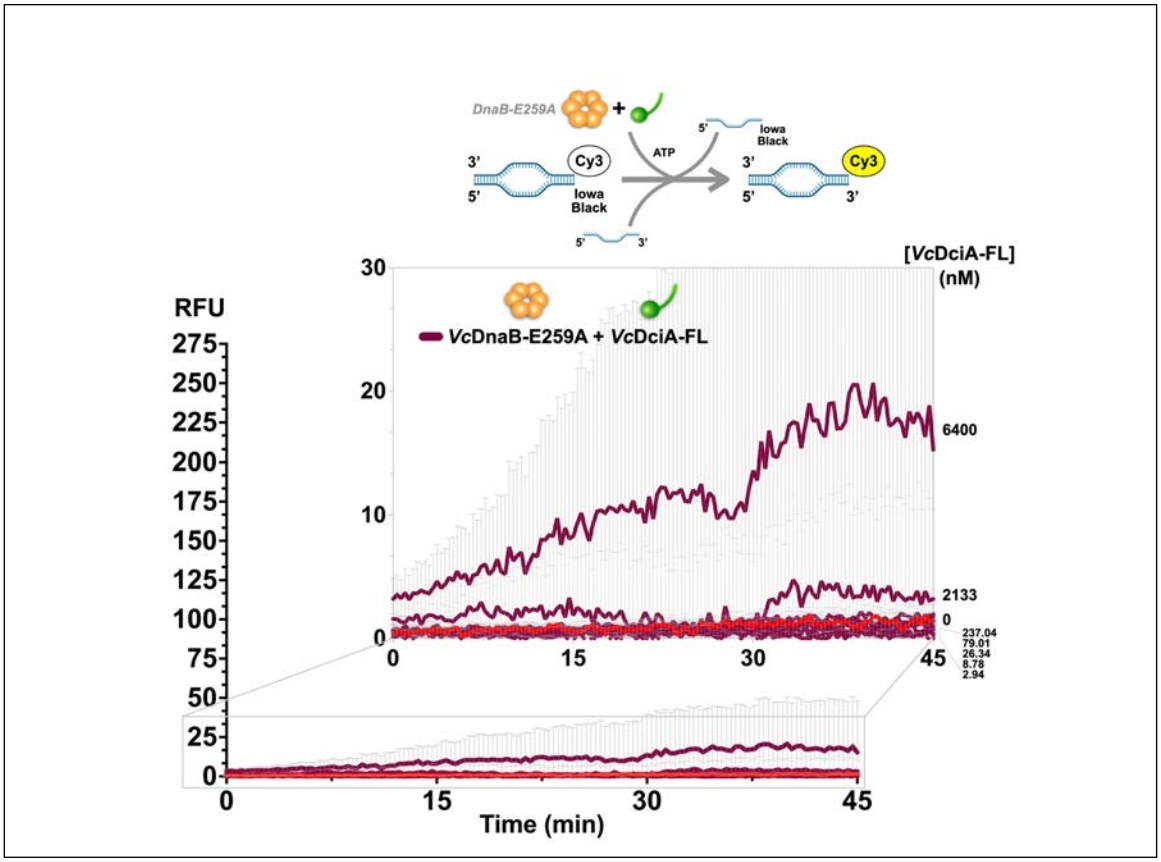

Supplementary Figure 24. The *Vc*DnaB Walker B glutamate (E259A) mutation is deficient in loading onto a physiological bubble substrate. This experiment, diagrammed above, is similar to the one shown in Supplementary Figure 22, except that a DNA bubble substrate is used. The plot illustrates a point-by-point subtraction of the fluorescence signals generated by *Vc*DciA, as shown in Figure 7 B. The resulting curves (orange) show little loading activity above the basal rate measured without DciA (red). Only when DciA is present at 6400 nM is a curve with significant activity above the basal rate observed. However, the amplitude of this curve (~15) was 30% of the amplitude seen with wild-type *Vc*DnaB. The inset shows the same data but expands a section of the plot.

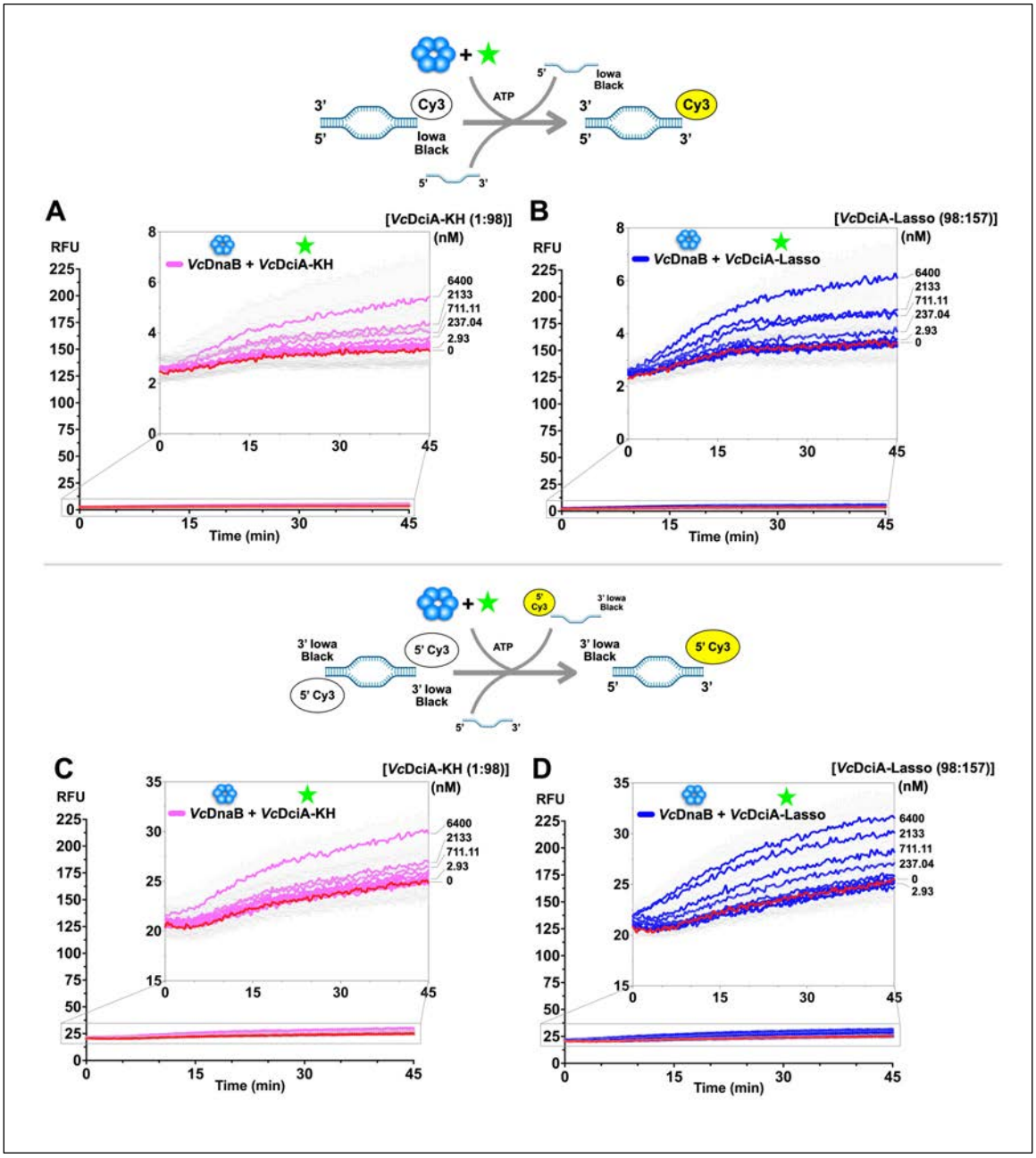

1615 **Supplementary Figure 25. The isolated *Vc*DciA KH and Lasso domains are**
1616 **inactive in the bubble-loading assay.** These measurements, diagrammed
1617 above each panel, represent controls for parallel studies with full-length *Vc*DciA.
1618 Panels A and B employ the singly labeled substrate, and panels C and D employ
1619 the doubly labeled substrate. Titration of the appropriate DciA construct was
1620 carried out as described in Figure 7. Measurements with the *Vc*DciA-KH domain

are colored pink, and those with the *Vc*DciA-Lasso domain are colored blue. The red curves in each plot represent the basal rate of loading measured in the absence of *Vc*DciA. With the singly labeled substrate, a 1.5 to 2-fold increase in the fluorescence signal was seen at the highest concentration tested (6400 nM); in contrast, full-length *Vc*DciA produces a 10-fold increase (Figure 7). With the doubly labeled substrate, a ~1.2-fold increase in the fluorescence signal was seen at the highest concentration tested (6400 nM); in contrast, full-length *Vc*DciA produces an 8-fold increase (Supplementary Figure 25). The lack of differentiation of the DciA titration-derived curves from the basal rate (red) leads us to conclude that each *Vc*DciA truncated construct is inactive in helicase loading.

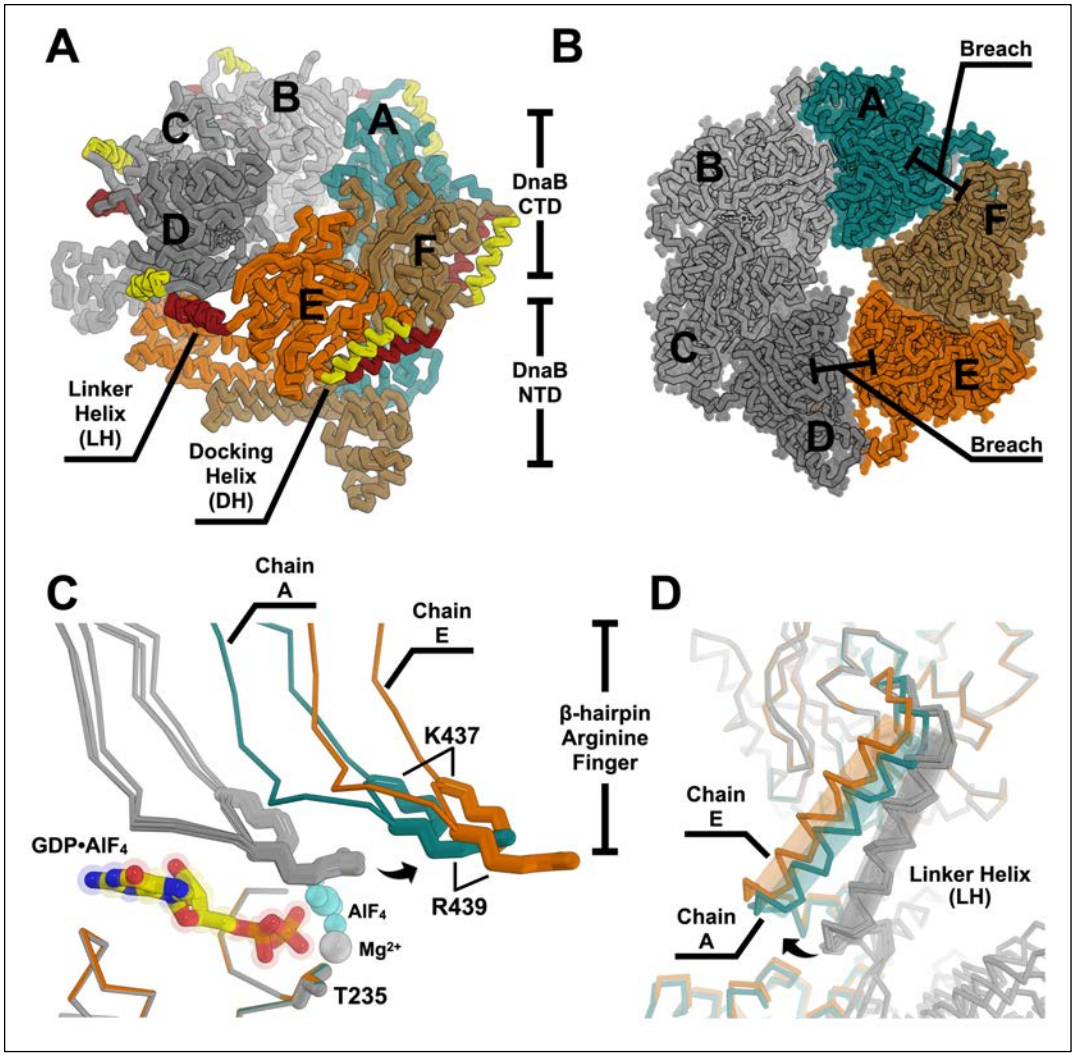

Supplementary Figure 26. Crystal Structure of *Vc*DnaB-GDP/AlF$_4$ (PDB: 6T66) and the disposition of β-hairpin arginine fingers and Linker Helix elements. A) *Vc*DnaB is depicted as a ribbon with chains labeled. The NTD and CTD layers are indicated. The six Docking-Helix (DH) and Linker-Helix (LH) elements are shown in yellow and red, respectively. Chains A, F, and E are shown in blue, sand, and orange, and the other chains are in alternating shades of gray. B) The 6T66 DnaB structure depicts the two breaches in the CTD layer: the largest is between chains E (orange) and D (grey), and the narrowest is between chains A (deep teal) and F (sand). The protein surface is drawn with the PyMol solvent radius = 0.3 setting. C) The six CTD pairs (A-B, B-C, etc., residue 200:461) from 6T66 were superimposed (RMSD = 0.03 Å) on chain A, but the DH elements

(residue 280:306) and the second chain were excluded from the calculation. Each *Vc*DnaB harbors a GDP•AlF_4 species, and only one is shown in the stick representation, which has transparent spheres overlaid. The β-hairpin arginine fingers are shown as ribbons, and K437 and K439 are shown as sticks. The β-hairpins from four chains (B, C, D, F) follow each other closely (grey), although not included in the alignment. The corresponding elements from chain A (deep teal) and E (orange) have moved away by ~9 Å and ~13 Å, respectively. D) The superposition from panel C was interrogated for the disposition of the LH elements represented as transparent cylinders. The LH elements from chains B, C, D, and F (grey) superimpose closely and occupy the LH1 position as defined in the main text and Supplementary Figure 10. In contrast, those belonging to chain A (deep teal) and chain E (orange) drift away by ~5-~9 Å and occupy position LH2.

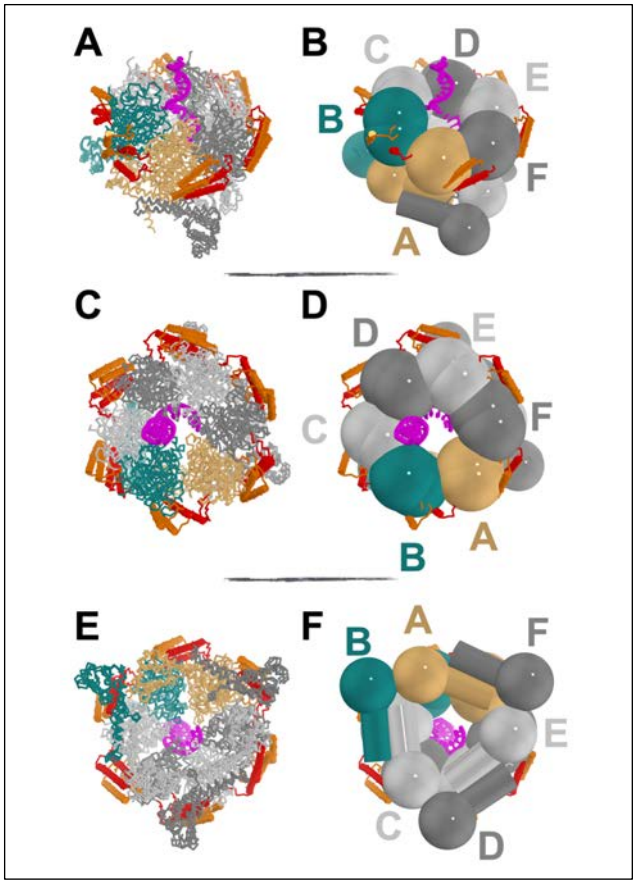

Supplementary Figure 27. Distinct Configuration in DnaB in the VcDnaB-ssDNA-ATPγS complex and the DnaB-DciA complex (PDB: 8A3V). The DnaB-DciA crystal structure was superimposed on the chain A NTD (residue 1:170) of the current VcDnaB-ssDNA-ATPγS complex (RMSD: 0.85 Å; 139 Cα carbons). DnaB is drawn in a ribbon representation (A, C, and E) or a schematic using the NTD-cylinder/sphere and CTD-spheres design language (B, D, and F) in the identical poses. ssDNA, colored in magenta, is depicted in a cartoon and stick representation. The superimposed structures are colored identically. Chain A (light orange), chain B (deep teal), and other DnaB subunits (colored in alternating shades of gray) are labeled. The Docking Helix (DH) and the Linker Helix (LH) are depicted as cylinders and ribbons colored orange and red. Panels A/B and D/E are related by a 30° rotation about the X-axis, and panels D/E and E/F are related by 180°. The dilated configuration of the NTD tier enabled superposition even of chains not included in the calculation (panels E and F), as indicated by the close positions of the NTD sphere and cylinder proxies. In contrast, individual CTDs vary between the two structures in this superposition.

The distinct conformations in the two DnaB structures can be seen in the positions of the DH and LH elements.

1682 **Supplementary Movie 1. Migration of Subunits from the Bottom to the Top**
1683 **of the DnaB Spiral during Translocation.** This video shows the transition from
1684 the ATPγS conformation of the present *Vc*DnaB-ssDNA complex to the GDP-AlF_4
1685 configuration of the GDP•AlF4 4ESV DnaB ssDNA (12) complex. The two
1686 complexes are aligned by superimposing the ssDNA molecules of each structure,
1687 as detailed in the main text. The motions depicted in the video are described in
1688 the main text. The DnaB-ssDNA-ATPγS complex is drawn in the ribbon
1689 representation (left) or the sphere/cylinder/ribbon schematic (right). Both
1690 representations are colored according to their chain. The ssDNA is depicted in
1691 both cartoon and stick representations and is colored orange. To calculate the
1692 transition between structures, a version of the 4ESV coordinates was constructed
1693 that encompassed the *Vibrio cholerae* primary sequence. The two states were
1694 then submitted to PyMol to calculate the 90 intermediate structures between the
1695 ATPγS and the GDP-AlF_4 conformers, as well as an additional 90 structures
1696 between the GDP-AlF_4 and the ATPγS structures. Frames were rendered in PyMol
1697 and assembled in QuickTime Player.

1698 # Supplementary Tables

1699 ## Supplementary Table 1. Expression Plasmids Used in This Study

Expression Plasmid	Insert	Template	Primers	Plasmid vector
pNG066-pET24a-*Vc*DnaB-unt	*Vc*DnaB-untagged	*V. cholerae* N16961 genomic DNA	*Vc*DnaB-NdeI-F, *Vc*DnaB-XhoI-R	pET24a
pNG067-pET24a-*Vc*DnaB-NHis	*Vc*DnaB-NHis	pNG066	*Vc*DnaB-pET24a-NHis-F, *Vc*DnaB-pET24a-NHis-R	pET24a
pNG072-pET24a-*Vc*DnaB-E259A-NHis	*Vc*DnaB-E259A-NHis	pNG067	*Vc*DnaB-E259A-F, *Vc*DnaB-E259A-R	pET24a
pNG114-pET24a-*Vc*DnaB-1to170-unt	*Vc*DnaB-NTD-untagged	pNG066	*Vc*DnaB_170-pET24a-F, *Vc*DnaB_170-pET24a-R	pET24a
pNG131-pET24a-*Vc*DnaB-1to208-unt	*Vc*DnaB-NTD_LH-untagged	pNG066	*Vc*DnaB_208-pET24a-F, *Vc*DnaB_208-pET24a-R	pET24a
pNG134-pET24a-*Vc*DnaB-170to468-unt	*Vc*DnaB-LH_CTD-untagged	pNG066	pET24a-*Vc*DnaB_170-F, pET24a-*Vc*DnaB_170-R	pET24a
pNG057-pCDFDuet-1-*Vc*DciA-CHis	*Vc*DciA-CHis	*V. cholerae* N16961 genomic DNA	*Vc*DciA-NdeI-F, *Vc*DciA-XhoI-CHis-R	pCDFDuet-1
pNG078-pCDFDuet-*Vc*DciA-1to98-CHis	*Vc*DciA-NTD-CHis	pNG057	*Vc*DciA_98-CHis_pCDF-F, *Vc*DciA_98-CHis_pCDF-R	pCDFDuet-1
pNG087-pCDFDuet-*Vc*DciA-98to157-CHis	*Vc*DciA-CTD-CHis	pNG057	*Vc*DciA_1-*Vc*DciA_98-F, *Vc*DciA_1-*Vc*DciA_98-R	pCDFDuet-1

1700

1701

1702 **Supplementary Table 2. Primers and Other DNAs Used in This Study**

DNA Name	DNA Sequence (5' to 3')
*Vc*DnaB-NdeI-F	GGGAGAGCATATGGCAGATCCACGTACTGATA
*Vc*DnaB-XhoI-R	GGGAGAGCTCGAGTTACTCATCGTCAAATGCAGGT
*Vc*DnaB-pET24a-NHis-F	CTTTAAGAAGGAGATATACATATGCATCACCATCACCATCACGCAGATCCACGTACTGATAATCG
*Vc*DnaB-pET24a-NHis-R	CGATTATCAGTACGTGGATCTGCGTGATGGTGATGGTGATGCATATGTATATCTCCTTCTTAAAG
*Vc*DnaB-E259A-F	GATCTTCTCGCTGGCGATGCCCGCCGAAC
*Vc*DnaB-E259A-R	GTTCGGCGGGCATCGCCAGCGAGAAGATC
*Vc*DnaB_170-pET24a-F	GCCGAAGCGCGTACCTAACTCGAGCACCAC
*Vc*DnaB_170-pET24a-R	GTGGTGCTCGAGTTAGGTACGCGCTTCGGC
*Vc*DnaB_208-pET24a-F	GAGTGAACACGGGCTTTTAACTCGAGCACCACC
*Vc*DnaB_208-pET24a-R	GGTGGTGCTCGAGTTAAAAGCCCGTGTTCACTC
pET24a-*Vc*DnaB_170-F	TAAGAAGGAGATATACATATGACCAGTGAAAATGAAGGCCCG
pET24a-*Vc*DnaB_170-R	CGGGCCTTCATTTTCACTGGTCATATGTATATCTCCTTCTTA
*Vc*DciA-NdeI-F	GGGAGAGCATATGCGTGATCACCGCCCTACC
*Vc*DciA-XhoI-CHis-R	GGGAGAGCTCGAGTCAGTGATGGTGATGGTGATGATCGTCTTTCTGATTTGCTT
*Vc*DciA_1-*Vc*DciA_98-F	TAAGAAGGAGATATACATATGCCTGAGTTGTATCGGCAAAGC
*Vc*DciA_1-*Vc*DciA_98-R	GCTTTGCCGATACAACTCAGGCATATGTATATCTCCTTCTTA
*Vc*DciA_98-CHis_pCDF-F	GAAGTGCGAGTCAATCCTCATCACCATCACCATCAC
*Vc*DciA_98-CHis_pCDF-R	GTGATGGTGATGGTGATGAGGATTGACTCGCACTTC
FRET-DNA-fork-top-strand	/5Cy3/TACGTAACGAGCCTGCTTTTTTTTTTTTTTTTTTTTTTTTT
FRET-DNA-fork-bottom-strand	TTTTTTTTTTTTTTTTTTTTTTTTTTGCAGGCTCGTTACGTA/3BHQ_2/
FRET-DNA-fork-capture-oligo	GCAGGCTCGTTACGTA
895	TCCTTGTTATCCACAGGGCAGTTTTTTTTTTTTTTTTTTT

1704 **Supplementary Table 3: Cryogenic Electron Microscopy Data Measurement**
1705 **and PDB Model Refinement.**

PDB	9DLS
EMDB	EMD-46984
Data Collection and Processing	
Microscope	Titan Krios
Voltage (kV)	300
Camera	Gatan K3
Magnification	81000
Defocus range (μm)	-0.7 - -2.9
Exposure time (ms)	2000
Electron dose (e^-/Å^2)	51.37
Number of frames collected (no.)	40
Number of frames processed (no.)	40
Calibrated pixel size (Å)	0.5413
Micrographs (no.)	12265
Total particle images (no.)	4315534
Refinement	
Particle per class (no.)	521399
Symmetry imposed	C1
Map resolution (Å), Gold-standard Fourier Shell Correlation = 0.143	3.37
Map sharpening B-factor (Å^2)	119.2
Map versus Model cross-correlation	0.7414
Model Composition	
Non-hydrogen atoms	21282
Protein residues	2648
Nucleotide residues	22
Ligand: ATPγS	6
Ligand: Mg^{2+}	6
Model Refinement	
Resolution limit (Å)	3.37
Number of chains	14
Number of residues	2648
B factors (Å^2)	
Protein	74.66
DNA	145.76
Ligand (ATPγS)	55.68
RMS deviations	

Bond lengths (Å)	0.002
Bond angles (°)	0.426
Validation	
MolProbity score	1.48
Clash score	4.88
Rotamer outliers (%)	2.00
Ramachandran plot (%)	
Favored (%)	98.07
Allowed (%)	1.93
Outliers (%)	0.00

1708 **Supplementary Table 4. Contacts (<4 Å) in the *Vc*DnaB-ssDNA complex.**

Model1	Chain1	Res1	ResN1	Atom1	to	Model2	Chain2	Res2	ResN2	Atom2	Dist
*Vc*B-ssDNA	B	THR	355	OG1	to	*Vc*B-ssDNA	G	DC	9	O2	3.947
*Vc*B-ssDNA	B	ASN	383	OD1	to	*Vc*B-ssDNA	G	DC	11	C5'	3.716
*Vc*B-ssDNA	B	ASN	383	ND2	to	*Vc*B-ssDNA	G	DC	11	O5'	3.771
*Vc*B-ssDNA	B	ASN	383	OD1	to	*Vc*B-ssDNA	G	DC	11	O5'	3.727
*Vc*B-ssDNA	B	ASN	383	CG	to	*Vc*B-ssDNA	G	DC	11	OP1	3.107
*Vc*B-ssDNA	B	ASN	383	ND2	to	*Vc*B-ssDNA	G	DC	11	OP1	2.651
*Vc*B-ssDNA	B	ASN	383	OD1	to	*Vc*B-ssDNA	G	DC	11	OP1	2.814
*Vc*B-ssDNA	B	ASN	383	ND2	to	*Vc*B-ssDNA	G	DC	11	OP2	3.263
*Vc*B-ssDNA	B	ASN	383	CG	to	*Vc*B-ssDNA	G	DC	11	P	3.922
*Vc*B-ssDNA	B	ASN	383	ND2	to	*Vc*B-ssDNA	G	DC	11	P	3.259
*Vc*B-ssDNA	B	ASN	383	OD1	to	*Vc*B-ssDNA	G	DC	11	P	3.784
*Vc*B-ssDNA	B	ASN	383	CA	to	*Vc*B-ssDNA	G	DA	12	OP2	3.423
*Vc*B-ssDNA	B	ASN	383	CB	to	*Vc*B-ssDNA	G	DA	12	OP2	3.404
*Vc*B-ssDNA	B	ASN	383	CG	to	*Vc*B-ssDNA	G	DA	12	OP2	3.126
*Vc*B-ssDNA	B	ASN	383	OD1	to	*Vc*B-ssDNA	G	DA	12	OP2	2.483
*Vc*B-ssDNA	B	ASN	383	OD1	to	*Vc*B-ssDNA	G	DA	12	P	3.825
*Vc*B-ssDNA	B	ARG	400	CA	to	*Vc*B-ssDNA	G	DC	11	OP1	3.351
*Vc*B-ssDNA	B	ARG	400	CD	to	*Vc*B-ssDNA	G	DA	12	OP2	3.746
*Vc*B-ssDNA	B	ARG	400	NH1	to	*Vc*B-ssDNA	G	DA	12	OP2	3.77
*Vc*B-ssDNA	B	GLU	401	CA	to	*Vc*B-ssDNA	G	DA	10	C4'	3.997
*Vc*B-ssDNA	B	GLU	401	CA	to	*Vc*B-ssDNA	G	DA	10	C5'	3.812
*Vc*B-ssDNA	B	GLU	401	CA	to	*Vc*B-ssDNA	G	DA	10	O3'	3.636
*Vc*B-ssDNA	B	GLY	403	CA	to	*Vc*B-ssDNA	G	DA	10	OP1	3.887
*Vc*B-ssDNA	C	THR	355	OG1	to	*Vc*B-ssDNA	G	DA	8	C5'	3.886
*Vc*B-ssDNA	C	ASN	383	ND2	to	*Vc*B-ssDNA	G	DC	9	O5'	3.47
*Vc*B-ssDNA	C	ASN	383	CG	to	*Vc*B-ssDNA	G	DC	9	OP1	3.534
*Vc*B-ssDNA	C	ASN	383	ND2	to	*Vc*B-ssDNA	G	DC	9	OP1	3.136
*Vc*B-ssDNA	C	ASN	383	OD1	to	*Vc*B-ssDNA	G	DC	9	OP1	3.236
*Vc*B-ssDNA	C	ASN	383	ND2	to	*Vc*B-ssDNA	G	DC	9	OP2	2.885
*Vc*B-ssDNA	C	ASN	383	ND2	to	*Vc*B-ssDNA	G	DC	9	P	3.222
*Vc*B-ssDNA	C	ARG	384	NH2	to	*Vc*B-ssDNA	G	DA	10	O3'	3.553
*Vc*B-ssDNA	C	ARG	384	NH2	to	*Vc*B-ssDNA	G	DA	10	O5'	3.969
*Vc*B-ssDNA	C	ARG	384	CB	to	*Vc*B-ssDNA	G	DA	10	OP2	3.621
*Vc*B-ssDNA	C	ARG	384	NH2	to	*Vc*B-ssDNA	G	DC	11	OP1	3.334
*Vc*B-ssDNA	C	ARG	384	NH2	to	*Vc*B-ssDNA	G	DC	11	OP2	3.229
*Vc*B-ssDNA	C	ARG	384	NH2	to	*Vc*B-ssDNA	G	DC	11	P	3.476
*Vc*B-ssDNA	C	ARG	400	NH2	to	*Vc*B-ssDNA	G	DC	9	O3'	3.991
*Vc*B-ssDNA	C	ARG	400	CA	to	*Vc*B-ssDNA	G	DC	9	OP1	3.163
*Vc*B-ssDNA	C	ARG	400	CB	to	*Vc*B-ssDNA	G	DC	9	OP1	3.945
*Vc*B-ssDNA	C	GLU	401	CA	to	*Vc*B-ssDNA	G	DA	8	O3'	3.771

*Vc*B-ssDNA	C	GLU	401	CA	to	*Vc*B-ssDNA	G	DC	9	OP1	3.548
*Vc*B-ssDNA	C	GLY	403	CA	to	*Vc*B-ssDNA	G	DA	8	OP1	3.765
*Vc*B-ssDNA	D	ASN	353	CG	to	*Vc*B-ssDNA	G	DG	5	N2	3.974
*Vc*B-ssDNA	D	ASN	353	OD1	to	*Vc*B-ssDNA	G	DG	5	N2	3.119
*Vc*B-ssDNA	D	ASN	383	ND2	to	*Vc*B-ssDNA	G	DT	7	O5'	3.535
*Vc*B-ssDNA	D	ASN	383	CG	to	*Vc*B-ssDNA	G	DT	7	OP1	3.881
*Vc*B-ssDNA	D	ASN	383	ND2	to	*Vc*B-ssDNA	G	DT	7	OP1	3.317
*Vc*B-ssDNA	D	ASN	383	ND2	to	*Vc*B-ssDNA	G	DT	7	OP2	2.826
*Vc*B-ssDNA	D	ASN	383	OD1	to	*Vc*B-ssDNA	G	DA	8	OP2	3.144
*Vc*B-ssDNA	D	ASN	383	ND2	to	*Vc*B-ssDNA	G	DT	7	P	3.287
*Vc*B-ssDNA	D	ARG	384	NH1	to	*Vc*B-ssDNA	G	DC	9	OP1	3.975
*Vc*B-ssDNA	D	ARG	384	CB	to	*Vc*B-ssDNA	G	DA	8	OP2	3.817
*Vc*B-ssDNA	D	ARG	384	NH1	to	*Vc*B-ssDNA	G	DC	9	OP2	3.673
*Vc*B-ssDNA	D	ARG	400	CA	to	*Vc*B-ssDNA	G	DT	7	OP1	3.31
*Vc*B-ssDNA	D	ARG	400	NH1	to	*Vc*B-ssDNA	G	DA	8	OP1	3.523
*Vc*B-ssDNA	D	ARG	400	NH1	to	*Vc*B-ssDNA	G	DA	8	OP2	3.988
*Vc*B-ssDNA	D	GLU	401	CA	to	*Vc*B-ssDNA	G	DA	6	C5'	3.914
*Vc*B-ssDNA	D	GLU	401	CA	to	*Vc*B-ssDNA	G	DA	6	O3'	3.561
*Vc*B-ssDNA	D	GLU	401	CG	to	*Vc*B-ssDNA	G	DA	6	O3'	3.774
*Vc*B-ssDNA	D	GLU	401	CA	to	*Vc*B-ssDNA	G	DT	7	OP1	3.923
*Vc*B-ssDNA	D	GLY	403	CA	to	*Vc*B-ssDNA	G	DA	6	OP1	3.815
*Vc*B-ssDNA	E	THR	355	OG1	to	*Vc*B-ssDNA	G	DA	4	C5'	3.779
*Vc*B-ssDNA	E	THR	355	OG1	to	*Vc*B-ssDNA	G	DC	3	O2	3.494
*Vc*B-ssDNA	E	THR	355	OG1	to	*Vc*B-ssDNA	G	DA	4	O4'	3.947
*Vc*B-ssDNA	E	ASN	383	OD1	to	*Vc*B-ssDNA	G	DG	5	C3'	3.914
*Vc*B-ssDNA	E	ASN	383	CG	to	*Vc*B-ssDNA	G	DG	5	O5'	3.967
*Vc*B-ssDNA	E	ASN	383	ND2	to	*Vc*B-ssDNA	G	DG	5	O5'	3.376
*Vc*B-ssDNA	E	ASN	383	CG	to	*Vc*B-ssDNA	G	DG	5	OP1	3.957
*Vc*B-ssDNA	E	ASN	383	ND2	to	*Vc*B-ssDNA	G	DG	5	OP1	3.414
*Vc*B-ssDNA	E	ASN	383	CG	to	*Vc*B-ssDNA	G	DG	5	OP2	3.968
*Vc*B-ssDNA	E	ASN	383	ND2	to	*Vc*B-ssDNA	G	DG	5	OP2	2.769
*Vc*B-ssDNA	E	ASN	383	OD1	to	*Vc*B-ssDNA	G	DA	6	OP2	3.377
*Vc*B-ssDNA	E	ASN	383	ND2	to	*Vc*B-ssDNA	G	DG	5	P	3.268
*Vc*B-ssDNA	E	ARG	384	CB	to	*Vc*B-ssDNA	G	DA	6	OP2	3.604
*Vc*B-ssDNA	E	ARG	384	NH2	to	*Vc*B-ssDNA	G	DT	7	OP2	3.483
*Vc*B-ssDNA	E	ARG	400	CA	to	*Vc*B-ssDNA	G	DG	5	OP1	3.17
*Vc*B-ssDNA	E	ARG	400	CB	to	*Vc*B-ssDNA	G	DG	5	OP1	3.856
*Vc*B-ssDNA	E	GLU	401	CA	to	*Vc*B-ssDNA	G	DA	4	C4'	3.884
*Vc*B-ssDNA	E	GLU	401	CA	to	*Vc*B-ssDNA	G	DA	4	C5'	3.87
*Vc*B-ssDNA	E	GLU	401	CA	to	*Vc*B-ssDNA	G	DA	4	O3'	3.897
*Vc*B-ssDNA	E	GLY	403	CA	to	*Vc*B-ssDNA	G	DA	4	OP1	3.625
*Vc*B-ssDNA	F	THR	355	OG1	to	*Vc*B-ssDNA	G	DC	2	C5'	3.719

*Vc*B-ssDNA	F	THR	355	OG1	to	*Vc*B-ssDNA	G	DT	1	O4'	3.647
*Vc*B-ssDNA	F	ASN	383	CG	to	*Vc*B-ssDNA	G	DC	3	O5'	3.901
*Vc*B-ssDNA	F	ASN	383	ND2	to	*Vc*B-ssDNA	G	DC	3	O5'	3.271
*Vc*B-ssDNA	F	ASN	383	CG	to	*Vc*B-ssDNA	G	DC	3	OP1	3.928
*Vc*B-ssDNA	F	ASN	383	ND2	to	*Vc*B-ssDNA	G	DC	3	OP1	3.269
*Vc*B-ssDNA	F	ASN	383	ND2	to	*Vc*B-ssDNA	G	DC	3	OP2	3.048
*Vc*B-ssDNA	F	ASN	383	OD1	to	*Vc*B-ssDNA	G	DA	4	OP2	3.653
*Vc*B-ssDNA	F	ASN	383	ND2	to	*Vc*B-ssDNA	G	DC	3	P	3.276
*Vc*B-ssDNA	F	ARG	384	NH2	to	*Vc*B-ssDNA	G	DA	4	C3'	3.931
*Vc*B-ssDNA	F	ARG	384	NH2	to	*Vc*B-ssDNA	G	DG	5	OP1	3.545
*Vc*B-ssDNA	F	ARG	384	CB	to	*Vc*B-ssDNA	G	DA	4	OP2	3.528
*Vc*B-ssDNA	F	ARG	384	NH2	to	*Vc*B-ssDNA	G	DG	5	OP2	3.591
*Vc*B-ssDNA	F	ARG	384	NH2	to	*Vc*B-ssDNA	G	DG	5	P	3.861
*Vc*B-ssDNA	F	ARG	400	CA	to	*Vc*B-ssDNA	G	DC	3	OP1	3.216
*Vc*B-ssDNA	F	ARG	400	CB	to	*Vc*B-ssDNA	G	DC	3	OP1	3.778
*Vc*B-ssDNA	F	GLU	401	CA	to	*Vc*B-ssDNA	G	DC	2	C4'	3.918
*Vc*B-ssDNA	F	GLU	401	CG	to	*Vc*B-ssDNA	G	DC	2	C4'	3.794
*Vc*B-ssDNA	F	GLU	401	CA	to	*Vc*B-ssDNA	G	DC	2	C5'	3.855
*Vc*B-ssDNA	F	GLU	401	OE2	to	*Vc*B-ssDNA	G	DC	3	C5'	3.76
*Vc*B-ssDNA	F	GLU	401	CG	to	*Vc*B-ssDNA	G	DC	2	O3'	3.81

1709

1710 **Supplementary Table 5. native mass spectrometry mass measurements for**
1711 **predominant DnaB assemblies from three bacterial species with and without**
1712 **Mg-ATP.**

Sample	Main Complex	+*x* MgADP	Mass/Da			Mass Error (%)[b]
			Measured	Expected[a]	Δ	
Vc DnaB only	Vc $DnaB_6$	*0*	311,517	311,502	15	0.005
Vc DnaB + Mg-ATP	Vc $DnaB_6$	*0*	311,612	311,502	110	0.04
		1	312,039	311,953	86	0.03
		2	312,476	312,405	71	0.02
		3	312,914	312,856	58	0.02
		4	313,354	313,307	47	0.01
		5	313,786	313,759	27	0.01
		6	314,274	314,210	64	0.02
Ec DnaB only	Ec $DnaB_6$	*0*	313,714	313,553	161	0.05
Ec DnaB + Mg-ATP	Ec $DnaB_6$	*0*	313,738	313,553	185	0.06
		1	314,183	314,004	179	0.06
		2	314,622	314,456	166	0.05
		3	315,070	314,907	163	0.05
		4	315,526	315,358	168	0.05
		5	316,055	315,810	245	0.08
		6	316,508	316,261	247	0.08
BsDnaC only[c]	Bs$DnaC_1$	*0*	51,398	51,399	-1	(0.002)
BsDnaC + Mg-ATP[c]	Bs$DnaC_1$	*0*	51,396	51,399	-3	(0.006)

1713

a. From the protein sequence of Vc DnaB with the N-terminal Met removed (51,917.7 Da), Ec DnaB with the N-terminal Met removed (52,258.8 Da), and *Bs*DnaC (51,399.1 Da).

b. Calculated from the % difference between the measured and expected masses relative to the expected mass. The mass errors are larger for the +Mg-ATP samples due to magnesium adduction (mass of Mg^{2+} = 24 Da)."

c. Additional satellite peaks were observed for the DnaC samples, indicating adduction. The masses of adducted peaks are not shown here.

1723